

UNIVERSITY OF CALIFORNIA, SAN DIEGO

Simulations of molecules and processes in the synapse

A dissertation submitted in partial satisfaction
of the requirements for the degree
Doctor of Philosophy in Chemistry

by

Kaihsu Tai

Committee in charge:

Professor James Andrew McCammon, Chair
Professor Elizabeth A. Komives
Professor John C. Wheeler
Professor Michael Jay Holst
Professor Palmer W. Taylor

2002

Copyright © 2002

Kaihsu Tai

All rights reserved.

The dissertation of Kaihsu Tai is approved, and it is acceptable
in quality and form for publication on microfilm:

_____Chair

University of California, San Diego

2002

Hō· Ma-ma, A-pah, kap A-má

עשות ספרים הרבה אין קץ ולהג הרבה יגעת בשר
קהלת

TABLE OF CONTENTS

Signatures of approval	iii
Dedication	iv
Epigraph	v
Table of contents	vi
List of figures and tables	viii
Acknowledgments	xi
Vita, publications, and field of study	xii
Abstract	xiii
I Introduction	1
A. The synapse	1
B. Molecular dynamics	4
C. Finite element method	9
D. Acknowledgments	12
II Analysis of a 10 ns molecular dynamics simulation of mouse acetylcholin- esterase	14
A. Abstract	14
B. Introduction	15
C. Methods	15
D. Results	20
E. Discussion	28
F. Conclusions	37
G. Acknowledgments	38
III Mechanism of acetylcholinesterase inhibition by fasciculin: 5 ns molecular dynamics simulation	39
A. Abstract	39
B. Introduction	40
C. Methods	41
D. Results	48
E. Discussion	62
F. Conclusions	68
G. Acknowledgments	69

IV	Finite element simulations of acetylcholine diffusion in neuromuscular junctions	70
	A. Abstract	70
	B. Introduction	71
	C. The neuromuscular junction	71
	D. Mathematical setting	73
	E. Neuromuscular junction models	76
	F. Discussion and conclusions	88
	G. Acknowledgments	88
	Bibliography	90
	Colophon	96

LIST OF FIGURES AND TABLES

Figures

I.1	Schematic of the neuromuscular synapse	2
I.2	Electron micrograph of synaptic junction from mouse gastrocnemius muscle	4
II.1	The solute potential energy for the 10.8 ns trajectory	21
II.2	The solute potential energy versus the gorge proper radius ρ	21
II.3	Time dependence of the root mean square deviations (rmsd) for the 10 ns mAChE MD trajectory	22
II.4	The B factor for each residue from the mAChE part in the 1MAH crystal structure	23
II.5	Stereographs of two conformations in the back door region	24
II.6	Selected dihedral angles through the 10 ns that are important to the opening of the back door	25
II.7	The 10 ns time series for the gorge proper radius, $\rho(t)$	25
II.8	The correlation vector for each residue displayed on the initial structure	26
II.9	The correlation vector within each secondary structure element displayed on the initial structure	27
II.10	The average velocity covariance vector for each residue displayed on the initial structure	29
II.11	The gorge proper radius ρ versus the distance between Phe 338 $C_{\epsilon 2}$ and Tyr 124 O_H	30
II.12	Contribution of linear and cross terms to the square distance	31
II.13	The solute potential energy projected onto a histogram of the first two principal components	37
III.1	Overview of the Fas2-mAChE complex structure (1KU6)	43

III.2	Stereograph of the secondary-structure representation the Fas2-mAChE crystal structure (1KU6)	44
III.3	Time series for the openings through the 5 ns Fas2-mAChE MD simulation	47
III.4	Root mean square deviation (rmsd) through the 5 ns Fas2-mAChE MD trajectory.	50
III.5	<i>B</i> factor for each residue	52
III.6	Ratio of <i>B</i> factors for each residue in mAChE	53
III.7	Ratio of <i>B</i> factor for each residue in mAChE	54
III.8	Structures representing the extremal projections on the principal components with the largest eigenvalue	55
III.9	Comparing the average structures from the 10 ns apo-mAChE and from the 5 ns Fas2-mAChE trajectories: visual comparison	56
III.10	Comparing the average structures from the 10 ns apo-mAChE and from the 5 ns Fas2-mAChE trajectories: geometric measurements	57
III.11	Catalytic triad of mAChE	58
III.12	Distribution of the gorge proper radius	59
III.13	Porcupine plots	61
III.14	Interface contact pairs	63
IV.1	Three views of the finite element mesh for the rectilinear model of the neuromuscular junction	78
IV.2	Total number of ACh molecules in the rectilinear NMJ model decreases over time	80
IV.3	The postsynaptic detection level $L(t)$ in the rectilinear NMJ model	81
IV.4	$L(t)$ for NMJ models of fast-twitch and slow-twitch muscles	82
IV.5	$\Lambda(t)$ for NMJ models of fast-twitch and slow-twitch muscles	83
IV.6	Normal versus dystrophic fast-twitch muscle	83

IV.7	Comparing $L(t)$ for different AChE densities	84
IV.8	Three views of the realistic mesh	86
IV.9	Surface area distribution of the AChE holes in the realistic mesh . . .	87
IV.10	The postsynaptic detection level $L(t)$ over $150\ \mu s$ in the realistic NMJ model	87

Table

IV.1	Geometric dimensions for the recilinear models of different muscle types	81
------	--	----

ACKNOWLEDGMENTS

First I should say “Chin to-siā!” to A-pah, Ma-ma, kap A-má for bearing with – even encouraging – my numerous “He sī sia^{nh}?” (“What’s that?”) since my earliest years, as this dissertation is a culmination thereof.

I thank Andy McCammon, Mike Holst, and Palmer Taylor for mentoring me, with encouragement and admonishment, each timely administered; I especially thank Andy for keeping me in his research group for 4 years! I thank La Jolla Interfaces in Science fellowship and the Burroughs Wellcome Fund for giving me money to do fun science.

I thank the members of the McCammon group – especially, Prof. Nathan Andrew Baker, Dr Stephen David Bond, Mr Ulf Erik Börjesson, Dr Richard Humfry Henchman, Dr Jeremy Kua, Dr Hugh Robert MacMillan, Dr Marios Philippopoulos, Prof. David Samuel Sept, and Dr Shěn Tóngyè – for being great friends, colleagues, and some even role models during my graduate school years. I thank Dr Yves Bourne, Dr Pascale Marchot, and Dr Tjerk P. Straatsma for their trust in collaborating with me. I thank Prof. William A. Goddard III and Dr Kenneth A. Brameld for introducing me to molecular dynamics and for allowing me to work with them during my days at Caltech. I thank my family, my friends, and the many good teachers and ministers in my life.

Parts of the material in I.A.1 are excerpted from an article that appeared in the *Accounts of Chemical Research* [1], of which I am a coauthor.

Chapter II contains the same material as an article that appeared in the *Biophysical Journal* [2]. Chapter III contains the same material as an article that appeared in the *Journal of American Chemical Society* [3]. Chapter IV contains the same material as a manuscript submitted to the *Biophysical Journal*. I am the primary author of these articles.

VITA

February 6, 1977	Born, Taipei (Tâi-pak), Taiwan
1998	Bachelor of Science with Honor (Chemistry; Dabney House), California Institute of Technology
2000	Master of Science, Chemistry, University of California, San Diego
2000 to 2002	Fellow, La Jolla Interfaces in Science, Burroughs Wellcome Fund
2002	Doctor of Philosophy, University of California, San Diego

PUBLICATIONS

Shen, T. Y.; **Tai, K.**; McCammon, J. A. Statistical analysis of the fractal gating motions of the enzyme acetylcholinesterase. *Phys. Rev. E* **2001**, *63*, 041902.

Tai, K.; Shen, T.; Börjesson, U.; Philippopoulos, M.; McCammon, J. A. Analysis of a 10-ns molecular dynamics simulation of mouse acetylcholinesterase. *Biophys. J.* **2001**, *81*, 715–724.

Shen, T.; **Tai, K.**; Henchman, R.; McCammon, J. A. Molecular dynamics of acetylcholinesterase. *Acc. Chem. Res.* **2002**, *35*, 332–340.

Henchman, R. H.; **Tai, K.**; Shen, T.; McCammon, J. A. Properties of water molecules in the active site gorge of acetylcholinesterase from computer simulation. *Biophys. J.* **2002**, *82*, 2671–2682.

Tai, K.; Shen, T.; Henchman, R. H.; Bourne, Y.; Marchot, P.; McCammon, J. A. Mechanism of acetylcholinesterase inhibition by fasciculin: a 5-ns molecular dynamics simulation. *J. Am. Chem. Soc.* **2002**, *124*, 6153–6161.

Baker, N.; **Tai, K.**; Henchman, R.; Sept, D.; Elcock, A.; Holst, M.; McCammon, J. A. Mathematics and molecular neurobiology. In *Advances in Computational Methods for Macromolecular Modeling: Theory and Application in Biomolecular Systems*; Schlick, T.; Gan, H. H., Eds.; Springer-Verlag: Berlin, 2002.

FIELD OF STUDY

Major Field: Biochemistry
Studies in computer simulation of biological systems.
Professor J. Andrew McCammon

ABSTRACT OF THE DISSERTATION

Simulations of molecules and processes in the synapse

by

Kaihsu Tai

Doctor of Philosophy in Chemistry

University of California, San Diego, 2002

Professor J. Andrew McCammon, Chair

Two nanosecond-timescale molecular dynamics simulations of acetylcholinesterase (EC 3.1.1.7) were analyzed: one unliganded, the other complexed with the snake-venom toxin fasciculin 2. These simulation trajectories revealed complex fluctuation of the active site gorge. In both simulations, we observe a two-peaked probability distribution of the gorge width. Comparing the gorge width with the principal components of motion showed that collective motions of many scales contribute to the opening behavior of the gorge. Covariance and correlation results, as displayed in the novel “porcupine plots”, identified the motions of the protein backbone as the gorge opens.

Fasciculin 2 binds to the gorge entrance of acetylcholinesterase with excellent complementarity and many polar and hydrophobic interactions; it appears to sterically block access of ligands to the gorge. When fasciculin is present, the gorge width distribution is altered such that the gorge is more likely to be narrow. Moreover, there are large increases in the opening of alternative passages, namely the side door and the back door. Finally, the catalytic triad arrangement in the acetylcholinesterase active site is disrupted with fasciculin bound. These data support that, in addition to the steric obstruction seen in the crystal structure, fasciculin may inhibit acetylcholinesterase by combined allosteric and dynamical means.

On a larger scale, the general infrastructure for solving the time-dependent diffusion equation using the finite element method has been implemented. Simulations of

synaptic transmission were performed using simplified rectilinear models of the neuromuscular junction to demonstrate the effects of synaptic geometries and reactivity parameters. Observations from models representing synapses in fast- and slow-twitch muscles follow the trends of experimental data. One of our models explains the effects of geometry in muscular dystrophy; another demonstrates the capability of our infrastructure to simulate complicated realistic models based on electron microscopy data.

I

Introduction

I.A The synapse

A synapse is a junction through which a nerve cell, or a neuron, communicates with another cell. There are two types of synapses, categorized by the manner of transmission: electrical synapses and chemical synapses [4–6]. This dissertation presents simulations on some molecules and processes in the cholinergic synapses, the chemical synapses which employs acetylcholine (ACh) as the neurotransmitter molecule. The neuromuscular junctions, synapses that transmits signal from a neuron to a muscle cell, are predominately cholinergic; cholinergic synapses are also present in the central nervous system.

I.A.1 The chemistry of synaptic transmission

Signaling from nerve to muscle is mediated by ACh in neuromuscular junctions. The mechanism of this process is as follows (Figure I.1). ACh is synthesized from choline and acetyl-CoA and packaged into vesicles in the presynaptic terminal. An action potential arriving at the terminal of the presynaptic neuron triggers the opening of voltage-

I.A.1 is reproduced in part with permission from Shen, T.; Tai, K.; Henchman, R.; McCammon, J. A. *Acc. Chem. Res.* **2002**, *35*, 332–340. Copyright © 2002 American Chemical Society.

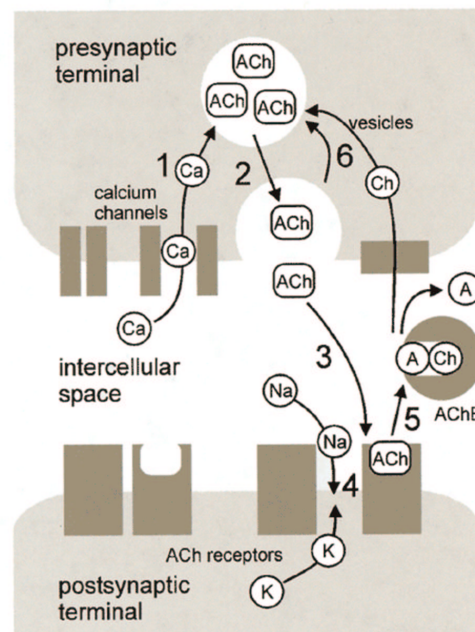


Figure I.1: Schematic of the neuromuscular synapse. (1) Depolarizing of the cell opens Ca^{2+} channels and Ca^{2+} enters. (2) Ca^{2+} stimulates vesicles to release acetylcholine (ACh) into the synapse. (3) ACh diffuses and binds to the ACh receptors, opening their ion channels. (4) Na^{+} and K^{+} diffuse through the channel, depolarizing the postsynaptic terminal. (5) ACh diffuses to acetylcholinesterase (AChE) and is hydrolyzed to choline (Ch) and acetate (A). (6) Ch is taken up for resynthesis of ACh and packaged into vesicles.

gated Ca^{2+} channels. Ca^{2+} entering the cytosol stimulates the vesicles to release their ACh by exocytosis into the synaptic cleft. ACh diffuses across the cleft and binds to and activates the postsynaptic receptors, allowing Na^{+} and K^{+} to diffuse across the membrane and depolarize the muscle cell. The enzyme acetylcholine (AChE) quickly degrades ACh to acetate and choline, deactivating the receptor and tapering off the transmitted nerve impulse. Choline is taken up again by the presynaptic terminal for resynthesis of ACh.

Several diseases are related to dysfunctions of the synapse. For example, one symp-

tom of Alzheimer's disease is the reduction of ACh concentration; in patients with myasthenia gravis (serious muscle weakness) there are fewer receptors than normal. In these cases, moderate inhibition of AChE is effective in the treatment of the disease to prolong the effect of ACh on the receptor. Some AChE inhibitors for treatment of Alzheimer's disease are tacrine, rivastigmine, and galantamine [7]. Inhibitors for treatment of myasthenia gravis include pyridostigmine and neostigmine [8]. However, overwhelming inhibition of AChE, particularly by covalent bonding to the active site serine, is invariably lethal. Hence, AChE is a prime target for naturally occurring toxins such as the snake venom fasciculin 2 (Fas2), pesticides such as parathion and malathion, and chemical warfare agents such as sarin, tabun, and VX [9].

The work in Chapters II and III explores the dynamics of the AChE molecule and mechanism of AChE inhibition by Fas2 using simulation.

I.A.2 The geometries of the neuromuscular synapse

The most striking feature of the neuromuscular junction, as observed by electron microscopy [10, 11] and more recently by electron tomography, is the postsynaptic folds, consisting of long valleys and crests directly opposing those presynaptic "active zones" (Figure I.2). In contrast, the presynaptic membrane is smoother in geometry; the active zones therein are arranged in rows, from which the vesicles of neurotransmitters are released into the synaptic cleft, the space between the pre- and postsynaptic membranes.

Not all synapses share the same geometry: synapses of the slow-twitch and the fast-twitch muscles in the same organism differ in their geometric structures. Further, neuromuscular junctions in dystrophic animals are not geometrically similar to those in normal ones. The work in Chapter IV builds a finite element model of the synapse, with the geometry as a part of the parameter set, and subsequently seeks to explain the effects of differing geometries on synaptic transmission.

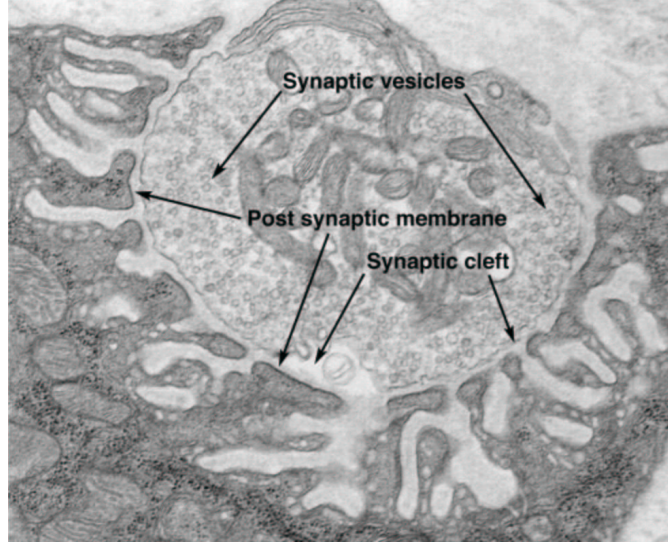


Figure I.2: Electron micrograph of synaptic junction from mouse gastrocnemius muscle.

I.B Molecular dynamics

Molecular dynamics (MD) solves Newton's equation of motion on an atomistic model of a molecule to obtain the trajectory of its motion. The positions $\mathbf{r}(t)$ of the atoms in the molecule are recorded at selected time points t through the simulation; a force field is used to describe the interaction between the atoms.

I.B.1 Force field

The following MD simulations use the AMBER (Assisted Model Building with Energy Refinement) force field [12] as the model for biomolecules, and the extended simple point charge (SPC/E) model [13] for water molecules. In the AMBER force field, for a conformation of the molecule \mathbf{r} , the potential energy is modeled as

$$\begin{aligned}
 E(\mathbf{r}) = & \sum_{\text{bonds}} K_r (r - r_{\text{eq}})^2 + \sum_{\text{angles}} K_\theta (\theta - \theta_{\text{eq}})^2 \\
 & + \sum_{\text{dihedrals}} \frac{V_n}{2} [1 + \cos(n\phi - \gamma)] + \sum_{i < j} \left[\frac{A_{ij}}{R_{ij}^{12}} - \frac{B_{ij}}{R_{ij}^6} + \frac{q_i q_j}{\epsilon R_{ij}} \right], \quad (\text{I.1})
 \end{aligned}$$

which takes into account the contributions from bond lengths and angles, dihedral angles, van der Waals interactions, and electrostatic interactions. The analytical form of the force on the molecule can then be derived using the fact that it is the negative gradient of the potential energy,

$$\mathbf{F} = -\frac{\partial E(\mathbf{r})}{\partial \mathbf{r}}. \quad (\text{I.2})$$

The acceleration \mathbf{a} is obtained using Newton's equation of motion

$$\mathbf{F} = m\mathbf{a}. \quad (\text{I.3})$$

I.B.2 Time-stepping

The position and acceleration at a certain time t are used in the Verlet leap-frog method [14–16] to calculate the atom positions after one time-step δt :

$$\mathbf{r}(t + \delta t) = \mathbf{r}(t) + \delta t \mathbf{v}(t + \frac{1}{2}\delta t) \quad (\text{I.4})$$

where the velocity at time $t + \frac{1}{2}\delta t$ is

$$\mathbf{v}(t + \frac{1}{2}\delta t) = \mathbf{v}(t - \frac{1}{2}\delta t) + \delta t \mathbf{a}(t) \quad (\text{I.5})$$

which requires the velocity at time $t - \frac{1}{2}\delta t$. For calculating the kinetic energy, temperature and other properties which requires the velocity at time t , the expression for current velocity is used:

$$\mathbf{v}(t) = \frac{1}{2} (\mathbf{v}(t + \frac{1}{2}\delta t) + \mathbf{v}(t - \frac{1}{2}\delta t)). \quad (\text{I.6})$$

I.B.3 Constrained dynamics

It has been shown that constraining the bond lengths between hydrogens and the heavier atoms, using the SHAKE algorithm [17, 18] described below, can speed up the time-stepping calculation while maintaining the dynamical properties observed in the trajectory on time scales larger than 0.05 ps.

Used after each unconstrained time-stepping is performed, the SHAKE algorithm iterates through a list of constraints starting from the first, and adjusts the positions of the atoms as each constraint is being applied. Thus, as the k th constraint, which fixes the bond length between atoms i and j , is about to be applied, any previous k' th constraint with $k' < k$ has already been applied; we call this the previous atom position. If there is no previous constraint, the previous atom position is the position resulting from the unconstrained time-stepping.

Let m_ι be the mass of atom $\iota = i, j$; d be the i - j target bond length for this k th constraint; \mathbf{r} be the distance between atoms i and j before the last unconstrained time step, which satisfies the constraint; \mathbf{r}' be the distance after all k' th constraints with $k' < k$ have been applied. The SHAKE algorithm make the following adjustment to the previous atom position for atom ι :

$$\delta \mathbf{r}_\iota = \frac{g \mathbf{r}}{m}, \quad \iota = i, j \quad (\text{I.7})$$

where

$$g = \frac{d^2 - \mathbf{r}' \cdot \mathbf{r}'}{2 \left(\frac{1}{m_i} + \frac{1}{m_j} \right) \mathbf{r} \cdot \mathbf{r}'} \quad (\text{I.8})$$

It is likely that by making this adjustment, some of the previous constraints will become broken. The SHAKE algorithm is repeated until all constraints are satisfied within a specified tolerance, usually 10^{-4} of the target bond length.

I.B.4 Constant temperature and pressure

To perform MD simulations under the condition of constant temperature and constant pressure, the system is coupled to an external bath. The extent of such coupling is determined by a time constant. The following MD simulations use an external temperature and pressure bath that is weakly coupled to the system.

During each time-step, the velocity of the atoms is proportionally scaled such that the change in temperature over this time-step $\frac{\Delta T}{\delta t}$ satisfies

$$\frac{dT}{dt} \approx \frac{\Delta T}{\delta t} = \frac{1}{\tau_T} (T_0 - T) \quad (\text{I.9})$$

where T is the system temperature, T_0 is the temperature of the bath, and τ_T is the temperature-coupling time constant. Recall that the velocity of the atoms v (each with mass m) and the system temperature are related through the kinetic energy, namely,

$$\sum_{\text{atoms}} \frac{1}{2}mv^2 = \frac{3}{2}Nk_B T \quad (\text{I.10})$$

where N is the total number of atoms, and k_B the Boltzmann constant. It follows that the velocity of each atom should be scaled from v to λv , where

$$\lambda = \left[1 + \frac{\delta t}{\tau_T} \left(\frac{T_0}{T} - 1 \right) \right]^{\frac{1}{2}} \quad (\text{I.11})$$

Similarly, isotropic pressure coupling is achieved by scaling the boundary sizes and the coordinates of the atoms from l to μl , with

$$\mu = \left[1 - \frac{\delta t}{\tau_p} (p_0 - p) \right]^{\frac{1}{3}} \quad (\text{I.12})$$

where p is the system pressure, p_0 the pressure of the external bath, and τ_p the pressure-coupling time constant.

I.B.5 Electrostatics with periodic boundary condition

When periodic boundary conditions are used in a molecular dynamics simulation, van der Waals and other short-range interactions can be easily calculated within the unit box. However, electrostatic interactions are long-range and usually reach beyond the neighboring boxes. To calculate the interaction between an ion and its periodic images, the Ewald sum [15] is used.

For N ions in a cubic unit box of edge length L in a lattice, the electrostatic potential energy among all ions in all copies of the unit box is

$$\mathcal{V}^{zz} = \frac{1}{8\pi\epsilon_0} \sum_{\mathbf{n}}' \left(\sum_{i=1}^N \sum_{j=1}^N z_i z_j \left| \mathbf{r}_{ij} + \mathbf{n} \right|^{-1} \right) \quad (\text{I.13})$$

where z_i and z_j are the charges on the ion, and the sum over \mathbf{n} is the sum over all lattice points $\mathbf{n} = (n_x L, n_y L, n_z L)$, with n_x, n_y, n_z being integers; the prime excludes summing

over the cases with $i = j$ for $\mathbf{n} = 0$. For faster convergence in the calculation of this potential energy, the Ewald summation is used instead:

$$\begin{aligned}
 \mathcal{V}^{zz} = & \underbrace{\frac{1}{8\pi\epsilon_0} \sum_{i=1}^N \sum_{j=1}^N \left(\sum_{|\mathbf{n}|=0}^{\infty}{}' z_i z_j \frac{\text{erfc}(\kappa|\mathbf{r}_{ij} + \mathbf{n}|)}{|\mathbf{r}_{ij} + \mathbf{n}|} \right)}_{\text{I}} \\
 & + \underbrace{\frac{1}{2\epsilon_0 L^3} \sum_{i=1}^N \sum_{j=1}^N \left(\sum_{\mathbf{k} \neq 0} z_i z_j \frac{1}{k^2} \exp\left(\frac{-k^2}{4\kappa^2}\right) \cos(\mathbf{k} \cdot \mathbf{r}_{ij}) \right)}_{\text{II}} \\
 & + \underbrace{\frac{1}{4\pi\epsilon_0} \frac{\kappa}{\sqrt{\pi}} \sum_{i=1}^N z_i^2}_{\text{III}}
 \end{aligned} \tag{I.14}$$

In Equation I.14, term **I** sums, in real space, the original charges with screening charges that are by construction Gaussian; term **II** cancels the contribution from the screening charges; term **III** corrects the self-energy of the screening charges that is included in term **I**. The value κ is an arbitrary parameter chosen to optimize the summation. In implementation, particle-mesh Ewald [19], an algorithm that scales as $N \log N$, is used.

I.B.6 Implementation: parallel supercomputing

The following MD simulations have been carried out using NWChem [20] on two supercomputers, the Cray T3E and the “Blue Horizon”. The Blue Horizon is an IBM Scalable POWERparallel (SP) machine. Each of the supercomputers consists of multiple processors connected by switches for inter-processor communication.

NWChem calculates the MD trajectory using multiple processors in parallel. The calculation work-load is distributed to each of the processors, and the results are then collected by a processor and written out to disk storage. The work-load is distributed using spatial domain decomposition: the molecular system on which MD is to be performed is spatially divided into smaller boxes. Each processor is responsible for a box. The length of an MD time step is the time taken by the processor that last finishes the calculation, plus the time for the inter-processor communication during the distribution

of work-load and collection of results. The speed or efficiency of the MD simulation can be improved by load-balancing schemes.

I.C Finite element method

The finite element method [21] solves partial differential equations, of which the diffusion equation is an instance.

I.C.1 Diffusion equation

The diffusion equation is of the form

$$\nabla \cdot D \nabla c = f \quad \text{in } \Omega \in \mathbf{R}^d \quad (\text{I.15})$$

where c , a function of position, is the concentration of the species of interest; D is the diffusion constant; and \mathbf{R} is the set of all real numbers. Ω is called the domain; d is then the number of dimensions of the domain. A boundary condition on the boundary $\partial\Omega$ needs to be specified. The Dirichlet boundary condition is

$$c = c_D \quad \text{on } \partial\Omega. \quad (\text{I.16})$$

where c_D can be a function of position or time. The Neumann, or reflective, boundary condition is

$$\hat{\mathbf{n}} \cdot \nabla c = 0 \quad \text{on } \partial\Omega. \quad (\text{I.17})$$

where $\hat{\mathbf{n}}$ is the exterior unit normal vector of the boundary. It is admissible to have parts of the boundary be Neumann, and the other part be Dirichlet. In the steady-state diffusion problem, we simply have $f = 0$; in the time-dependent problem, we have $f = \frac{dc}{dt}$, where t is time.

I.C.2 Weak formulation

Consider the one-dimensional model diffusion problem

$$\nabla \cdot D \nabla c(x) = f \quad \text{in } \Omega = [0, 1] \quad (\text{I.18})$$

with the Dirichlet boundary condition

$$c(x) = 0 \quad \text{on} \quad \partial\Omega = \{0, 1\}. \quad (\text{I.19})$$

It is beneficial to transform this into a weak formulation by introducing a test function $v : \Omega \mapsto \mathbf{R}$ with $v = 0$ on $\partial\Omega$. Then, we multiply both sides of (I.18) by v and integrate over Ω .

$$\int_{\Omega} (\nabla \cdot D\nabla c) v \, dx = \int_{\Omega} f v \, dx. \quad (\text{I.20})$$

The divergence theorem says

$$\int_{\Omega} (\nabla \cdot \vec{w}) z \, dx = - \int_{\Omega} \vec{w} \cdot \nabla z \, dx + \oint_{\partial\Omega} \vec{w} z \cdot \hat{\mathbf{n}} \, dS. \quad (\text{I.21})$$

Setting $\vec{w} = D\nabla c$ and $z = v$, we have

$$\int_{\Omega} (\nabla \cdot D\nabla c) v \, dx = - \int_{\Omega} D\nabla c \cdot \nabla v \, dx + \oint_{\partial\Omega} (D\nabla c) v \cdot \hat{\mathbf{n}} \, dS. \quad (\text{I.22})$$

Since we have chosen

$$v = 0 \quad \text{on} \quad \partial\Omega, \quad (\text{I.23})$$

we have

$$\oint_{\partial\Omega} (D\nabla c) v \cdot \hat{\mathbf{n}} \, dS = 0, \quad (\text{I.24})$$

and (I.22) becomes simply

$$\int_{\Omega} (\nabla \cdot D\nabla c) v \, dx = - \int_{\Omega} D\nabla c \cdot \nabla v \, dx. \quad (\text{I.25})$$

Plugging this into (I.20), we have

$$- \int_{\Omega} D\nabla c \cdot \nabla v \, dx = \int_{\Omega} f v \, dx. \quad (\text{I.26})$$

We then define

$$A(c, v) := \int_{\Omega} D\nabla c \cdot \nabla v \, dx \quad (\text{I.27})$$

$$F(v) := \int_{\Omega} f v \, dx \quad (\text{I.28})$$

to get the weak formulation

$$-A(c, v) = F(v). \quad (\text{I.29})$$

It can be proven that any solution that satisfies the model problem (I.18) also satisfies the following weak-form problem: Find $u \in H_0^1(\Omega)$ such that the weak formulation (I.29) is satisfied $\forall v \in H_0^1$, where the definitions of the Hilbert spaces are

$$H^1 := \left\{ c \mid \|c\|_{H^1} < \infty \right\} \quad (\text{I.30})$$

$$H_0^1(\Omega) := \left\{ c \in H^1 \mid c = 0 \text{ at } x = 0, x = 1 \right\} \quad (\text{I.31})$$

and the norms and semi-norm are defined as

$$|c|_{H^1} := \left[\int_0^1 \left(\frac{dc}{dx} \right)^2 dx \right]^{\frac{1}{2}} \quad (\text{I.32})$$

$$\|c\|_{L^2} := \left(\int_0^1 c^2 dx \right)^{\frac{1}{2}} \quad (\text{I.33})$$

$$\|c\|_{H^1} := \|c\|_{L^2} + |c|_{H^1}. \quad (\text{I.34})$$

I.C.3 Galerkin approximation

The Galerkin method finds an approximation of the true solution in a subset \mathbf{V}_h of the Hilbert space ($H_0^1 = H_0^1(\Omega)$ for the model problem). The problem now becomes: Find $c_h \in \mathbf{V}_h \subset H_0^1(\Omega)$ such that

$$-A(c_h, v_h) = F(v_h), \quad \forall v_h \in \mathbf{V}_h. \quad (\text{I.35})$$

\mathbf{V}_h is constructed as a span of a set of bases or “elements”; that is,

$$\mathbf{V}_h = \text{span}\{\phi_1, \phi_2, \dots, \phi_n\} \quad (\text{I.36})$$

These bases ϕ_i are defined using the following procedure: First, the domain $\Omega = [0, 1]$ is tessellated into a uniform mesh, with vertices $x_i = ih$ where $h = 1/N$ and $i = 0, \dots, N$. Then, the elements ϕ_i is thus defined:

$$\phi_i(x) = \begin{cases} \frac{1}{h}(x - x_{i-1}), & x \in [x_{i-1}, x_i] \\ \frac{1}{h}(x_{i+1} - x), & x \in (x_i, x_{i+1}] \\ 0 & \text{otherwise} \end{cases} \quad (\text{I.37})$$

These kinds of elements have three important properties: (a) local support, (b) continuous, and (c) within the interval between two neighboring vertices, the element is simply a linear polynomial.

Setting

$$c_h = \sum_{j=1}^N c_j \phi_j, \quad (I.38)$$

$$v_h = \phi_i, \quad i = 1, \dots, N \quad (I.39)$$

in (I.35), we have a set of equations

$$-A \left(\sum_{j=1}^N c_j \phi_j, \phi_i \right) = F(\phi_i), \quad i = 1, \dots, N \quad (I.40)$$

$$\Rightarrow - \sum_{j=1}^N c_j A(\phi_j, \phi_i) = F(\phi_i), \quad i = 1, \dots, N \quad (I.41)$$

This is equivalent to a matrix equation to solve:

$$-\mathbf{A}\mathbf{c} = \mathbf{F} \quad (I.42)$$

where each of the entries $A_{ij} = A(\phi_j, \phi_i)$ in the matrix \mathbf{A} , each of the entries c_i in the vector \mathbf{c} are to be solved, and each of the entries $F_i = F(\phi_i)$ in the vector \mathbf{F} . Thus, a partial differential equation is transformed into a matrix equation which is tractable using linear algebra and numerical methods. The solution, which is an approximation of the concentration, can be recovered using (I.38).

I.C.4 Generalization and approximation theory

This treatment by the Galerkin method can be generalized to solve partial differential equations in higher dimensions and time-dependent problems. The tessellation can be non-uniform, and elements can be designed in a variety of manners. The quality of the approximation can be evaluated *a posteriori* and even *a priori*.

I.D Acknowledgments

Figure I.2 is courtesy of Prof. Mark H. Ellisman.

Parts of the material in I.A.1 are excerpted from an article that appeared in the *Accounts of Chemical Research* [1], of which I am a coauthor.

II

Analysis of a 10 ns molecular dynamics simulation of mouse acetylcholinesterase

... la dimensione del tempo è andata in frantumi, non possiamo vivere o pensare se non spezzoni di tempo che s'allontanano ognuno lungo una sua traiettoria e subito spariscono. [22]

II.A Abstract

A 10 ns molecular dynamics simulation of mouse acetylcholinesterase was analyzed, with special attention paid to the fluctuation in the width of the gorge, and opening events of the back door. The trajectory was first verified to ensure its stability. We defined the gorge proper radius as the measure for the extent of gorge opening. We developed an expression of an inter-atom distance representative of the gorge proper radius in terms of projections on the principal components. This revealed the fact that collective motions of many scales contribute to the opening behavior of the gorge. Co-

This chapter is reproduced with permission from Tai, K.; Shen, T.; Börjesson, U.; Philippopoulos, M.; McCammon, J. A. *Biophys. J.* **2001**, *81*, 715–724. Copyright © 2001 Biophysical Society.

variance and correlation results identified the motions of the protein backbone as the gorge opens. In the back door region, side chain dihedral angles that define the opening were identified.

II.B Introduction

Acetylcholinesterase (AChE) is the enzyme responsible for the termination of signaling in cholinergic synapses (such as the neuromuscular junction) by degrading the neurotransmitter acetylcholine. AChE has a gorge, 2 nm deep, leading to the catalytic site. Molecular dynamics (MD) simulations [14, 23] have shown breathing motions of this gorge [24–26]. They also showed that an alternative portal providing access to the catalytic site is present in AChE. This back door, as it is called, may facilitate rapid solvent and product removal [24, 27].

In this paper, we collect a 10 ns trajectory of mouse AChE (mAChE) using MD simulation. We define and calculate the time series for the proper radius of the gorge and for the back door opening events, as observed in our 10 ns MD trajectory. We also perform principal component analysis for the trajectory. Then we look for correlations among the results from our analyses with a view to finding the important collective motions in AChE responsible for its opening behaviors.

II.C Methods

II.C.1 Molecular dynamics simulation

The previous 1 ns MD simulation of mouse AChE [27] was extended to afford a trajectory of 10.8 ns. The set-up procedure has been described in the previous paper, and is summarized below. The crystal structure of mouse AChE (mAChE) in complex with fasciculin 2 (Fas2) [28] (Protein Data Bank identification code: 1MAH) was used to model unliganded mAChE. Fas2 was removed from the structure and seven residues in mAChE that are missing in 1MAH (residues 258–264) were repaired by modeling with

Insight II (Accelrys, San Diego, California) to give the initial structure. The protein was solvated in a cubic box (9.6 nm edges) of pre-equilibrated water molecules. In order to neutralize the -10 charge of mAChE, 9 sodium ions were placed in the solvent at about 0.5 nm from the protein surface, and one sodium ion was placed in the active site near Trp 86 and His 447. The simulation system had a total of 8 289 solute atoms and 75 615 solvent atoms.

The simulation was performed in the isothermal-isobaric ensemble. The solvent and solute were separately coupled to temperature reservoirs of 298.15 K with coupling times of 0.1 ps. Pressure was restrained to 1 atmosphere with a coupling time of 0.4 ps. All minimization and MD simulation steps were performed using NWChem Version 3.0 [20] with the AMBER 94 force field [12]. Long-range electrostatic interactions were calculated using particle-mesh Ewald summation [19]. Bond lengths between hydrogens and heavy atoms were constrained using SHAKE [17]. The simulation was performed on 32 processors of a Cray T3E parallel supercomputer at the San Diego Supercomputer Center over a period of 3 years, consuming a total of about 200 processor-months of supercomputer time. Frames were collected at 1 ps intervals for the simulation length of 10.8 ns, giving 1.08×10^4 frames. The first 700 frames of this trajectory were considered the equilibration phase and not used in the main analysis for reasons described in the Results section; only the subsequent 10 000 frames (10 ns) were used in the main analysis. Thus, the last 300 ps of the previous trajectory [27] is the first 300 ps of the present 10 ns trajectory admitted for analysis.

II.C.2 Proper radius of the gorge

In order to characterize the degree of the gorge opening with a single variable, we defined the gorge proper radius ρ for the conformation of each snapshot as the maximum radius of a spherical ligand that can go through the gorge from outside the protein to reach the bottom. Equivalently, it is the maximum probe radius that still generates a solvent accessible surface with a continuous topology.

In our algorithm, we first generate the Shrake and Rupley surface with a testing

probe sphere of given radius; then we try to determine whether the surface generated by the atom O_γ in residue Ser 203 (one of the residues in the active site; the bottom of the gorge) is topologically continuous with the surface of bottleneck region (represented by the atoms Leu 76 $C_{\delta 1}$, Trp 286 C_β , and Tyr 72 O_H) for that probe radius. Using a binary search algorithm to decide what will be the next probe radius, we can determine ρ with desired precision. We started with a test value of 160 pm, and assumed ρ to be bounded by 80 pm and 240 pm. With 6 iterations in the binary search algorithm, we achieved a final discretization of 5 pm. We calculated ρ for each snapshot, and the results were collected as a time series $\rho(t)$.

II.C.3 Back door opening events

In addition to the gorge, MD results from this and previous [27] simulations of mACHe also showed an alternative opening occasionally large enough for at least water molecules to pass. This opening, named the back door [24], is conjectured to assist in releasing solvent or reaction products. The back door is formed by the residues Trp 86, Gly 448, Tyr 449, and Ile 451. Instead of using multiple probe radii to calculate the proper radius, as in the case of the gorge, we used a single probe radius of 140 pm to test whether it is open or closed. We always blocked the gorge entrance while probing for back door opening events. (Similarly, we blocked the back door region in the gorge calculation described above.) Each frame that the algorithm reported to have a back door opening was verified visually using *Insight II*. The result is expressed as a time series

$$\Upsilon(t) := \begin{cases} 0 & \text{if closed;} \\ 1 & \text{if open.} \end{cases} \quad (\text{II.1})$$

II.C.4 Principal components

Principal component analysis. Considering only the α -carbon atoms, the N -residue trajectory can be considered as a vector function of time t , namely

$$\mathbf{r}(t) = \left[r_{1x}(t), r_{1y}(t), \dots, r_{Nz}(t) \right]^T \quad (\text{II.2})$$

of size $f = 3N$, containing the Cartesian coordinates at time t for residue 1 in the x -direction, residue 1 in the y -direction, \dots , up to residue N in the z -direction.

The ij -entry C_{ij} of the covariance matrix C is the covariance of the positions for two degrees of freedom i and j , namely, $C_{ij} = \langle (r_i(t) - \langle r_i \rangle_t)(r_j(t) - \langle r_j \rangle_t) \rangle_t$ where $\langle \cdot \rangle_t$ is the time average over the whole trajectory. Principal component analysis (PCA) [25, 29–31] diagonalizes C by solving $\Lambda = T^T C T$, so as to obtain the diagonal matrix Λ with the diagonal entries being the eigenvalues ranked by magnitude. The c th column of the transformation matrix T is the c th eigenvector \mathbf{v}_c , that is, $T = [\mathbf{v}_1, \mathbf{v}_2, \dots, \mathbf{v}_f]$.

In our analysis, the algorithm for PCA of the Cartesian coordinates of the α -carbon atoms was implemented in the Java programming language, with the JAMA matrix package (The MathWorks, Natick, Massachusetts, and National Institute of Standards and Technology, Gaithersburg, Maryland).

The first 5 residues in the MD simulation (residues 4 to 8) and the last 5 (residues 539 to 543) were removed before the PCA in order to avoid terminal motions excessively dominating the analysis. Therefore, each frame contained the Cartesian coordinates for $N = 530$ α -carbon atoms (Leu 9 to Lys 538), or $f = 3N = 1590$ degrees of freedom. Each frame in the 10 ns trajectory is superimposed to the first frame using quaternion fitting before being admitted into the PCA. This removes the motions in the rotational and translational degrees of freedom.

Using the transformation matrix T , we can convert between the projections along the principal components and the Cartesian coordinates using $\Delta \mathbf{r}(t) := \mathbf{r}(t) - \langle \mathbf{r} \rangle_t = T \mathbf{p}(t)$, where $\mathbf{p}(t) = [p_1(t), p_2(t), \dots, p_f(t)]^T$ is a vector of size f ; the c th entry thereof is the projection along the principal component c .

“Backprojecting”: expressing a C_α – C_α distance in terms of projections along principal components. Knowing the rules for matrix multiplication, we can solve for each of the entries in $\Delta \mathbf{r}$. For example, the deviation from average for residue 124 in the x -direction is $\Delta r_{124x} = v_{1,124x}p_1 + v_{2,124x}p_2 + \dots + v_{f,124x}p_f$ where $v_{i,124x}$ is the (scalar) entry in the i th eigenvector that corresponds to residue 124 in the x -direction, etc. (For

simplicity in notation, we omit explicitly writing out that the rs and ps are indeed functions of time.)

The squared distance between residues 124 and 338 (see the Results section for the reason of this choice of residues) can then be written as

$$\begin{aligned} \left[d_{124,338}(t) \right]^2 &= (r_{124x} - r_{338x})^2 + (r_{124y} - r_{338y})^2 + (r_{124z} - r_{338z})^2 \quad (\text{II.3}) \\ &= \left(\langle r_{124x} \rangle_t - \langle r_{338x} \rangle_t + \Delta r_{124x} - \Delta r_{338x} \right)^2 \\ &\quad + \left(\langle r_{124y} \rangle_t - \langle r_{338y} \rangle_t + \Delta r_{124y} - \Delta r_{338y} \right)^2 \\ &\quad + \left(\langle r_{124z} \rangle_t - \langle r_{338z} \rangle_t + \Delta r_{124z} - \Delta r_{338z} \right)^2. \end{aligned}$$

We define $\delta_{i,x} := v_{i,124x} - v_{i,338x}$ and $\xi_x := \langle r_{124x} \rangle_t - \langle r_{338x} \rangle_t$, and similarly for y and z ; then we can write

$$r_{124x} - r_{338x} = \xi_x + \delta_{1,x}p_1 + \delta_{2,x}p_2 + \cdots + \delta_{f,x}p_f = \xi_x + \sum_{c=1}^f \delta_{c,x}p_c$$

and similarly for y and z . The square of these values is

$$(r_{124x} - r_{338x})^2 = \xi_x^2 + 2 \sum_{c=1}^f \xi_x \delta_{c,x} p_c + \sum_{c_2=1}^f \sum_{c_1=1}^f \delta_{c_1,x} \delta_{c_2,x} p_{c_1} p_{c_2},$$

etc. By defining

$$S := \xi_x^2 + \xi_y^2 + \xi_z^2 = \left\langle d_{124,338} \right\rangle_t^2 \quad (\text{II.4})$$

$$R_c := 2(\xi_x \delta_{c,x} + \xi_y \delta_{c,y} + \xi_z \delta_{c,z}) \quad (\text{II.5})$$

$$Q_{c_1 c_2} := \delta_{c_1,x} \delta_{c_2,x} + \delta_{c_1,y} \delta_{c_2,y} + \delta_{c_1,z} \delta_{c_2,z} \quad (\text{II.6})$$

we can rewrite Equation (II.3) as

$$\left[d_{124,338}(t) \right]^2 = S + \sum_{c=1}^f R_c p_c + \sum_{c_2=1}^f \sum_{c_1=1}^f Q_{c_1 c_2} p_{c_1} p_{c_2}. \quad (\text{II.7})$$

We can calculate the time-independent S , $\mathbf{R} := [R_c]$, and $\mathbf{Q} := [Q_{c_1 c_2}]$ simply by looking at the average structure $\langle \mathbf{r} \rangle_t$ and the transformation matrix \mathbf{T} . Note that the square of the distance, $\left[d_{124,338}(t) \right]^2$, is not simply a linear combination of the projections $p_c(t)$, but also has cross-terms in the product of two projections $p_{c_1}(t)p_{c_2}(t)$.

Alternatively, this squared distance can be equated to

$$\begin{aligned}
 \left[d_{124,338}(t) \right]^2 &= \sum_{\alpha=x,y,z} \left(\xi_{\alpha} + \sum_{c=1}^f \delta_{c,\alpha} p_c \right)^2 \\
 &= \sum_{\alpha=x,y,z} \xi_{\alpha}^2 + 2 \sum_{\alpha=x,y,z} \xi_{\alpha} \left(\sum_{c=1}^f \delta_{c,\alpha} p_c \right) \\
 &\quad + \sum_{\alpha=x,y,z} \left[\left(\sum_{c=1}^f \delta_{c,\alpha} p_c \right)^2 \right]
 \end{aligned} \tag{II.8}$$

Equations (II.7) and (II.8) have equivalent parts: the squared average distance $S = \left\langle d_{124,338} \right\rangle_t^2$ is $\sum_{\alpha} \xi_{\alpha}^2$; the linear part $\sum_c R_c p_c$ is $2 \sum_{\alpha} \xi_{\alpha} (\sum_c \delta_{c,\alpha} p_c)$; and the cross-term part $\sum_{c_2} \sum_{c_1} Q_{c_1 c_2} p_{c_1} p_{c_2}$ is $\sum_{\alpha} \left[(\sum_c \delta_{c,\alpha} p_c)^2 \right]$. Because of this last correspondence, we expect to see that the cross-term part will always be larger than zero; this is indeed what we see in the Results section.

II.D Results

II.D.1 Stability of trajectory and mobility of residues

Figure II.1 shows the solute potential energy of the 10.8 ns trajectory. After the first 700 ps, the solute potential energy ended its decreasing trend and fluctuated around $75.9 \text{ MJ} \cdot \text{mol}^{-1}$. This is one of our reasons for discarding the first 700 ps of trajectory and starting the equilibrium statistics thereafter.

Another justification for discarding the first 700 ps comes from Figure II.2, where we plot the solute potential energy with the gorge proper radius ρ . The points from the first 700 ps cluster are distinct from the rest of the trajectory for their high energies and small gorge radii. This suggests that the mACH molecule relaxes from the conformation in the crystal structure 1MAH with higher energy and smaller gorge proper radius to one that has a wider gorge and is lower in energy.

The root mean square deviation (rmsd) from the crystal structure through the 10 ns trajectory is shown in Figure II.3. The rmsd for the α -carbon atoms kept stable around 120 pm, and that for all heavy atoms maintained at 170 pm.

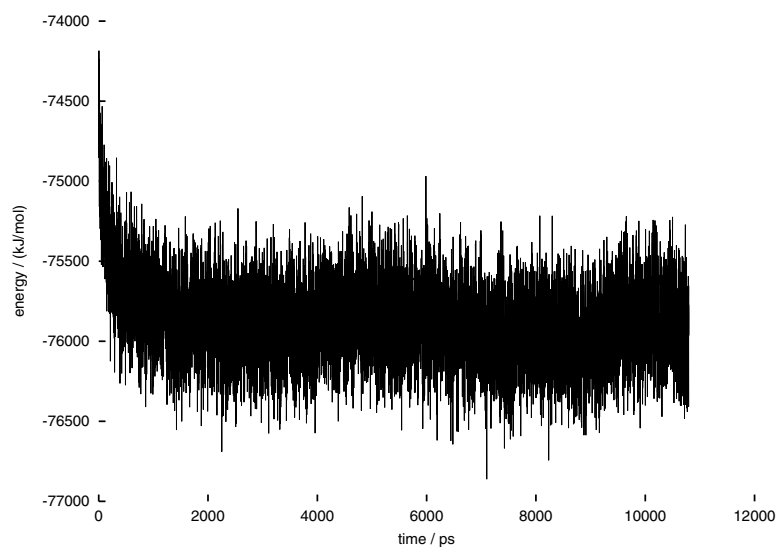


Figure II.1: The solute potential energy for the 10.8 ns trajectory.

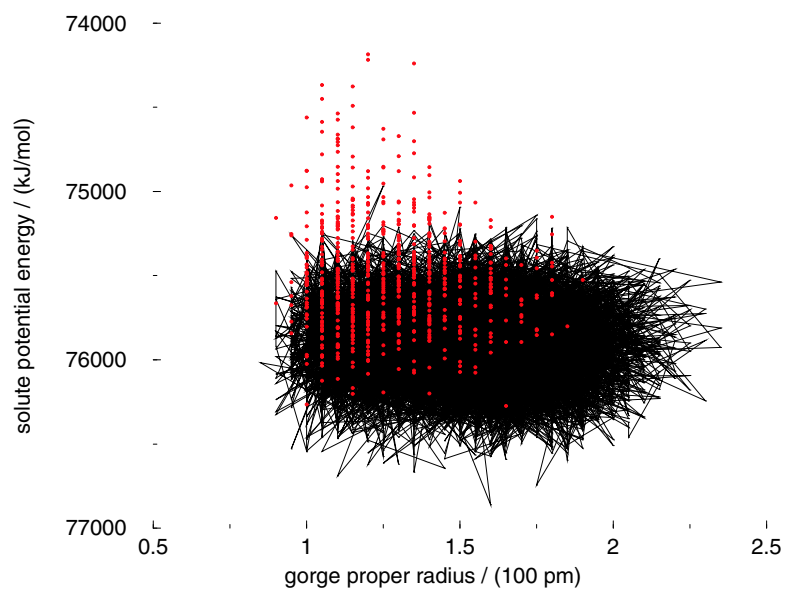


Figure II.2: The solute potential energy versus the gorge proper radius ρ . The red dots are the first 700 ps of trajectory. The black dots are the following 10 ns of trajectory, with the adjacent frames connected with lines.

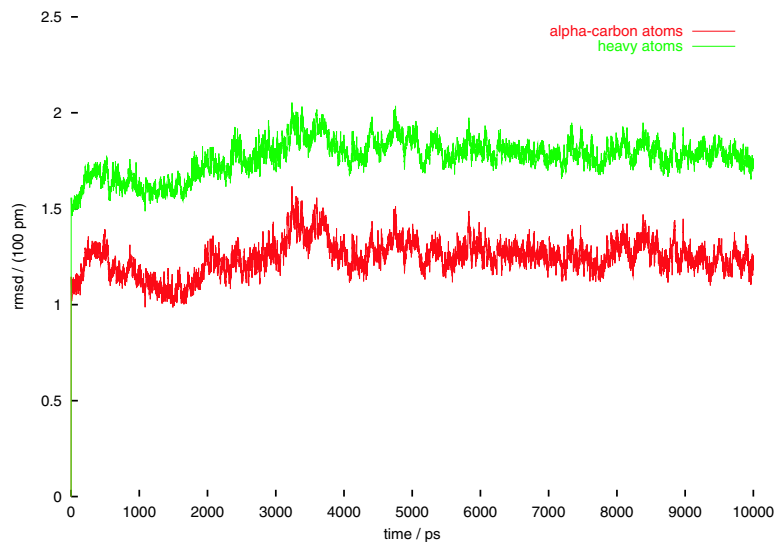


Figure II.3: Time dependence of the root mean square deviations (rmsd) for the 10 ns mACH E MD trajectory, using the mACH E part in the 1MAH crystal structure as reference. Red, rmsd for alpha-carbon atoms; green, rmsd for heavy atoms.

The temperature, the total energy, the mass density, and the volume during the 10 ns trajectory remained stable. The energy components were inspected to ensure the stability of the trajectory.

The isotropic temperature (B) factor can be calculated from the mean square fluctuation (msf) [14, 23] using the equation

$$B = \frac{8\pi^2}{3} (\text{msf}). \quad (\text{II.9})$$

The B factor for each residue from the mACH E part in the 1MAH crystal structure and that calculated from the msf in the MD simulation are shown in Figure II.4.

The time-averaged rmsd for each residue, using the mACH E part in the 1MAH crystal structure as the reference was also calculated; it showed similar features as the simulated B factor (data not shown). Overall we do not observe outstanding fluctuations in the gorge region over other parts of the protein.

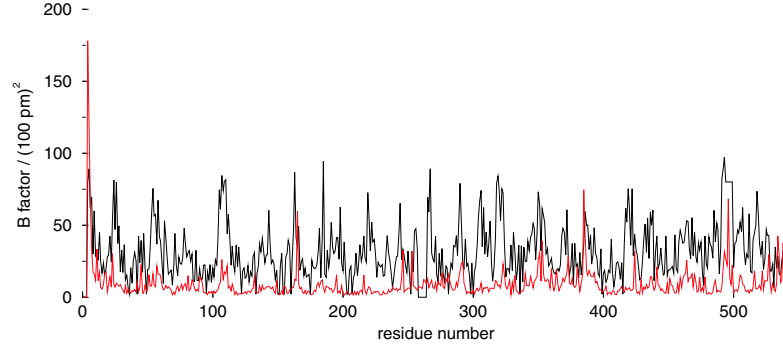


Figure II.4: The B factor for each residue from the mACH E part in the 1MAH crystal structure. Black, crystal structure; red, calculated from the msf in the 10 ns MD trajectory.

II.D.2 Back door opening events

In the 10 000 frames analyzed, only 78 had back door openings (Figure II.5). We compared $Y(t)$ with the dihedral angle values in the residues that form the back door, namely, Trp 86, Gly 448, Tyr 449, and Ile 451. The most important ones are shown in Figure II.6.

II.D.3 Correlation and covariance analyses

The 10 ns time series for the gorge proper radius $\rho(t)$ is shown in Figure II.7. The average of the proper radius is 152 pm. The probability distribution over all observed values of ρ is not Gaussian, as previously described [32].

We define the correlation between the i th degree of freedom, $r_i(t)$, and the gorge proper radius $\rho(t)$ to be

$$\frac{\langle (r_i(t) - \langle r_i \rangle_t) (\rho(t) - \langle \rho \rangle_t) \rangle_t}{\sqrt{\langle (r_i(t) - \langle r_i \rangle_t)^2 \rangle_t \langle (\rho(t) - \langle \rho \rangle_t)^2 \rangle_t}}. \quad (\text{II.10})$$

We calculated a correlation vector with 3 entries thus defined for the α -carbon atom of each residue (Figure II.8). Also, we calculated the average correlation vector within each of the secondary structure elements (α -helices and β -strands; Figure II.9).

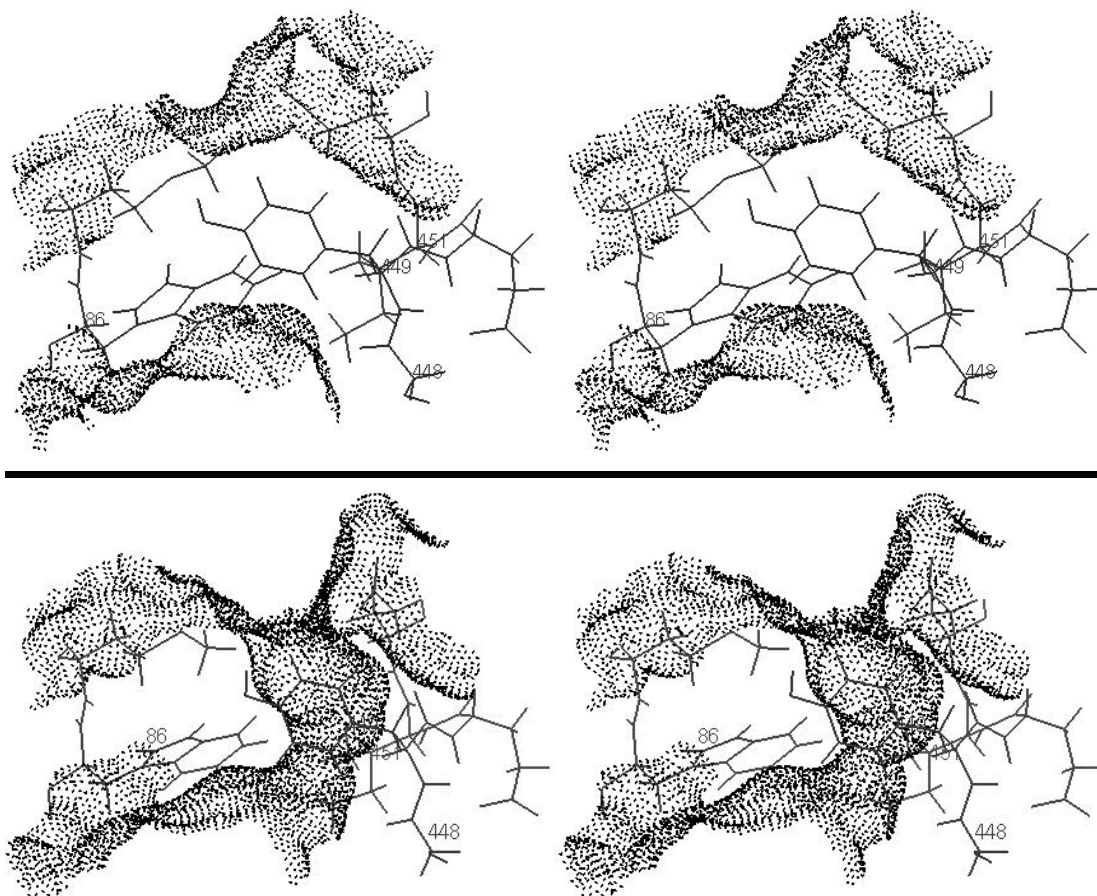


Figure II.5: Stereographs of two conformations in the back door region. In each conformation, the outside of the protein is on the top; Trp 86 is on the lower-left, Gly 448 on the lower-right, and Tyr 449 in the middle. The Connolly surface generated with a probe radius of 140 pm is shown. Top: the frame at 291 ps, showing a closed back door. In this frame, χ_2 of Trp 86 is 114° , ψ of Gly 448 is 86° , χ_1 of Tyr 449 is -121° , χ_1 of Ile 451 is -72° , and χ_2 of Ile 451 is 161° . Bottom: the frame at 8996 ps, showing an open back door. In this frame, χ_2 of Trp 86 is 120° , ψ of Gly 448 is 65° , χ_1 of Tyr 449 is -122° , χ_1 of Ile 451 is -64° , and χ_2 of Ile 451 is 163° .

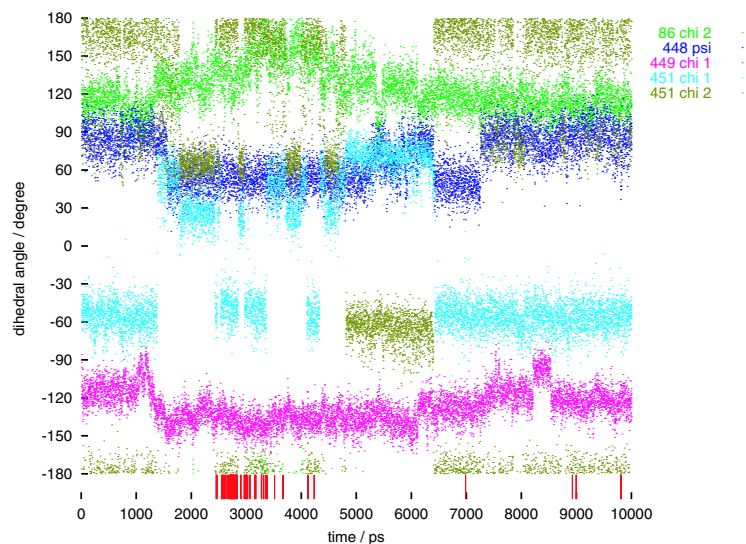


Figure II.6: Selected dihedral angles through the 10 ns that are important to the opening of the back door. The red lines at the bottom mark the back door opening events. The dots are the dihedral angles: χ_2 of Trp 86 (green); ψ of Gly 448 (blue); χ_1 of Tyr 449 (pink); χ_1 of Ile 451 (cyan); χ_2 of Ile 451 (brown).

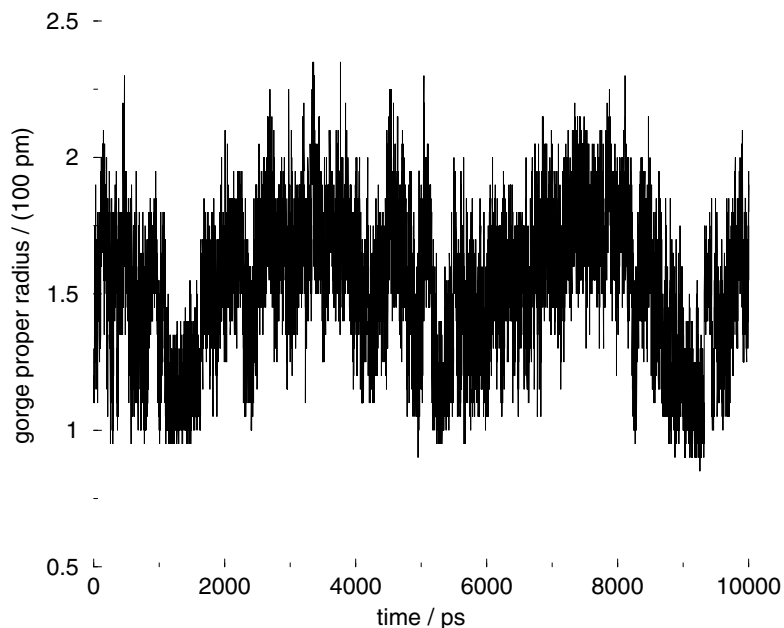


Figure II.7: The 10 ns time series for the gorge proper radius, $\rho(t)$.

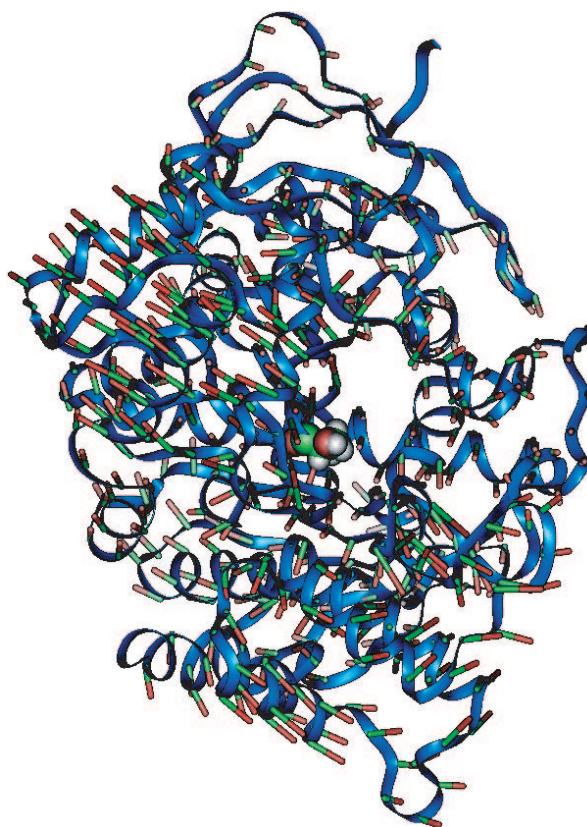


Figure II.8: The correlation vector for each residue displayed on the initial structure (see text for definition). The vectors point from green to red; the lengths are in arbitrary units. The AChE molecule is shown in the conventional orientation: the viewer looks down the gorge, with the *N*-terminus on the top of the figure and the *C*-terminus at the lower-left corner. The active site Ser 203 is shown in the space-filling model.

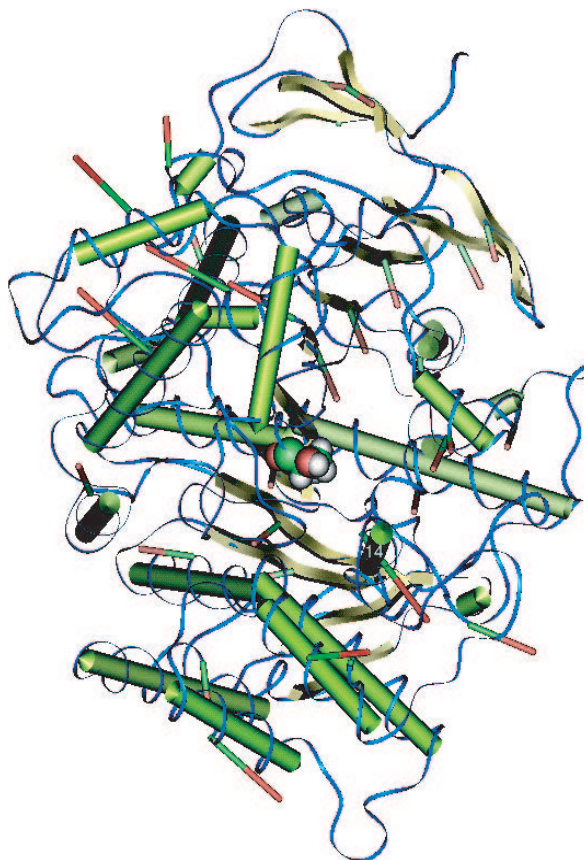


Figure II.9: The correlation vector within each secondary structure element displayed on the initial structure (see text for definition). The α -helices are shown as green cylinders; the β -strands are shown in yellow. The vectors point from green to red; the lengths are in arbitrary units. The AChE molecule is shown in the conventional orientation: the viewer looks down the gorge, with the *N*-terminus on the top of the figure and the *C*-terminus at the lower-left corner. The active site Ser 203 is shown in the space-filling model. Helix 14 is marked with numerals '14'.

Similarly, the average velocity covariance is defined as

$$\langle (r_i(t) - r_i(t - 1 \text{ ps})) (\rho(t) - \rho(t - 1 \text{ ps})) \rangle_t \quad (\text{II.11})$$

The average velocity covariance vector is shown in Figure II.10.

II.D.4 Principal component analysis and backprojecting

We found that the distance between Phe 338 C_{ε2} and Tyr 124 O_H and the gorge proper radius are highly correlated, with a correlation coefficient of 0.91 (Figure II.11); the correlation coefficient between the distance Phe 338 C_α–Tyr 124 C_α and the gorge proper radius is 0.55.

We calculated the time-dependent contributions to $\left[d_{124,338}(t) \right]^2$, namely, the linear part $\sum_c R_c p_c(t)$ and the cross-term part $\sum_{c_1} \sum_{c_2} Q_{c_1 c_2} p_{c_1}(t) p_{c_2}(t)$ (Figure II.12). Note that sometimes the linear part and the cross-term part have comparable magnitudes but opposite directions, for example, around 8.1 ns.

II.E Discussion

II.E.1 *B* factors

The crystallographic *B* factors include a variety of contributions (e.g., crystal contacts, static disorder in the crystal) in addition to that from the dynamical fluctuations, and these additional contributions are expected to be substantial for a structure of modest resolution [33]. The crystallographic resolution is 0.32 nm (3.2 Å) for the structure 1MAH [28]. Generally the crystallographic *B* factors were larger than those observed in MD because the simulation sampled far fewer conformations of the protein than crystallography; the termini, however, exhibited larger *B* factors in the MD simulation where the protein is solvated in water rather than packed in a crystal.

In the original crystal structure [28], loop II of Fas2 interacts with the peripheral anionic site of mAChE, thereby blocking substrate access to the active site; loop I of



Figure II.10: The average velocity covariance vector for each residue displayed on the initial structure (see text for definition). The vectors point from green to red; the lengths are in arbitrary units. The AChE molecule is shown in the conventional orientation: the viewer looks down the gorge, with the *N*-terminus on the top of the figure and the *C*-terminus at the lower-left corner. The active site Ser 203 is shown in the space-filling model.

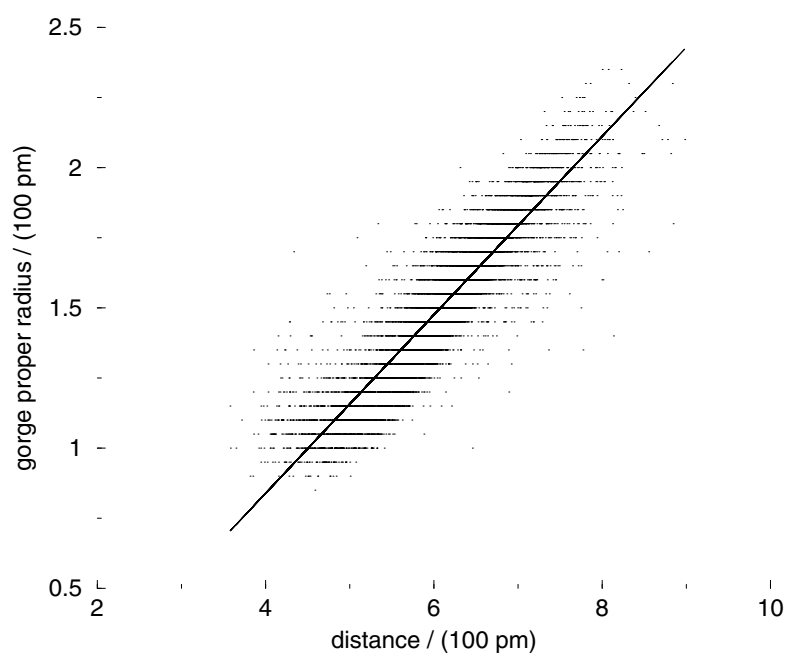


Figure II.11: The gorge proper radius ρ versus the distance between Phe 338 C ϵ_2 and Tyr 124 O_H. The correlation coefficient is 0.91.

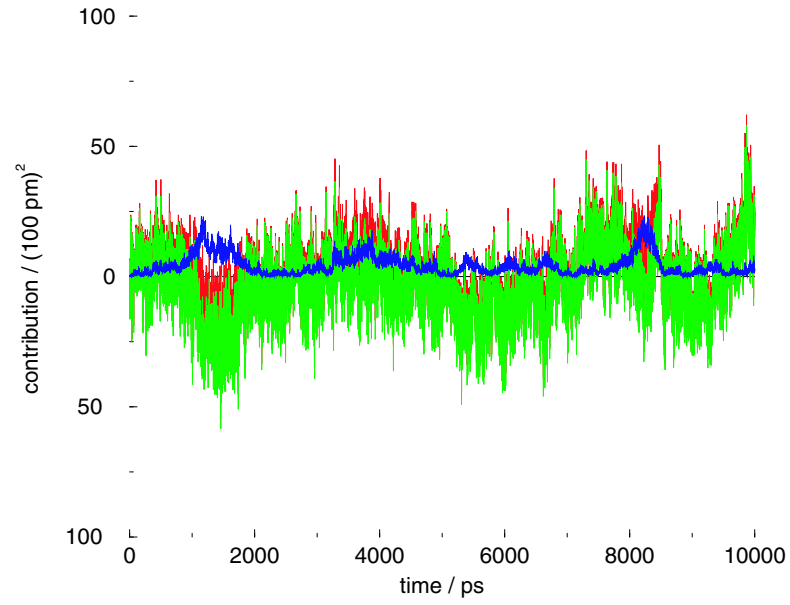


Figure II.12: Contribution of linear ($\sum_c R_c p_c(t)$, green) and cross ($\sum_{c_1} \sum_{c_2} Q_{c_1 c_2} p_{c_1}(t) p_{c_2}(t)$, blue) terms to the square distance $\left[d_{124,338}(t) \right]^2$, and the sum of these two (red). See text for definitions.

Fas2 fits in a crevice near the entrance of the gorge. Our simulation starts from this crystal structure, with the inhibitor Fas2 removed. However, we do not see larger B factors in MD than in the crystal structure for the residues involved in contact with Fas2; this is probably due to the same reasons mentioned in the previous paragraph. Nor were any outstanding deviations observed in the Fas2 contact interface in the time-averaged rmsd for each residue.

II.E.2 Access to the active site

Unlike the previous 0.5 ns MD simulation on the *Torpedo californica* AChE (*TcAChE*) complexed with tacrine [25], our simulation showed a non-Gaussian probability distribution of the gorge proper radius as previously described [32]. In addition, our average radius, 152 pm, was smaller than that in the tacrine-complexed *TcAChE* simulation (about 190 pm). The time series $\rho(t)$ almost never reached the 240 pm; for a substrate as large as acetylcholine, AChE hardly allowed it any spontaneous access to the active site during the 10 ns trajectory.

The presence of the ligand tacrine in the gorge may be the reason for the larger proper radius in the tacrine-complexed *TcAChE* simulation. Favorable electrostatic interactions between AChE and its substrate may help in overcoming the difficulty of squeezing through a narrow gorge. Note that the catalysis of AChE occurs on a millisecond time-scale; as long as the frequency of gorge opening is not so low that the substrate diffuses away from the gorge entrance before commitment to catalysis, rarity of opening in this nanosecond simulation does not preclude diffusion-controlled kinetics.

II.E.3 Back door opening events

The proposition for the existence of the back door has been based on visual observation of the crystal structure [34] and supported by conformations sampled by simulations of *TcAChE* [24, 35]. In our simulation, although only 78 frames out of our 10 ns trajectory

had back door opening events, the back door opening observed here aligned sequentially with that observed in the MD simulation of *TcAChE*: Trp 86, Gly 448, and Tyr 449 in mAChE correspond respectively to Trp 84, Gly 441, and Tyr 442 in *TcAChE*. This is a remarkable fact: this alternative opening, named the back door, is not limited to a single species, but has been observed by molecular dynamics simulations in at least two species.

The selected dihedral angles in the region, as shown, have preferred values when the back door opens. For most of the opening events, e.g., around 3 ns, χ_2 of Trp 86 acquires higher values around 150° than the usual values around 110° . Back door opening is more likely to happen when ψ of Gly 448 assumes a value around 45° rather than around 80° , and when χ_1 of Tyr 449 is around -140° rather than -120° . Four major types of rotamers for the χ_1 and χ_2 of Ile 451 are observed: (i) ($\chi_1 \approx -60^\circ, \chi_2 \approx \pm 180^\circ$), or (*-gauche, trans*); observed most often in this trajectory, this seems to be almost a necessary, but not sufficient, condition for back door opening. (ii) ($\chi_1 \approx 30^\circ, \chi_2 \approx 60^\circ$), or (*+gauche, +gauche*); observed sporadically in the first half of the trajectory, it is interspersed between opening events. (iii) ($\chi_1 \approx 60^\circ, \chi_2 \approx -60^\circ$), or (*+gauche, -gauche*); observed around 5 ns and 6 ns, this rotamer does not give any opening events. (iv) ($\chi_1 \approx -60^\circ, \chi_2 \approx 60^\circ$), or (*-gauche, +gauche*); observed after 7 ns, this rotamer also does not give any opening events.

It is difficult to be conclusive about preferred dihedral angle values for back door opening for the following reasons: We only have a small number of opening events. In addition, some of the opening events in the last 2 ns of the simulation have violations of preferred dihedral angle values; for example, the two conformations shown in Figure II.5 have subtly different values for these dihedral angles, but the one at 8996 ps has an open back door but that at 291 ps does not.

Site-directed mutagenesis experiments on human AChE [36] and *TcAChE* [35] do not support significant participation of back door traffic in catalytic activities. On the other hand, there are recent experimental evidences from two different methods supporting the back door hypothesis: product clearance through the back door is implied

by the crystal structure of a carbamoylated *TcAChE* [37]; one inhibitory monoclonal antibody of *Electrophorus* AChE is reported to bind to the region of the back door [38]. It is our view that one has to be cautious while attempting to interpret and reconcile these data concerning the back door, and take into consideration the time-scale of each method of observation. Indeed, even this simulation of 10 ns only covers a fraction of a thousandth of a catalytic cycle of AChE. Despite consistently observing conformations with an open back door in several MD simulations, we cannot ascertain details of the involvement of the back door in AChE catalytic function.

II.E.4 Correlation and covariance analyses

We have found that the “porcupine plots” (Figures II.8, II.9 and II.10) are very helpful in visualizing the concerted motions between parts of the protein and the functionally interesting motion, the gorge opening. The correlation vectors in Figure II.8 reveal how much each residue moves in concert with the gorge. Note that a correlation vector does not show how much the residue fluctuates or how flexible it is, but how it moves from its average position when the gorge changes in proper radius. The moiety of AChE that includes the gorge (the half of the protein that is closer to the viewer in the figures) has remarkable concerted motion with the gorge proper radius. The residues in this moiety generally have correlation vectors pointing away from the gorge. These residues apparently move away from the gorge when the gorge opens. Some residues that are in the other moiety (closer to the base of the gorge and further from the viewer) have correlation vectors that are generally smaller. The discrimination of these concerted motions is even more pronounced in Figure II.10: the residues that construct the gorge itself have the largest average velocity covariance vectors, while those farthest from the gorge have the smallest average velocity covariance vectors. We introduce Figure II.9 as an easy way to visualize and interpret how the secondary structure elements contribute to the opening of the gorge. For example, helix 14 (Gly 335 to Tyr 341) is close to the active site gorge; it has a large vector in this figure pointing away from the gorge, which means it moves away when the gorge opens. This helix includes Phe 338, one

of the two residues whose separation correlates well with the gorge proper radius, as described above. Most of the α -helices in the same moiety as the gorge move away from the gorge; those further from the gorge show little concerted motion. The helices and two large β -sheets (B and C) in the other moiety, which is at the bottom of the gorge, generally have upward motion towards the gorge as the latter opens.

We speculate that inhibitors such as Fas2 may decrease the likelihood of gorge opening by restricting groups on the surface of AChE that have large concerted motions, in addition to sterically occluding the entrance to the gorge. Other allosteric inhibition mechanisms are also possible. These remain to be investigated and confirmed by our current work on the MD simulation of the complex of Fas2 and mAChE. We understand that *in vivo* AChE exists in cholinergic synapses as oligomers indirectly anchored on the post-synaptic membrane. These attachments to the AChE monomer are not represented in this simulation; they may also modulate the opening behavior of the gorge.

II.E.5 Contributions of the principal components in gorge opening

Several convincing pieces of evidence support a complex opening behavior of the gorge. Starting from a naïve guess that one single principal component or just a few, representing a large collective motion in the protein, has a dominant contribution in the gorge opening behavior, we shall now enumerate evidence to demonstrate the contrary.

There is a high correlation (0.91) between the Phe 338 C _{ϵ 2}–Tyr 124 O_H distance and the gorge proper radius; this distance alone may be used to predict the gorge proper radius with high confidence. The corresponding α -carbon distance has a lower correlation coefficient (0.55). The side chains seem to contribute significantly to the opening of the gorge. As these particular side chains project directly toward the gorge and actually constitute the bottleneck much of the time, it makes sense that the correlation of the side chain distance and the gorge radius will be particularly strong. A predictive model of the gorge width with high accuracy will thus have to include the side chains into consideration; for that purpose, it is inappropriate to only concentrate on large backbone motions and ignore those of the side chains. On the other hand, the largest fluctuations

in the gorge radius can be expected to reflect movement of backbone segments, and we investigate these in the current work. Ligands larger than acetylcholine do bind to the active site, including a number of important inhibitors, and with the backbone correlation analysis we are beginning to explore the mechanism of such processes.

The eigenvalues from the PCA, ranked by magnitude, decrease rapidly: the 15th largest eigenvalue is less than one-tenth (0.1) of the largest, and the 113rd largest is less than one-hundredth (0.01) of the largest. In spite of this, there is not one principal component that has an outstandingly high correlation with $\rho(t)$; in other words, no one principal component dominates the opening of the gorge. The naïve guess expects dismissible cross-term parts ($\sum_{c_2} \sum_{c_1} Q_{c_1 c_2} p_{c_1} p_{c_2}$) in the backprojecting expression (Equation II.7); in addition, it expects the linear part ($\sum_c R_c p_c(t)$) to have one dominant term with a large coefficient R_c , while all other terms have small coefficients. Contrary to this expectation, when ranked by magnitude, there was not a dominant minority of terms that stand out in the list of the R_c coefficients; indeed, none of the $R_c p_c(t)$ terms in the linear part are dominant (data not shown). It is not possible to single out principal components that dominate the width of the gorge.

Furthermore, we saw in Figure II.12 that a model that ignores the contribution of either the cross-term part or the linear part to the gorge opening behavior is not justified. Both the linear part and the cross-term part contribute significantly to fluctuations in the width of the gorge. In sum, the naïve guess that a few principal components dominate the gorge is not justified.

We conjecture that this finding is related to our fractal dynamics model previously proposed [32]. In that model, the time-dependent fluctuation of gorge proper radius reveals fractal dynamics that lacks a characteristic time-scale over the several orders of magnitude being observed. We suggested that this behavior is caused by a hierarchy of motions on different time-scales acting together. It is likely that these motions are related to our present results, where many motions on different length-scales (as revealed by PCA) have a similar effect on the gorge behavior.

As a side note, we did attempt to perform energy landscape analysis [39–41] by

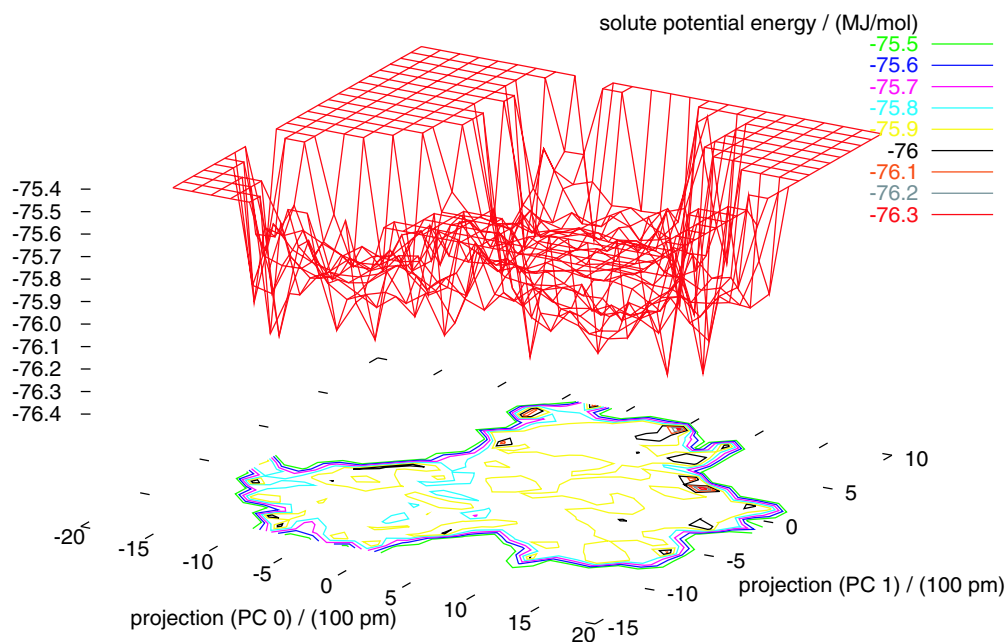


Figure II.13: The solute potential energy projected onto a histogram of the first two principal components.

projecting of the solute potential energy onto the first two principal components obtained from PCA (Figure II.13). For a protein as large as AChE, our 10 000 frames did not provide enough sampling to show a meaningful energy landscape. Comparison between the solute potential energy and the gorge proper radius was also inconclusive, likely for the same reason.

II.F Conclusions

The 10 ns MD simulation of mAChE was equilibrated and stable as shown by various properties and energy components, and gave reasonable B factors.

The small fraction of total number of frames in which we observed an open back door severely limits the statistics of our analysis. Back door opening seems to prefer

certain dihedral angle values for some of the residues in the region.

We developed the “porcupine plots” to visualize the concerted motions between residues in AChE and the gorge width. The plots show that residues lining the gorge have the largest velocity covariance with the gorge, and residues in the same moiety as the gorge move concertedly away from the gorge when it opens. This clearly reveals the residues involved in gorge opening, and gives the magnitude and direction of such involvement.

We have found that the Phe 338 C_{ε2}–Tyr 124 O_H distance is highly predictive of the gorge proper radius; the corresponding α -carbon distance has a moderate correlation. We have not investigated side chain motions extensively in this paper, but side chains will be important in a predictive model of the gorge opening.

Principal component analysis showed that the gorge proper radius is determined by motions on many different length-scales; this is likely to be related to the fractal dynamics model we previously proposed.

II.G Acknowledgments

We thank Dr Tjerk P. Straatsma for providing and maintaining the NWChem software and Dr Sylvia Tara for setting up and equilibrating the MD simulation. We also thank Prof. Nathan Baker, Dr Yves Bourne, Dr Pascale Marchot, Dr Zoran Radić, and Prof. Palmer Taylor for assistance and fruitful discussions. We especially thank Dr Richard Henchman for inspiration in developing the porcupine plots. Gratitude is expressed to Accelrys, San Diego, for generously providing us with the *Insight II* software. This project was supported in part by the Howard Hughes Medical Institute, W. M. Keck Foundation, San Diego Supercomputer Center, National Science Foundation, and National Institutes of Health.

This chapter contains the same material as an article that appeared in the *Biophysical Journal* [2], of which I am the primary author.

III

Mechanism of acetylcholinesterase inhibition by fasciculin: 5 ns molecular dynamics simulation



III.A Abstract

Our previous molecular dynamics simulation (10 ns) of mouse acetylcholinesterase (EC 3.1.1.7) revealed complex fluctuation of the enzyme active site gorge. Now we report a 5 ns simulation of acetylcholinesterase complexed with fasciculin 2. Fasciculin 2 binds to the gorge entrance of acetylcholinesterase with excellent complementarity and many

This chapter is reproduced with permission from Tai, K.; Shen, T.; Henschman, R. H.; Bourne, Y.; Marchot, P.; McCammon, J. A. *J. Am. Chem. Soc.* **2002**, *124*, 6153–6161. Copyright © 2002 American Chemical Society.

polar and hydrophobic interactions. In this simulation of the protein–protein complex, where fasciculin 2 appears to sterically block access of ligands to the gorge, again we observe a two-peaked probability distribution of the gorge width. When fasciculin is present, the gorge width distribution is altered such that the gorge is more likely to be narrow. Moreover, there are large increases in the opening of alternative passages, namely the side door (near Thr 75) and the back door (near Tyr 449). Finally, the catalytic triad arrangement in the acetylcholinesterase active site is disrupted with fasciculin bound. These data support that, in addition to the steric obstruction seen in the crystal structure, fasciculin may inhibit acetylcholinesterase by combined allosteric and dynamical means.

III.B Introduction

Acetylcholinesterase (AChE; EC 3.1.1.7) terminates synaptic transmission at cholinergic synapses by catalyzing hydrolysis of the neurotransmitter acetylcholine [4]. A gorge, 2 nm in depth, leads from the surface of the enzyme to its buried active site. Fasciculin 2 (Fas2), a peptidic three-finger snake toxin (61 residues) from green mamba (*Dendroaspis angusticeps*) venom, is a picomolar inhibitor of mammalian acetylcholinesterases.

Much kinetics and structural information for the fasciculin 2-mouse acetylcholinesterase complex (Fas2-mAChE) has been collected in the past decade. Some kinetic data suggested that the inhibition may be achieved by steric obstruction: Fas2 capping the entrance of the gorge, sterically blocking the entry of the ligand [42]. The crystallographic structures of complexes of Fas2 with mouse acetylcholinesterase (mAChE) [28], *Torpedo californica* AChE [43], and human AChE [44] all supported this hypothesis, and showed excellent surface complementarity between Fas2 and AChE. The contacts between Fas2 and mAChE are in turn verified by mutation studies [45–47].

In the crystal structures, allosteric effects seem to be subtle at most. However, this has not been fully reconciled with kinetics information, which shows residual catalytic

activity for the Fas2-bound enzyme. Indeed, inhibition of AChE by fasciculin, despite its high affinity and slow rate of dissociation, is not complete, and the fractional residual activity reveals that substrates can still enter the active site in Fas2-bound AChE [45, 48–51]. With certain AChE mutants and substrates whose catalysis is not diffusion limited, Fas2 even acts as an allosteric activator [52], connoting possible influence by Fas2 on alternative passages and other interaction in addition to direct steric occlusion. Moreover, it has been suggested that Fas2 alters the conformation of AChE in the active site [49] and in the Ω loop (Cys 69 to Cys 96) [28, 53–55], particularly that of the Trp 86 side chain [52].

We have previously carried out a 10 ns molecular dynamics (MD) simulation of mAChE [2]. This has revealed the complex nature of the gorge fluctuations. Collective motions on many scales contribute to the opening behavior of the gorge, and two distinct states, one narrow and one wide, were found. Correlation results identified the motions of many protein residues as the gorge opens. In particular, the residues within the mAChE moiety that includes the gorge apparently move away from the gorge entrance when the gorge opens. The opening of alternative passages to the active site was found to be infrequent, since less than one-hundredth of the frames collected showed opening of alternative passages. These alternative passages are the back door, bounded by residues Trp 86, Tyr 449, and Ile 451 [24]; and the side door, by residues Thr 75, Leu 76, and Thr 83 [25, 27].

To investigate the structural and dynamical effect of Fas2 binding on mAChE, we performed another MD simulation of the mAChE complexed with Fas2 and compare mAChE properties with the results from the previous apo-mAChE trajectory.

III.C Methods

III.C.1 Crystal structure

The crystal structure of the Fas2-mAChE complex used for this study (Protein Data Bank identification code: 1KU6) was refined to 0.25 nm (2.5 Å) resolution. It con-

tains one Fas2 molecule (residues 1–61) bound to one mAChE monomer (residues 3–541), one GlcNAc moiety linked to mAChE residue Asn 350, one ethylene glycol and 189 water molecules. The overall deviations from ideal geometry are 0.010 Å for bond distances and 1.76° for bond angles. This structure, though virtually identical to the previous complex structure 1MAH [28] with an average root mean square deviation (rmsd) of 0.57 Å for 587 C α atoms, provides significantly improved accuracy in the positions of the main and side chains of Fas2 and mAChE and of those located at the complex interface, and unambiguously reveals the position of a higher number of water molecules. A detailed description of this structure including a report on the crystallization and data collection conditions will be published elsewhere.

III.C.2 Molecular dynamics simulation

The 0.25 nm crystal structure of Fas2-mAChE described above was used to build the initial structure (Figures III.1 and III.2). In addition to the Fas2 and mAChE molecules themselves, the 189 crystallographic water molecules present in the structure were left intact and considered part of the solvent throughout the following preparation.

To mend the missing or truncated residues and segments of the Fas2-mAChE crystal structure 1KU6, we used mAChE segment Pro 258–Gly 264 from the mAChE crystal structure (1MAA) [57]; mAChE residues Lys 496, Ala 542, and Thr 543 from the previous Fas2-mAChE crystal structure (1MAH); and Fas2 residue Lys 51 from the unliganded Fas2 crystal structure (1FSC) [58]. The mAChE residue Arg 493, which in the structure was modeled as an alanine residue due to side chain mobility, was kept unchanged, following our previous simulation of mAChE [2, 27]. In the end, the prepared structure has the same mAChE atoms as our previous apo-mAChE MD. These structure manipulations were carried out using *Insight II* (Accelrys, San Diego, California).

The following preparation, minimization and MD procedures were performed using NWChem version 4.0 [20], using the AMBER 94 force field [12] for the solutes (proteins and counterions), and SPC/E [13] for the water molecules.

Hydrogen was added to the structure using the prepare module of NWChem. To

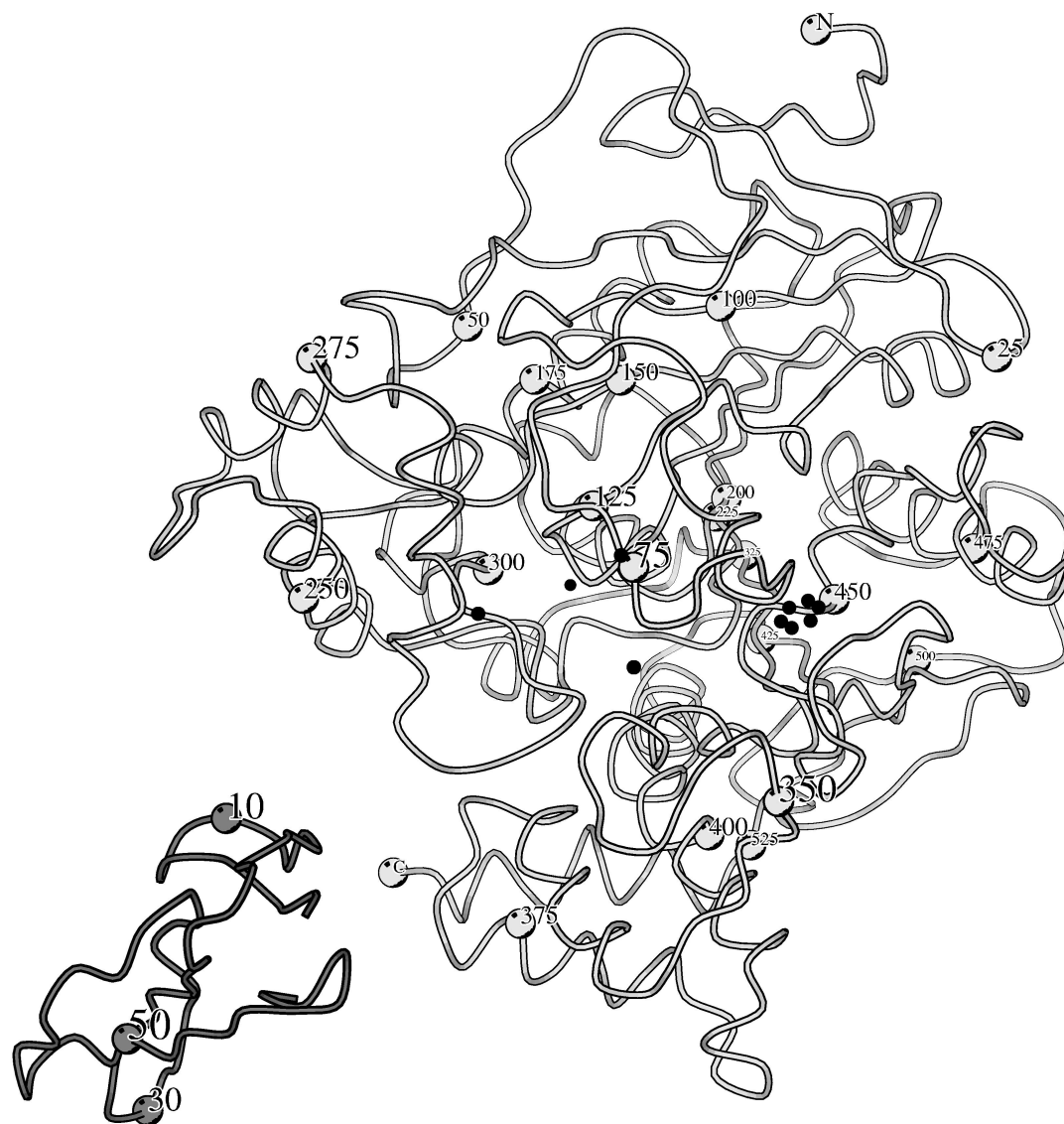


Figure III.1: Overview of the Fas2-mAChE complex structure (1KU6). The mAChE molecule is labeled every 25 residues; the Fas2 molecule, moved from the mAChE for the sake of clarity, has residues 10 (in loop I), 30 (in loop II) and 50 (in loop III) labeled. The mAChE atoms that are used to define the blocking sphere (see Methods) for each passage are marked with small spheres: gorge (Tyr 72 O_H, Leu 76 C_{δ1}, Trp 286 C_β); side door (Thr 75 C_β); back door (Tyr 449 6-membered ring). Generated using Molscript [56].

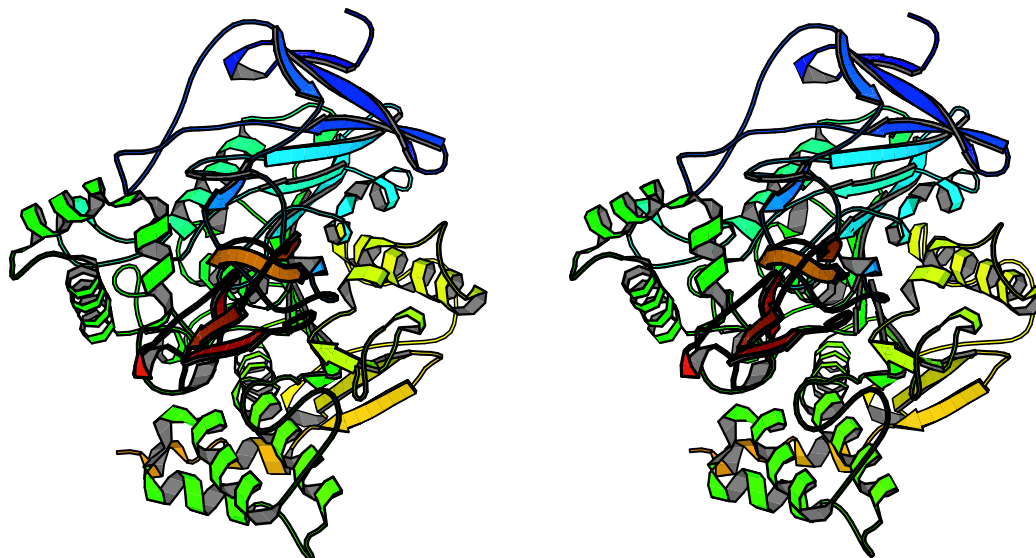


Figure III.2: Stereograph of the secondary-structure representation the Fas2-mAChE crystal structure (1KU6). The mAChE molecule is gradually colored from blue (*N*-terminus; residue 4) to light orange (*C*-terminus; residue 543). The Fas2 molecule is closer to the viewer, colored from dark orange (*N*-terminus; residue 1) to red (*C*-terminus; residue 61). Generated using Molscript [56].

neutralize the -6 charge of the Fas2-mAChE complex, 6 sodium counterions were added; in addition to the sodium ion in the active site as in the previous simulation of apo-mAChE [2, 27], the position of the other 5 counterions are analogous to those farthest from Fas2 in the previous mAChE simulation. The longest dimension of the molecule is 8.4 nm at this point. The molecule is then solvated in a cubic box of water molecules with length 10.5 nm on each side.

The MD simulation was performed in the isothermal-isobaric ensemble. The solvent and solute were separately coupled to temperature reservoirs of 298.15 K with coupling times of 0.1 ps; pressure was restrained to 1.025×10^5 Pa with a coupling time of 0.5 ps [59]. The MD simulation time step was 2 fs for both equilibration and production. Long-range electrostatic interactions were calculated using particle-mesh Ewald summation [19]. Bond lengths between hydrogens and heavy atoms were constrained using SHAKE [17, 18].

The water molecules were relaxed using steepest descent for 5 000 steps, and equilibrated at 298.15 K for 100 ps. The whole MD simulation system contained 540 residues (residues 4 to 543; 8 279 atoms) for mAChE, 61 residues (906 atoms) for Fas2, 6 sodium counterions, and 35 796 solvent water molecules (including the crystallographic water molecules; 107 388 atoms): a total of 116 579 atoms.

The whole system was equilibrated with velocity reassignment every 1 ps (500 steps) at 50 K, 100 K, 200 K and 298.15 K, for 20 ps (10 000 steps) each. Then it was equilibrated (without velocity reassignment) at 298.15 K for 1 ns (500 000 steps).

The equilibration and production parts of the simulation were performed on the Blue Horizon, an IBM Scalable POWERparallel (SP) supercomputer, at the San Diego Supercomputer Center. The production part was carried out over a period of 6 months (not continuous). The production jobs ran on 64 to 128 processors of the Blue Horizon, consuming about 75 processor-months of supercomputer time. Frames were collected at 1 ps intervals for the production length of 5 ns, giving 5×10^3 frames.

III.C.3 Proper radii of the passages

The extent of opening for every passage into the gorge was characterized using a single variable named the proper radius, as we have introduced previously for the gorge in the apo-mAChE MD [2, 32]. The proper radius was defined as the maximum radius of a spherical ligand that can go through the opening of interest from outside of the protein to reach the active site. This could be measured with an algorithm which finds the largest probe radius that generates the solvent-accessible surface with a continuous topology. Equivalently in practice, we detected whether the $O_{\epsilon 1}$ atom of Glu 202 contributes to a inflated solvent accessible surface that connects to the outside of the protein. The probe was considered capable of entry into the active site when the residues outside and those inside are topologically continuous. With several trials for each snapshot, we could narrow down the proper radius to a desired resolution.

Three possible passages leading into the active site were located: the gorge, the side door and the back door. While detecting for one potential opening, regions near the other two potential openings were blocked to avoid contamination. The gorge was blocked using a sphere centered at the average position of the atoms $C_{\delta 1}$ of Leu 76, C_{β} of Trp 286, and O_H of Tyr 72, with a radius of 110 pm. The blocking sphere of the back door was centered at the center of the 6-membered ring of Tyr 449, with a radius of 65 pm; that of the side door, at the C_{β} atom of Thr 75, with a radius of 91 pm. The proper radii for the side and back doors were only calculated if their values were larger than 140 pm at a resolution of 10 pm. A finer resolution (5 pm) was used for the gorge than for the doors, and no lower bound was imposed. Therefore, a discretized value of the gorge proper radius ρ means that the true value of the proper radius ρ^* satisfies $\rho - 2.5 \text{ pm} \leq \rho^* < \rho + 2.5 \text{ pm}$. For the doors, a value of proper radius ρ , when $\rho \geq 140 \text{ pm}$, the true value of the proper radius ρ^* satisfies $\rho \leq \rho^* < \rho + 10 \text{ pm}$ (Figure III.3).

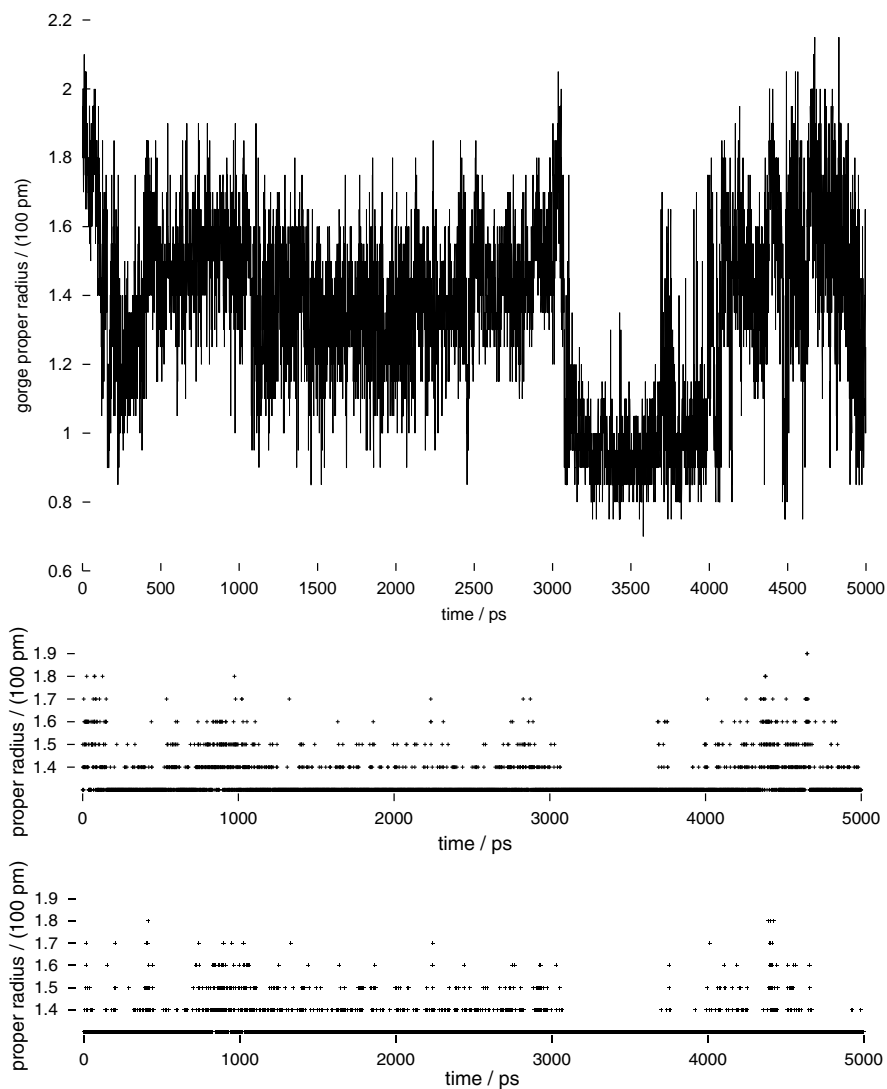


Figure III.3: Time series for the openings through the 5 ns Fas2-mAChE MD simulation. Top, gorge proper radius; Center, back door proper radius; Bottom, side door proper radius. For the latter two, points at the bottom row represent time frames with proper radius smaller than 140 pm.

III.C.4 Principal component analysis

The C_α coordinates of whole complex throughout the 5 ns trajectory (1 803 degrees of freedom: 540 C_α atoms in mAChE and 61 in Fas2) were admitted into the principal component analysis (PCA) [29, 30]: The covariance matrix was constructed and then diagonalized to give the diagonal matrix of eigenvalues and the transformation matrix containing columns that were the eigenvectors. Using the transformation matrix, the projection time series along each one of the principal component was calculated. For each one of these principal components, the maximal and the minimal projections were transformed back to Cartesian coordinates.

III.C.5 Porcupine plots

Porcupine plots [2] may be used to show the correlation between the movement of C_α atoms and any desired functionally important motion. In this case, the functionally important motions are the extent of opening of the gorge, the side door, and the back door.

The correlation coefficient between a proper radius $\rho(t)$ and the x degree of freedom for an C_α atom $x_i(t)$ was defined as

$$\frac{\langle (x_i(t) - \langle x_i \rangle_t) (\rho(t) - \langle \rho \rangle_t) \rangle_t}{\sqrt{\langle (x_i(t) - \langle x_i \rangle_t)^2 \rangle_t \langle (\rho(t) - \langle \rho \rangle_t)^2 \rangle_t}}. \quad (\text{III.1})$$

Similar expressions were obtained for $y_i(t)$ and $z_i(t)$ for the y and z coordinates. These three correlation coefficients made up a correlation vector for the C_α atom of each residue. The direction of the vector indicated where the residue was displaced when the proper radius became above average.

III.D Results

The first part of the analysis compares mAChE in the present 5 ns simulation and our previous 10 ns simulation [2]. The differences in structure and dynamics of mAChE are

investigated from rmsd plots, B factors, PCA, and average structures. The fluctuations in the width of the passages leading to the active site are examined and porcupine plots are used to pick out the motions of residues involved in their opening. In the second part of the analysis, the relative motion of the two proteins is assessed, and the nature of the interface region in the Fas2-mAChE complex is inspected by looking at the dominant residue contacts, particularly those that change or diverge from the crystal structure with time.

III.D.1 Stability of the trajectory and rmsd

The energy components, the temperature, and the volume were inspected and found to have reasonable stability throughout the 5 ns simulation (data not shown), ensuring that the system was at equilibrium. The rmsd of the protein structures from the crystal structure as a function of time for both heavy atoms and C_α atoms is in Figure III.4. The rmsd for the heavy atoms in the complex fluctuated but stayed around 330 pm, and for the C_α atoms, around 280 pm. This is in contrast to the lower respective values in apo-mAChE of 170 pm and 120 pm. Thus, the simulated Fas2-mAChE complex appears to deviate more than apo-mAChE from the corresponding crystal structure. The mAChE part of the structure has even larger rmsd values through the 5 ns, but the fluctuation thereof is smaller than that of the whole complex.

Comparing the average structure from the production run with the crystal structure indicates the changes that occurred during the equilibration phase. These changes were mainly in the termini and the segments that were flexible in the production run. The active site residues had also changed in its conformation during equilibration; this change is shown below in detail.

III.D.2 Flexibility from B factors

The isotropic temperature (B) factors provide a means of finding out which parts of the protein are behaving differently between apo-mAChE and Fas2-mAChE. B factors

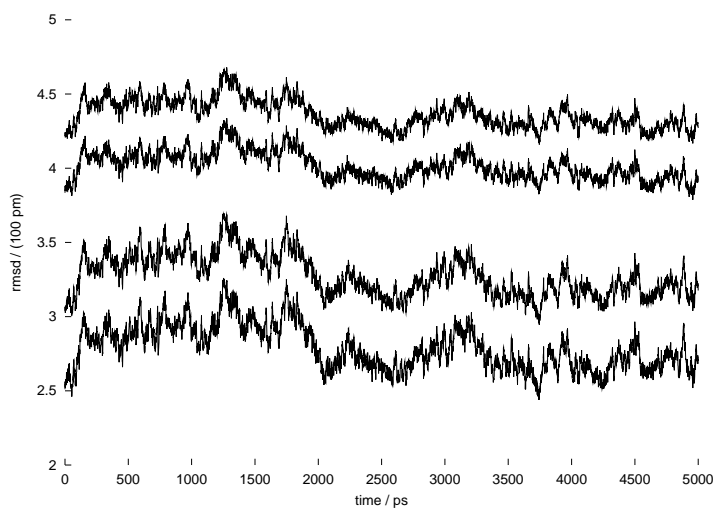


Figure III.4: Root mean square deviation (rmsd) through the 5 ns Fas2-mAChE MD trajectory, using the crystal structure of the complex as reference. The bottom pair of curves are for the whole complex, with each frame superimposed over the crystal structure of the whole complex (1MAH). The top pair of curves are for the mAChE part of the complex, with each frame superimposed over the mAChE part of crystal structure only. In each pair of curves, the top curve is the rmsd for the heavy atoms, and the bottom curve is the rmsd for the C_{α} atoms.

for our MD simulations were calculated from the mean square fluctuation (msf) [14] (Figure III.5).

As in the apo-mAChE simulation, there is a wide variation in flexibility for different residues. To compare apo-mAChE and the complex, the ratio of the B factors calculated in the complex MD trajectory over those from the apo-mAChE MD for each residue is calculated (Figure III.6); this information may be marked onto the protein in Figure III.7. The extent of positive deviation in complex ranges from blue (least) to red (most). Interestingly, deviations predominate around a number of residues and segments on the surface of the protein, namely, residues 46, 320, 462 and the segments 258–264 (the distal small Ω loop) and 430–435. Overall, the B factors seen in the complex MD are larger and again support the overall trend that mAChE is more flexible in the complex than in the apo-form in our simulations.

Comparing the B factors for the Fas2 calculated from this simulation and the previous unbound Fas2 MD simulation [61], we find that the flexibility in loops I (residues 4 to 16) and II (residues 23 to 38) that appeared in the unbound simulation has been suppressed compared to the flexibility in loop III (residues 42 to 51) and the two turn regions that encompass residues 16–20 and 54–57 near the Fas2 core.

III.D.3 Collective motion from principal component analysis

Principal component analysis is one means of displaying collective motion. The principal components with the largest eigenvalues represent the largest scale motions. The calculated eigenvalues decrease in magnitude quickly but smoothly: the 8th largest is less than 0.1 of the largest, and the 38th largest is less than 0.01 of the largest. The Cartesian-coordinate structures for the maximal and minimal projections of the principal components with the two largest eigenvalues (1.58 nm^2 and 0.87 nm^2) are shown in Figure III.8.

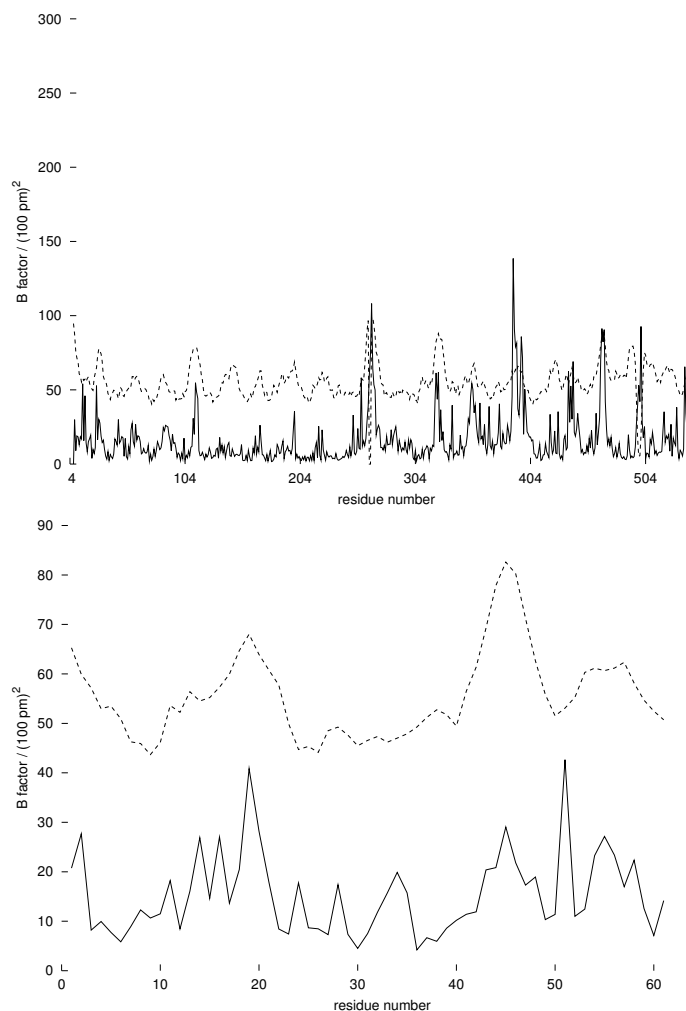


Figure III.5: Top, B factor for each residue in the mAChE part of the complex; bottom, that in the Fas2 part. Dashed line, B factor of the C_α atoms as reported in the crystal structure (1KU6); solid line, calculated for the whole residue from the msf in the 5 ns Fas2-mAChE MD trajectory.

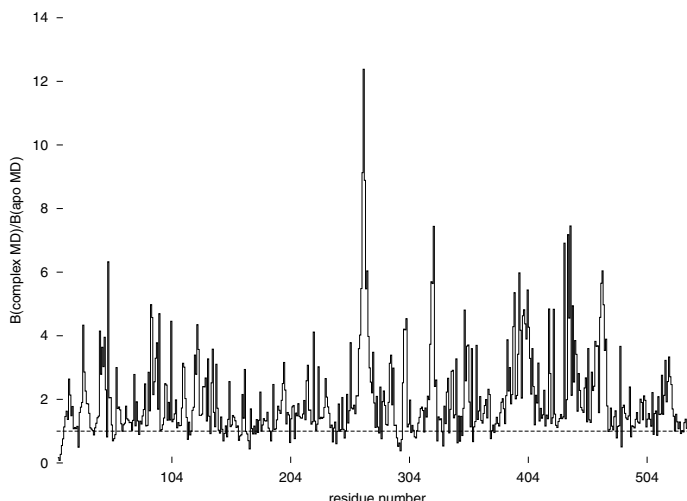


Figure III.6: Ratio of B factors for each residue in mAChE, calculated as that from Fas2-mAChE MD over that from the apo-mAChE MD. The dashed line marks 1.

III.D.4 Comparing the average structures of mAChE

For both the apo-form and the complex simulations, we produced the average structure of mAChE by superimposing the enzyme conformations onto that in the crystal structure and taking the mean of the atom positions. The resulting two average structures are displayed in Figure III.9. The distances between the C_{α} atoms, and the absolute values of the ϕ and ψ angle differences for every residue in each average structure were calculated (Figure III.10). When comparing these average structures, we have to keep in mind that many differences in the distances and angles might be linked to the differences in crystal packing and in the resolutions of the starting crystal structures.

While the overall agreement between the two structures is close, there are many places where they differ in small ways, and in a few loops the difference is quite substantial, such as residues 258 to 264 (the distal small Ω loop), 370 to 393, and 436 to 442, as well as the C -terminus. A greater variation is seen in the dihedral angles, but evidently many of these changes appear to cancel out and lead to little net movement in C_{α} position.

The active site arrangement was changed in the Fas2-bound complex, with critical

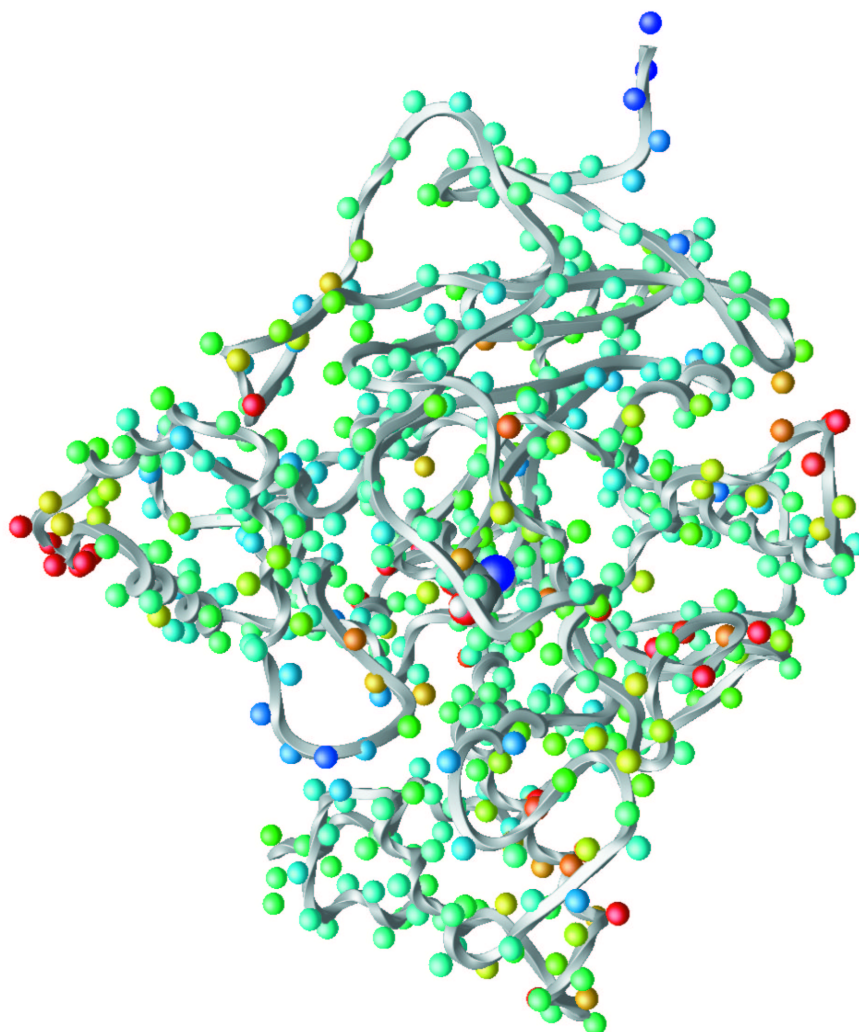


Figure III.7: Ratio of B factor for each residue in mAChE, calculated as that from Fas2-mAChE MD over that from the apo-mAChE MD, colored on the mAChE structure; each sphere represents one residue. The ratio decreases from red to blue. The active site Ser 203 is shown in the space-filling representation. Generated using OpenDX (IBM, White Plains, New York) with Chemistry Modules [60].

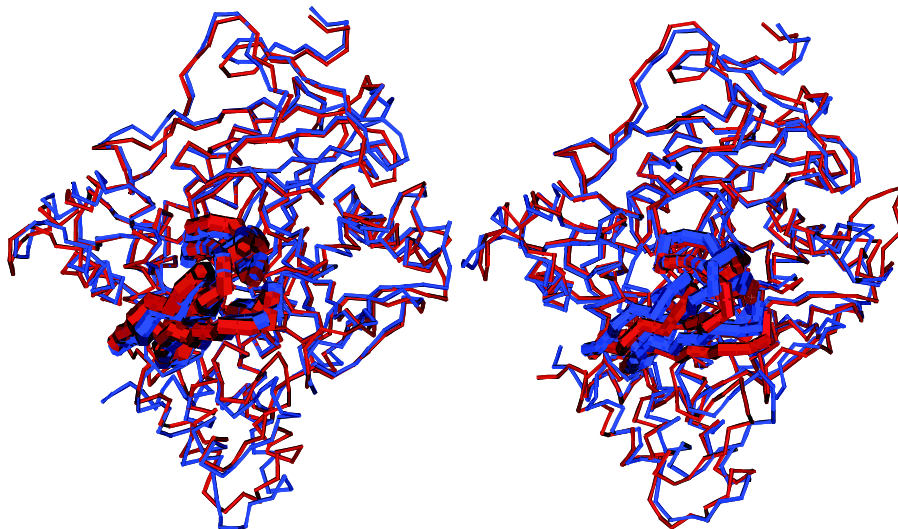


Figure III.8: Structures representing the extremal projections on the principal components with the largest eigenvalue, 1.58 nm^2 (left) and the second largest eigenvalue, 0.87 nm^2 (right). Red, maximal projection; blue, minimal projection. The thicker backbone is the Fas2 part of the structure. Generated using VMD [62].

implications for the function of mAChE. The change was seen by comparing the average structures from the apo-form and the complex trajectories (Figure III.11): In the apo-form average structure, the arrangement was conducive to proton transfer placing the imidazole ring of His 447 between the carboxyl group of Glu 334 and the hydroxyl group of Ser 203. Visual inspection of the complex trajectory and the average structure therefrom showed that by many dihedral angle changes in the backbone and side chains, the His 447 imidazole ring moved to a conformation where it is almost orthogonal to the route of proton transfer. In addition, the side chain carboxyl group of Glu 334 has moved away from the route. This disruptive change in conformation occurred in the 1 ns equilibration procedure before the 5 ns production run, and persisted through the 5 ns production trajectory.

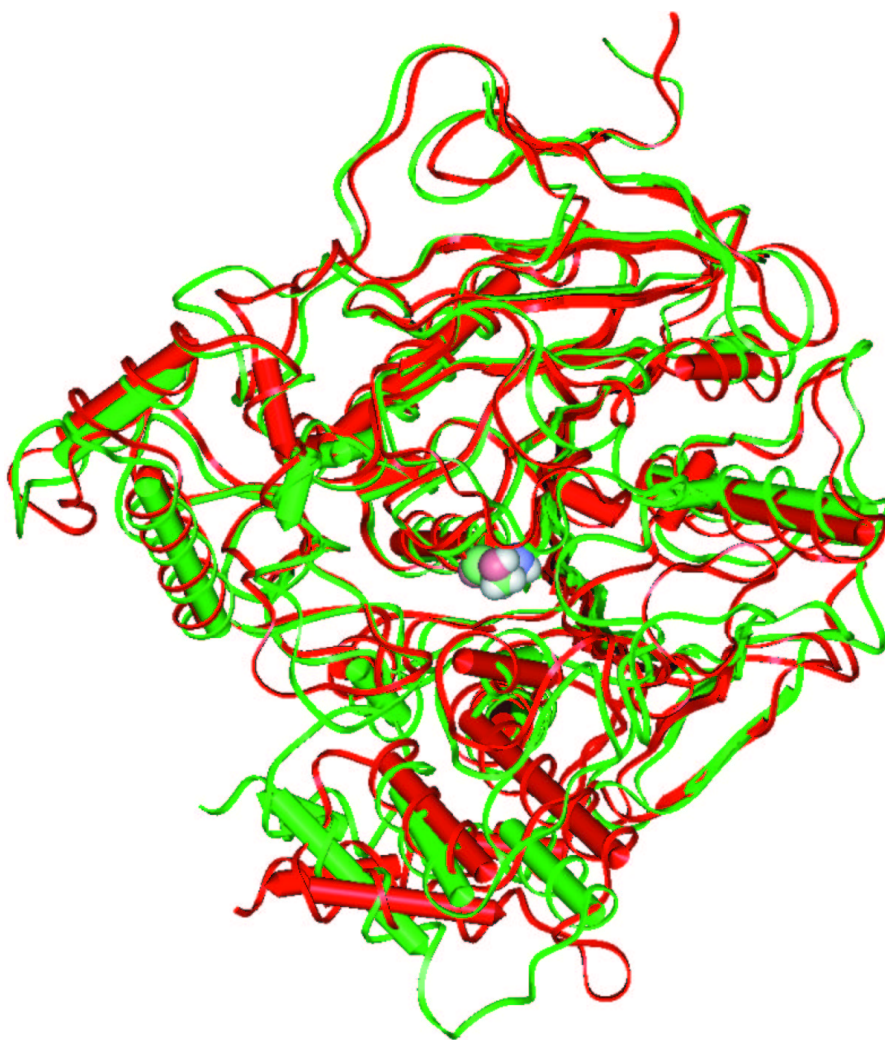


Figure III.9: Comparing the average structures from the 10 ns apo-mAChE (red) and from the 5 ns Fas2-mAChE (green) trajectories. The backbones are displayed in the ribbon representation, with the α -helices and β -sheets shown. Residue Ser203 from the average structure of the apo-mAChE trajectory is shown in the space-filling representation. Generated using *Insight II*.

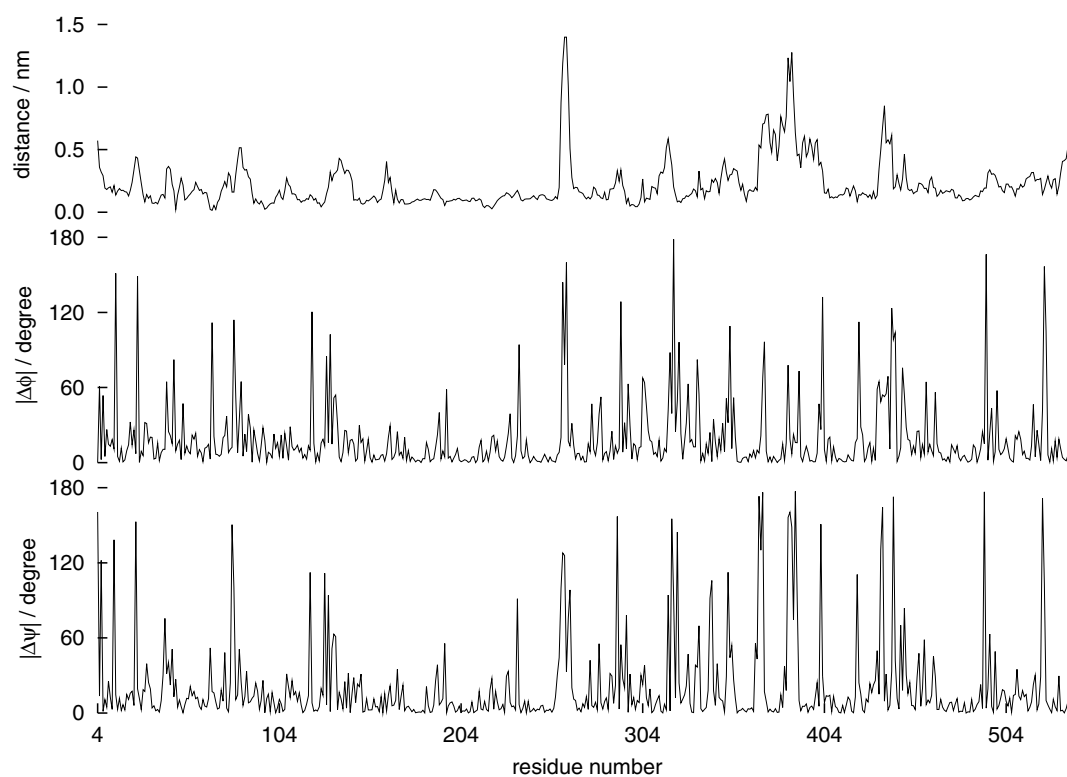


Figure III.10: Comparing the average structures from the 5 ns Fas2-mAChE and the 10 ns apo-mAChE trajectories. Top: the distances between the C α atoms of each residue in the two average structures. Center: the absolute values of the ϕ -angle differences. Bottom: the absolute values of the ψ -angle differences.

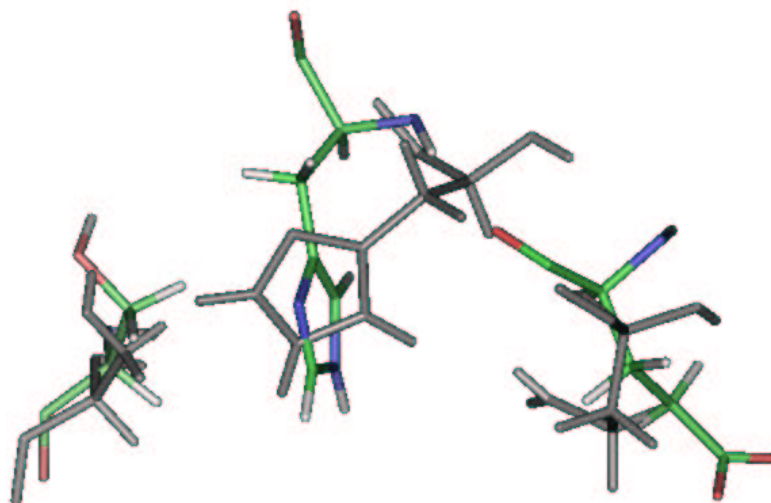


Figure III.11: Catalytic triad of mAChE. The average structures from both simulations are shown, after all-atom superimposition of the mAChE molecule. Gray, the apo-mAChE MD; colored, from the Fas2-mAChE MD. From left to right, the residues are Ser 203, His 447, and Glu 334. Generated using *Insight II*.

III.D.5 Opening of the passages

The one entrance into the active site that has been observed in all available crystal structures is the main active site gorge itself. The distribution for the gorge proper radius in the 5 ns Fas2-mAChE simulation is shown in Figure III.12; the time series thereof is in Figure III.3. As in the 10 ns apo-mAChE MD, we found two distinct local maxima in the probability distribution of the proper radius [32]. This affirms that there are indeed two states in mAChE gorge fluctuation: one narrower and one wider. In comparison, with Fas2 bound, the narrower state becomes more favored than in the apo-form simulation, and the distribution as a whole moves towards a smaller value for the gorge proper radius.

In addition, we produced the selective average structure for only the frames with an open gorge (proper radius greater than 127 pm) and that for only the frames with a closed gorge. The selective average structures for the open and closed version do not appear to be significantly different. This is also true for the selective structures of the

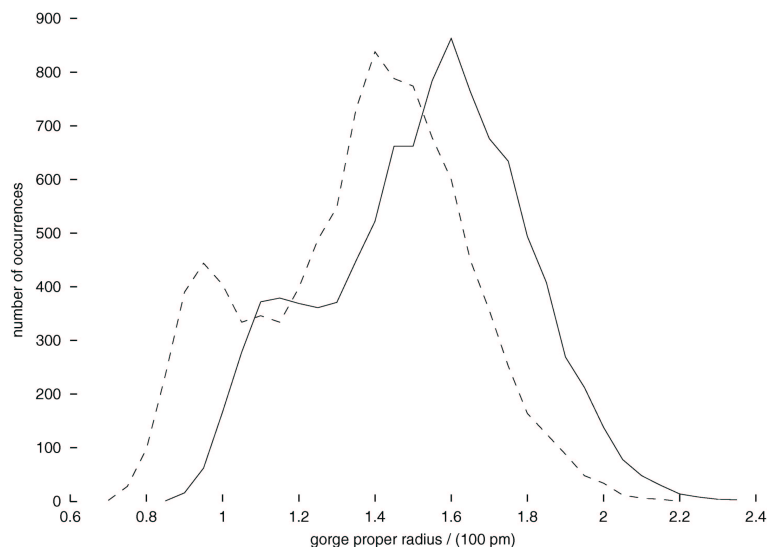


Figure III.12: Distribution of the gorge proper radius. Solid line, that in the 10 ns apo-mAChE trajectory; dashed line, twice that in the 5 ns Fas2-mAChE trajectory (so normalized for ease of comparison with the 10 ns data).

side door, and those for the back door. (For these two, an opening is defined as having a proper radius greater than 140 pm.) If we focus on the gorge, the distance between the C_{α} atoms of Tyr 124 and Phe 338 that straddle the gorge in the selective average structure with an open gorge is 1.288 nm; the distance in the structure with a closed gorge is 1.281 nm; the difference is only 7 pm. For in the apo-mAChE trajectory, the same distance measurement has 1.485 nm in the open gorge case, and 1.440 nm in the closed case; the difference is 45 pm and is comparable to the difference in gorge radius between the two states seen in Figure III.12.

A much larger and possibly functionally important difference was observed for the back and side doors. In the apo-form simulation, the back door was open to water molecules less than one hundredth (0.01) of the frames and the side door was never observed to be open. However, in the complex both side and back doors are observed to be open for a significant amount of simulation time. As shown in Figure III.3, 917 out of the 5 000 frames collected (0.18) have a back door opening event (proper radius

larger than 140 pm); 664 out of the 5 000 frames (0.13) have a side door opening event (defined likewise). There are 1 158 frames (0.23) with either of the alternative passages open, and 423 frames (0.08) with both open.

To probe the access to the active site by ligands or solvent molecules through the gorge when Fas2 is bound, we blocked the side and back doors, and measured the largest opening in the gorge region with Fas2 in place. The gorge is open to a spherical probe of radius 140 pm in 233 frames (0.05), while in only 9 frames is the gorge open for a spherical probe of radius 160 pm.

III.D.6 Motions of passages using porcupine plots

Porcupine plots are an alternative means of displaying concerted protein motion. In the present work, they are used to extract out protein motion correlated with the radius of each passage found into the gorge. Three porcupine plots, for the gorge, the side door, and the back door, are shown in Figure III.13. The coloring indicates the extent to which a residue's motion is correlated with the opening of the given passage, with red the most and blue the least.

Different parts of the protein are seen to be associated with each passage. Among the largest vectors in the side door porcupine plot is at residue 86, whose C_α atom is close to the side door region. Residues 445 and 446, in the back door region, have two of the largest vectors in the back door porcupine plot.

III.D.7 Movement and contacts of Fas2

The first issue addressed here is the extent of Fas2 motion relative to mAChE. The trajectory of the center of geometry of Fas2 (defined as the average position of the C_α atoms) relative to that of mAChE was calculated. It was found that this Fas2 trajectory is contained within a sphere of radius 250 pm. Thus it appears that the two proteins remain largely fixed with respect to each other for the duration of the simulation.

The second question is what residue contacts are made at the interface and whether

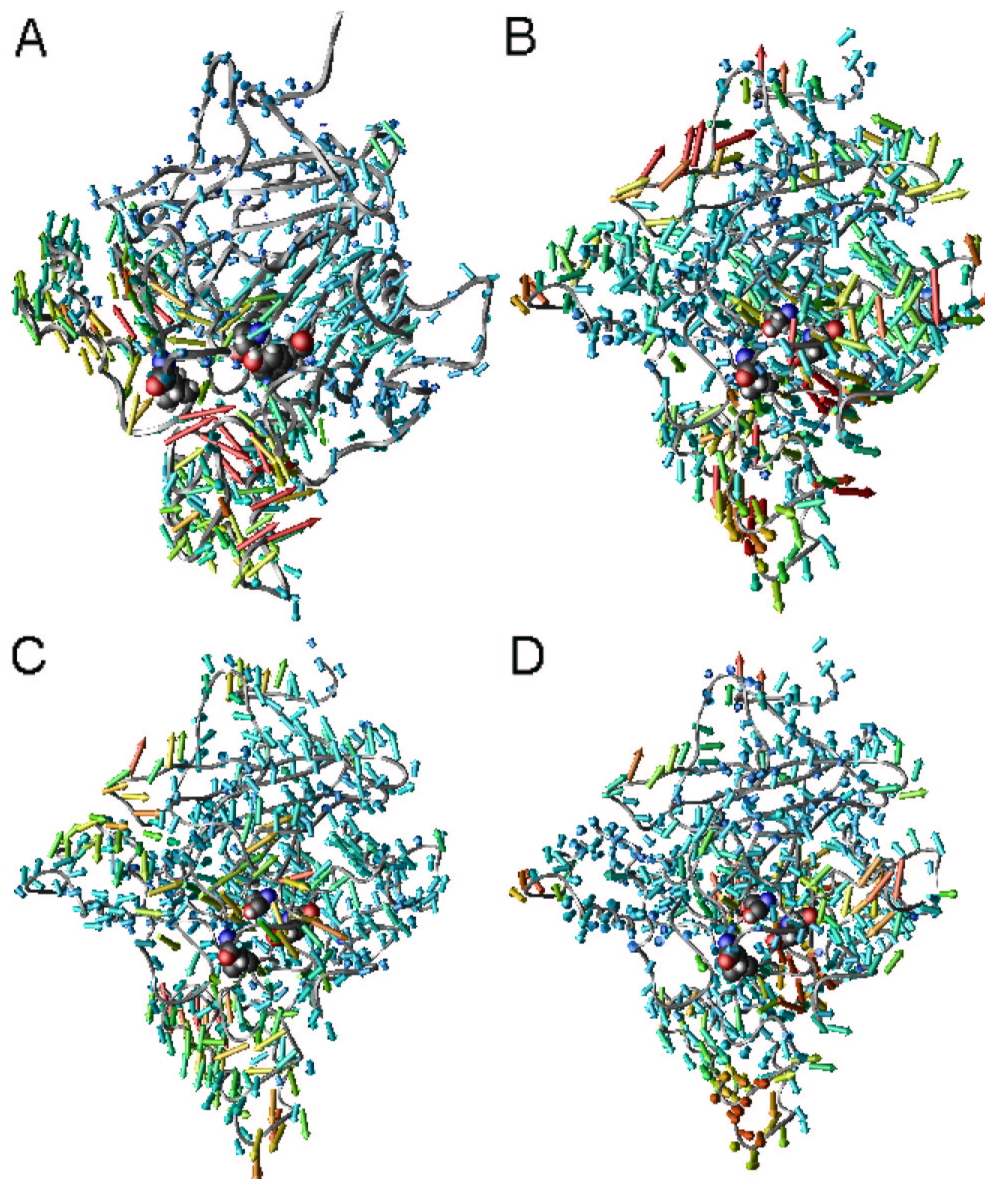


Figure III.13: Porcupine plots. A, for the gorge in the apo-mAChE trajectory; B, for the gorge in the Fas2-mAChE trajectory. In these two, the same coloring scheme is used. C, for the side door in the Fas2-mAChE trajectory; D, for the back door in the Fas2-mAChE trajectory. In each, three residues are shown in the space-filling model: Ser 203 (marking the bottom of the gorge and the active site), top; Tyr 449 (marking the back door), right; Leu 76 (marking the side door), bottom left. Generated using OpenDX with Chemistry Modules [60].

any of these change. To pick out interesting contact pairs at the Fas2-mAChE complex interface, we record any distance between a heavy atom in Fas2 and another in mAChE that is shorter than 500 pm for more than half of the 5×10^3 frames in the 5 ns trajectory. There are 599 contact pairs between heavy atoms in the interface. Eighty-three (83) of these are polar (between non-carbon heavy atoms) contact pairs; on the residue level, there are 39 interesting polar residue–residue contact pairs. For the 83 polar atom–atom pairs, we tallied the distributions of their distances through the 5 ns trajectory. If there is more than one maximum to a 50 pm resolution in a distribution, the residue can be considered more dynamic; otherwise, it is considered static, as the distance only fluctuates around one value. The details of these pairs are shown in Figure III.14 and in the Supporting Information of [3].

III.E Discussion

Fas2 may influence the function of mAChE in a variety of complementary ways: Fas2 may sterically obstruct the entrance of the mAChE gorge, allosterically change the conformation of parts of the enzyme, affect the fluctuation behaviors of the openings dynamically, or affect the efficiency of the catalysis at the active site, among other things. Hence our results will be discussed in light of these effects that may conceivably be adopted in natural design of Fas2.

III.E.1 Steric obstruction of the gorge entrance

As the eigenvalues from the PCA decrease rapidly in magnitude, the largest collective motions are represented in the few principal components with the largest eigenvalues. Looking at two of these components (Figure III.8), we do not see any collective movement that suggests Fas2 moving away significantly from the binding configuration where it sterically obstructs the gorge entrance. The Fas2 center of geometry movement relative to mAChE was also small; indeed, this motion can be contained by a sphere of radius 250 pm.

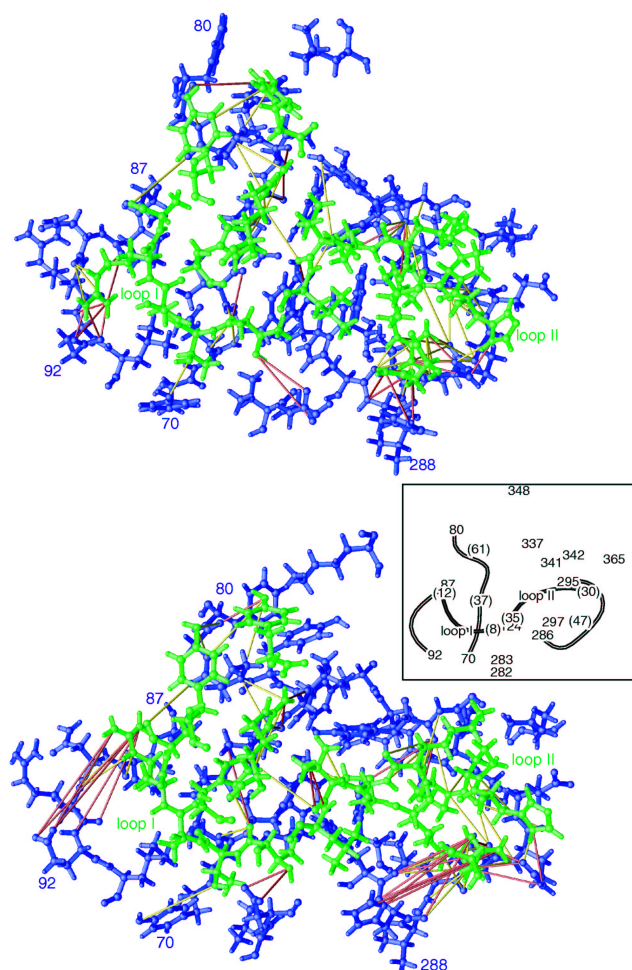


Figure III.14: Interface contact pairs. Top, structure of the residues participating in contact at the start of the 5 ns production trajectory (at 0 ns; that is, right after the 1 ns equilibration); bottom, that at 5 ns. The residues shown are those participating in interfacial interactions more often than not during the 5 ns, both polar and nonpolar. Residues belonging to Fas2 are shown in green; those of mAChE, blue. The yellow bars represent polar interactions with only one maximum in the distance distribution (static); the red bars represent polar interactions with more than one maximum (dynamic). Generated using OpenDX with Chemistry Modules [60]. Inset, the backbone of the relevant segments in Fas2 (gray) and in mAChE (white), with key residues labeled (Fas2 in parentheses); generated using Molscrip [56].

With Fas2 bound, the active site is rarely accessible through the gorge to allow entry of a spherical ligand with radius 160 pm (much smaller than the acetylcholine profile). Since it is nearly impossible for a ligand this size to move through the gorge, access to the active site is only likely through the alternative passages; in this simulation, we observed a large increase in their opening likelihood compared to the apo-mAChE trajectory.

III.E.2 Interactions at the interface

The polar interface contact pairs are listed in the Supporting Information of [3]. The participating mAChE residues mostly fall into two groups: the Ω loop group (residues 69 to 96) and the residues near the peripheral site (roughly from Asp 283 to Ser 293, and Tyr 341). On the Fas2 side, the participating residues are mostly from loop I or II; only Asn 47 is from loop III, and Tyr 61 is at the *C*-terminus of Fas2. It is notable that nearly all Fas2 residues at this interface participate in polar interactions (Figure III.14).

The contact regions of Fas2, namely loops I and II, have higher or comparable flexibility compared to loop III in the previous unbound Fas2 simulation [61]. When bound to mAChE, they are surpassed in flexibility (measured by the *B* factors) by the non-contacting loop III.

Except for the few contacts made by the Fas2 core region, we do see most of the contacts reported in the crystal structure [28], and when we do not see the exact interaction, usually a neighboring residue has a contact pair. In short, loops I and II of Fas2 have contacts with the mAChE Ω loop, while only loop II is in charge of interacting with the peripheral site. The flexibility of these contact loops is decreased relative to other parts of Fas2 upon binding.

III.E.3 Allostery: mAChE conformation and flexibility changed

As we embark in comparing the apo-mAChE and the complex trajectories, there is a caveat we have to point out first: With nanosecond-scale simulations, the trajectories do

not sample adequately all conformations available for a protein of the size of mAChE to explore. Some of the differences observed may be real and indicative of changes in protein functions under different circumstances; others may simply be trajectory-specific idiosyncracies that are imprudent to generalize.

Most residues in mAChE exhibited larger B factors in the Fas2-mAChE simulation than in the apo-mAChE one (Figure III.6). In particular, the distal small Ω loop from Pro 258 to Gly 264 had an extremely large increase in B factor as compared to that in the apo-mAChE simulation. Notably, this loop could not be resolved in the Fas2-mAChE complex crystal structures (1MAH and 1KU6) [28] because of its high flexibility, while in the tetrameric mAChE structure (1MAA) [57], where it participates in the crystalline tetramer interface and has stabilizing interactions, it was resolved in two of the monomers. The flexibility of this loop, as observed in the simulation, may be the reason for its low resolution in the complex structure.

Our previous apo-mAChE simulation [2] used the mAChE molecule from the Fas2-mAChE complex structure at 0.32 nm (3.2 Å) resolution (1MAA); the present Fas2-mAChE simulation used a Fas2-mAChE structure at 0.25 nm (2.5 Å) resolution, a resolution improvement that would be expected to generate lower B factors for the Fas2-mAChE simulation. Yet, we observed a higher flexibility in the complex trajectory than in the apo-mAChE trajectory.

By visual inspection, the most impressive differences between the mAChE structures from the apo-mAChE and Fas2-mAChE complex trajectories are in the positions and flexibilities of the distal small Ω loop from Pro 258 to Gly 264 (at the leftmost of Figure III.9) and the remote segment around residue 380 (at the bottommost of the same figure). Despite being far from the Fas2 binding site, the distal small Ω loop seems to acquire a different average position and become more flexible (as seen in the B factors) upon Fas2 binding. This is in stark contrast with fluorescence spectroscopy results where the fluorophore attached at residue 262 of this distal loop indicated little alteration in flexibility [63]. To reconcile this discrepancy, we recall that the distal loop was built in artificially in the two MD simulations. Thus it may not be justified to compare

the difference in flexibility in MD of this loop, considering its local lack of resolution in the crystal structure compounded with the ambiguity introduced by the artificial model-building process.

III.E.4 Dynamical inhibition of gorge opening

Contrary to previous expectations [28, 57], the observed change in the fluctuation (as indicated by the B factors) and conformation of the Fas2-bound mAChE Ω loop are only moderate and not outstanding in view of other parts of the molecule. Evidences both from simulations and from fluorescence spectroscopy experiments [55] indicate that, though mAChE and *Candida rugosa* lipase are related in their α/β hydrolase fold, the former does not seem to have its open and closed states characterized by the well-defined hinge motion of the Ω loop as the latter [64].

Considering that the two peaks in the probability distribution function of the gorge proper radius were separated by about 50 pm in the apo-mAChE trajectory [32], it is not surprising that the difference between the Tyr 124–Phe 338 C_α distance is 45 pm. On the other hand, the smaller 7 pm difference in the complex trajectory manifests that the bottleneck region of the gorge is no longer coupled to the Tyr 124–Phe 338 distance upon Fas2 binding, and implies significant change in the mechanism of the gorge opening behavior.

The binding of Fas2 indeed favors a narrower gorge size, as shown in Figure III.12. Not only does the whole distribution shift towards a smaller value of the proper radius, but the narrower of the two distinct states becomes more likely to occur in the complexed trajectory. Comparing the porcupine plot for the gorge with that from the apo-mAChE MD [2, 65], we find that the concert of motions near the Fas2 interface seems to be repressed in the Fas2-mAChE trajectory. Such effect of dynamical inhibition [26] is impressive, though the mechanism by which Fas2 imposes this effect is still not clear to us.

III.E.5 Changes in the alternative passages to the active site

In contrast to the apo-mAChE trajectory where only one hundredth (0.01) of all the frames collected gave an open back door [2], we have an increase in the likelihood of opening to 0.18 when Fas2 is bound. In addition, the side door also has a 0.13 chance of being open in the complex trajectory (Figure III.3). In the porcupine plots, most concerted motions show up around the respective alternative passages (the side door and the back door). These increases in the number and likelihood of alternative openings, as previously suggested, may indeed be responsible for some of the residual, or even enhanced, substrate catalysis in Fas2-bound AChE [28, 50–52].

In a previous MD simulation of mAChE complexed with the active site ligand huperzine A [66], opening of the side door is observed more frequently than in the apo-form simulation [27]. In another simulation, where the *T. californica* AChE dimer is complexed with the active site inhibitor tacrine [25], side door opening is also observed. It is in this context that we report here the significant increase of side door opening events induced by an inhibitor that does not bind at the AChE active site. This implies that alternative passage opening events may be promoted by either active site or peripheral site binding.

III.E.6 Changes in the conformation of the active site

Comparing the average structures (Figure III.11) from the apo-mAChE and Fas2-mAChE trajectories, we notice dramatic differences in the mAChE catalytic triad: Upon Fas2 binding, the functional groups in Glu 334 and His 447 have moved out of the strategic positions conducive to proton transfer that are observed in the apo-mAChE MD and the crystal structure. Such movements are achieved through movements of the backbone and several dihedral angle changes in the side chains, and do not appear to be trivial. Specifically, in the average structure from the Fas2-mAChE MD, the Glu 334 carboxylic group now points away from the neighboring His 447 in the complex MD, and the His 447 imidazole ring is now at an angle from its position in the apo-mAChE

MD, out of alignment for proton transfer.

Crystallography of *T. californica* AChE complexed with the organophosphorus inhibitor VX showed a movement of the active site histidine [67]. Monoclonal antibodies that bind to the peripheral site has been reported to allosterically affect the orientation of Trp 86 near the active site [68]. In addition, kinetic data have suggested that Fas2 inhibits AChE by disrupting the conformation of the active site, thus slowing down the proton transfer steps [49]. Our observation here is consistent with such a mechanism. However, as the Fas2 binding site does not neighbor the active site, the sequence of mechanical processes through which Fas2 exerts its influence is not immediately ostensible. Even though more rigorous procedures (such as the use of particle-mesh Ewald for the long-range electrostatics) were used here than the early MD work on *T. californica* AChE where active site disruption was relieved by addition of absent counterions in the gorge [69], the changes in the active site presently observed can only be considered suggestive at this stage.

III.F Conclusions

In the Fas2-mAChE complex, Fas2 binds to the mAChE Ω loop and peripheral site with excellent surface complementarity using many polar and hydrophobic interactions from loops I and II [28]. Our 5 ns simulation of this complex shows that Fas2 binding dynamically disfavors the opening of the mAChE active site gorge but increases the likelihood for back door and side door opening, a feature that may contribute to the residual (and occasionally enhanced) catalytic activity of the Fas2-bound enzyme observed in solution. As in the apo-mAChE simulation, the fluctuating behavior of the mAChE gorge in the Fas2-bound complex continues to present complexity, though selective averaging suggests a change in the location of the bottleneck region. Fas2 binding also increases the flexibility of two surface segments remote to the binding site, and, most impressively, disrupts the catalytic triad arrangement of the mAChE active site. In sum, we have observed steric, allosteric, and dynamic effects likely to represent the components

of the mechanism through which Fas2 influences the function of mAChE.

III.G Acknowledgments

We thank Dr. Tjerk P. Straatsma for providing and supporting the NWChem software, and Prof. Palmer W. Taylor, Dr. Zoran Radić, and Ms. Jianxin Shi for assistance and advice. Gratitude is expressed to Accelrys, San Diego, for providing us with the *Insight II* software, and to Dragon Farms, Toronto, for permission to use the photograph of *D. angusticeps* feeding. K. T. is a fellow of La Jolla Interfaces in Science training program, supported by Burroughs Wellcome Fund. This project was supported in part by Howard Hughes Medical Institute, W. M. Keck Foundation, San Diego Supercomputer Center, National Biomedical Computation Resource, National Science Foundation, and National Institutes of Health.

This chapter contains the same material as an article that appeared in the *Journal of American Chemical Society* [3], of which I am the primary author.

IV

Finite element simulations of acetylcholine diffusion in neuromuscular junctions

What I cannot create, I do not understand. [70]

IV.A Abstract

A robust infrastructure for solving time-dependent diffusion using the finite element package FETk has been developed to simulate synaptic transmission in a neuromuscular junction with realistic postsynaptic folds. Simplified rectilinear synapse models serve as benchmarks in initial numerical studies of how variations in geometry and kinetics relate to endplate currents associated with fast-twitch, slow-twitch, and dystrophic muscles. The flexibility and scalability of FETk affords increasingly realistic and complex models that can be formed in concert with expanding experimental understanding from electron microscopy. Ultimately, such models may provide useful insight on the functional implications of controlled changes in processes, suggesting therapies for neuromuscular

This chapter is reproduced with permission from the manuscript Tai, K.; Bond, S. D.; MacMillan, H. R.; Baker, N. A.; Holst, M. J.; McCammon, J. A. submitted to *Biophys. J.* **2002**.

diseases.

IV.B Introduction

The neuromuscular junction (NMJ) is the point of communication between neurons and muscle fiber in the orchestration of muscle contraction. This study encompasses the release of neurotransmitter acetylcholine (ACh), its hydrolysis with acetylcholinesterase (AChE) clusters, and its reactive presence near acetylcholine receptor (AChR) molecules. Past computational modeling of synaptic transmission on this scale has involved either differential equations governing continuum reaction-diffusion [71, 72] or particle methods such as Brownian dynamics and Monte Carlo [73, 74]. Here, we present an improved finite element infrastructure to solve continuum reaction-diffusion using FETk [75], an efficient platform for adaptive multiscale modeling. These efforts highlight the flexibility of finite elements to evolve with improved understandings of reaction kinetics. Now, with the capacity to represent realistic NMJs, comparative studies can be conducted with the guidance of coordinated experimental data. Ultimately, this could provide insight on the functional implications of NMJ variations associated with neuromuscular diseases, such as muscular dystrophy and myasthenia gravis.

IV.C The neuromuscular junction

A typical NMJ features a smooth presynaptic neuron membrane and a folded postsynaptic muscle surface of crests and troughs. When an action potential reaches the end of the nerve, it results in a localized influx of calcium ions that, in turn, causes vesicles to fuse to the neuron membrane and release ACh. In our model, vesicles are treated as having just opened and we do not yet account for subsequent relaxation of the neuron membrane. Eventually, this effect may be incorporated into FETk, along with spatial control of vesicle placement according to the varying presence of calcium ions.

ACh diffuses across the synaptic cleft and potentially binds to acetylcholine recep-

tors, ion channels embedded in the postsynaptic folds. AChR ion channels are multi-protein membrane-spanning complexes found at packing densities of up to $10\,000\,\mu\text{m}^{-2}$ at the crests of the postsynaptic folds. In the absence of ACh, an AChR channel is impermeable to ion flow. However, once two ACh molecules bind to it, AChR opens and ions flow through the muscle cell membrane: sodium inward, potassium outward. This ion flow defines an endplate current (EPC) across the muscle membrane that, when strong enough, induces contraction. Roughly 1 ms after activation, ACh molecules are released back into solution and AChR ion channels close.

ACh molecules remain in the cleft until they are hydrolyzed by AChE, the biomolecular “off-switch” for synaptic transmission. AChE is present as clusters of three tetramers suspended by collagen stalks bound to the muscle membrane at varying density (from $600\,\mu\text{m}^{-2}$ to $2500\,\mu\text{m}^{-2}$) throughout the postsynaptic folds. As an extremely fast enzyme capable of destroying ACh molecules at rates approaching theoretical limits, AChE provides a very efficient mechanism to terminate synaptic transmission for subsequent signaling [1, 9].

Experimental data are available on the ultrastructure and activity of NMJs of different muscle types to guide the initial development of mathematical models [76–81]. Ultrastructural differences between the NMJs in vertebrate fast (twitch or extensor digitorum longus) and slow (tonic or soleus) muscles have been observed [10, 82–84]. Also, geometric and reactive deviations in mouse NMJs due to muscular dystrophy have been documented [11, 85–87]. Local measurements of miniature endplate current (mEPC) are used to infer the functional implications of such structural differences on an NMJ’s efficiency. Having established our simulation infrastructure, we can begin to recreate the effects of the various parameters of different muscle types *in silico*. It is evident that more experimental data coordinated with simulations are needed to bring increasingly realistic models to maturity.

IV.D Mathematical setting

IV.D.1 Continuum formulation

In a continuum model, the concentration of ACh, $u(\mathbf{x}, t)$, is assumed to satisfy the time-dependent diffusion equation in the synaptic cleft, Ω , with appropriate conditions on its boundary, $\partial\Omega$. Formally, the concentration varies from its initial state, $u(\mathbf{x}, 0)$, according to

$$\frac{du(\mathbf{x}, t)}{dt} - \nabla \cdot D \nabla u(\mathbf{x}, t) = 0 \quad \text{in } \Omega, \quad (\text{IV.1})$$

$$\hat{\mathbf{n}}(\mathbf{x}) \cdot D \nabla u(\mathbf{x}, t) = \begin{cases} -k'_{\text{act}} u(\mathbf{x}, t) & \text{on } \partial\Omega_{\text{act}} \\ 0 & \text{on } \partial\Omega - \partial\Omega_{\text{act}} \end{cases}, \quad (\text{IV.2})$$

where $D = 4.0 \times 10^{-4} \mu\text{m}^2 \cdot \mu\text{s}^{-1}$ is the diffusion coefficient, $\hat{\mathbf{n}}(\mathbf{x})$ is the outward unit normal, and $\partial\Omega_{\text{act}} \subset \partial\Omega$ denotes the cumulative reactive surface of AChE with specific reactivity k_{act} [71]. Note that Equation IV.2 states a zero-flux condition on all boundaries except the surfaces representing AChE clusters, $\partial\Omega_{\text{act}}$, for which a linear reaction scheme yielding a Robin boundary condition is now assumed. Estimation of the specific reactivity, k_{act} , is described in each example. Attempts to lift this linear assumption on AChE binding and use more involved boundary conditions will be the focus of future research.

IV.D.2 Discrete formulation

We use the backward Euler algorithm to define a method of lines and reduce Equations IV.1 and IV.2 to the following elliptic problem at time t_n , knowing the previous concentration, $u(\mathbf{x}, t_{n-1})$:

$$-\nabla \cdot D \nabla u(\mathbf{x}, t_n) + \frac{u(\mathbf{x}, t_n) - u(\mathbf{x}, t_{n-1})}{t_n - t_{n-1}} = 0 \quad \text{in } \Omega, \quad (\text{IV.3})$$

$$\hat{\mathbf{n}}(\mathbf{x}) \cdot D \nabla u = \begin{cases} -k'_{\text{act}} u & \text{on } \partial\Omega_{\text{act}} \\ 0 & \text{on } \partial\Omega - \partial\Omega_{\text{act}} \end{cases}. \quad (\text{IV.4})$$

It is convenient to write $u_n := u(\mathbf{x}, t_n)$ and define

$$b(\mathbf{x}, u_n, u_{n-1}) := \frac{u(\mathbf{x}, t_n) - u(\mathbf{x}, t_{n-1})}{t_n - t_{n-1}}. \quad (\text{IV.5})$$

Integrating by parts, we obtain the weak form of Equation IV.4,

$$\begin{aligned} \int_{\Omega} D\nabla u_n \cdot \nabla v \, d\mathbf{x} - \int_{\partial\Omega} v D\nabla u_n \cdot \hat{\mathbf{n}} \, dS + \int_{\Omega} b(\mathbf{x}, u_n, u_{n-1}) v \, d\mathbf{x} &= 0, \\ \forall v \in V, \end{aligned} \quad (\text{IV.6})$$

where V is the test space [21, 75]. Enforcing boundary condition on $\partial\Omega$, the weak form becomes

$$\begin{aligned} \int_{\Omega} D\nabla u_n \cdot \nabla v \, d\mathbf{x} + k'_{\text{act}} \int_{\partial\Omega_{\text{act}}} u_n v \, dS + \int_{\Omega} b(\mathbf{x}, u_n, u_{n-1}) v \, d\mathbf{x} &= 0, \\ \forall v \in V. \end{aligned} \quad (\text{IV.7})$$

For a discrete solution to Equation IV.7, a finite element space $V^h = \text{span}\{\phi_1, \dots, \phi_N\} \subset V$ is used. The Galerkin approximation

$$u_n^h = \sum_{i=1}^N u_i \phi_i \in V^h \quad (\text{IV.8})$$

satisfies the discrete weak form

$$\begin{aligned} \int_{\Omega} D\nabla u_n^h \cdot \nabla \phi_i \, d\mathbf{x} + k'_{\text{act}} \int_{\partial\Omega_{\text{act}}} u_n^h \phi_i \, dS + \int_{\Omega} b(\mathbf{x}, u_n^h, u_{n-1}^h) \phi_i \, d\mathbf{x} &= 0, \\ \forall \phi_i \in \{\phi_1, \dots, \phi_N\}, \end{aligned} \quad (\text{IV.9})$$

knowing the discrete solution from the previous timestep, $u_{n-1}^h = \sum_{i=1}^N u_i^{\circ} \phi_i \in V^h$. To formulate Equation IV.9 into a matrix equation, we write the terms

$$\int_{\Omega} D\nabla u_n^h \cdot \nabla \phi_i \, d\mathbf{x} = \sum_{i=1}^N \left[u_i \int_{\Omega} D\nabla \phi_i \cdot \nabla \phi_j \, d\mathbf{x} \right], \quad (\text{IV.10})$$

$$k'_{\text{act}} \int_{\partial\Omega_{\text{act}}} u_n^h \phi_i \, dS = k'_{\text{act}} \sum_{i=1}^N \left[u_i \int_{\partial\Omega_{\text{act}}} \phi_i \phi_j \, dS \right], \quad (\text{IV.11})$$

$$\int_{\Omega} b(\mathbf{x}, u_n^h, u_{n-1}^h) \phi_i \, d\mathbf{x} = \left(\frac{1}{t_n - t_{n-1}} \right) \sum_{i=1}^N \left[(u_i - u_i^{\circ}) \int_{\Omega} \phi_i \phi_j \, d\mathbf{x} \right]. \quad (\text{IV.12})$$

It follows that

$$\mathbf{A}\mathbf{u} + \frac{1}{\Delta t} \mathbf{M}(\mathbf{u} - \mathbf{u}^{\circ}) + k'_{\text{act}} \mathbf{F}\mathbf{u} = 0, \quad (\text{IV.13})$$

where the stiffness matrix $\mathbf{A} = [A_{ij}] = \left[\int_{\Omega} D\nabla \phi_i \cdot \nabla \phi_j \, d\mathbf{x} \right]$, the mass matrix $\mathbf{M} = [M_{ij}] = \left[\int_{\Omega} \phi_i \phi_j \, d\mathbf{x} \right]$, $\mathbf{F} = [F_{ij}] = \left[\int_{\partial\Omega_{\text{act}}} \phi_i \phi_j \, dS \right]$, and the solution vectors $\mathbf{u} = [u_i]$, $\mathbf{u}^{\circ} = [u_i^{\circ}]$.

IV.D.3 Numerical solution and visualization

Several methods of lines to solve Equations IV.1 and IV.2 have been built in the context of FETk [75], a finite element package written in “clean object-oriented” C language. Details on the resulting linear systems at each timestep, using the backward Euler method of lines described above. At each timestep, the conjugate gradient method is used with termination chosen such that time-truncation error is less than 10^{-10} . Given a surface triangulation of an NMJ boundary with realistic folds, a robust and flexible mesh generation package, NETGEN [88], develops a structured volume mesh that has been interfaced with FETk (Figures IV.1 and IV.8). A structured mesh fine enough to sufficiently describe the constraining surface geometry is used in the examples that follow, and refining this mesh (i.e., halving edge length) has no appreciable effect. Similarly, the timestep has been chosen to adequately resolve a postsynaptic response curve; e.g., the range $10^{-1} \mu\text{s}$ to $10^1 \mu\text{s}$ was studied to ensure that the simulation is not overly sensitive to the chosen timestep, $1 \mu\text{s}$. Computing 1 000 timesteps for a system of approximately 33 000 vertices (such as the rectilinear synapse model) takes less than 1 hour on an Intel (Santa Clara, California) Xeon 1.80 GHz personal computer. The classical duo of backward Euler method of lines combined with conjugate gradient is nearly optimal for ordinary diffusion. Moreover, FETk memory usage scales linearly with the number of vertices. The FETk output formats are readable using MATLAB (MathWorks, Natick, Massachusetts), GMV (Los Alamos National Laboratory, New Mexico) and OpenDX (International Business Machines, White Plains, New York).

IV.D.4 Postsynaptic detection and AChR binding

Equations IV.1 and IV.2 quantify the presence of ACh in the NMJ, but relating this to experimentally observable mEPC involves estimating not only the density of AChR, but also the stochastic nature of its binding and retention. By defining the postsynaptic detection level, $L(t)$, as the weighted surface integration

$$L(t) := \int_{\partial\Omega} \gamma_R(\mathbf{x}) u(\mathbf{x}, t) \, dS, \quad (\text{IV.14})$$

where $\gamma_R(\mathbf{x})$ is AChR density, we only observe general timescale trends of observed mEPC, such as rise time and signal duration.

Toward more accurate estimations of mEPC, we account for ACh-AChR binding in the model to properly estimate the time course of open AChR ion channels. This entails appealing to the equilibrium mechanism $2\text{ACh} + \text{AChR}_{\text{closed}} \rightleftharpoons (\text{ACh})_2(\text{AChR}_{\text{open}})$, and assuming that AChR is saturated with ACh. For the equilibrium constant, we have $K = \gamma_R \theta / [u^2 \gamma_R (1 - \theta)]$, where θ is the fraction of open AChR channels. This implies $\theta = Ku^2 / (1 + Ku^2)$, leading to a new measure of postsynaptic response

$$\Lambda(t) := \int_{\partial\Omega} \gamma_R(\mathbf{x}) \frac{Ku(\mathbf{x}, t)^2}{1 + Ku(\mathbf{x}, t)^2} dS. \quad (\text{IV.15})$$

According to [89], $K = 3.6 \times 10^2 \text{ mM}^{-2} = 1.0 \times 10^{-9} \mu\text{m}^6$. While $\Lambda(t)$ is an improvement, it still does not consider the effect of ACh retention when bound to AChR. To do this is to alter the zero-flux condition on the postsynaptic folds with an integral that records accumulations of ACh bound to the ion channels. This sophistication will soon be incorporated into our modeling framework for realistic NMJs so that proper benchmarking with coordinated mEPC observations can be conducted. For brevity, we do not present plots of $\Lambda(t)$ in all the examples that follow, as they cannot yet be compared with experimental data.

IV.E Neuromuscular junction models

IV.E.1 Rectilinear benchmarking

As a first point of contact with existing literature, we have created a simplified rectilinear NMJ model similar to that in [71]. We introduce this model before presenting preliminary studies on the functional implications of variations in this geometry. All simulations are in micrometers and microseconds, with concentrations in particles per volume and densities in particles per area. Rectilinear models have also been studied with MCell [73, 74].

Neuromuscular geometry and initial conditions

In [71] a simplified rectilinear model of an NMJ is considered with 3 identical secondary clefts and the following measurements (Figure IV.1): primary cleft length = $2.0 \mu\text{m}$; primary cleft width = secondary cleft width = $0.05 \mu\text{m}$; separation between secondary clefts = $0.5 \mu\text{m}$; secondary cleft depth = $0.8 \mu\text{m}$.

We include a vesicle as a sphere of radius $0.024 \mu\text{m}$ fused to the middle of the presynaptic membrane. Its center is placed $0.016 \mu\text{m}$ above this membrane, leaving a circular area of radius $0.018 \mu\text{m}$ as the pore opening. The initial ACh concentration is only nonzero inside the vesicles, where it is $300 \text{ mM} = 1.8 \times 10^8 \mu\text{m}^{-3}$ [5, 71, 90, 91]. With the vesicle size stated above, this translates to 6.06×10^3 ACh molecules present. We recognize that this is a rather important yet simplistic aspect of our simulation, and sensitivity to the initial distribution of ACh will be included in future studies.

AChE clusters are treated as three-dimensional “holes” in the NMJ mesh with boundary condition Equation IV.2. The previous finite element simulation [71] uses an AChE cluster density of about $240 \mu\text{m}^{-2}$. By comparison, in [73], an active site density of $1800 \mu\text{m}^{-2}$ in the primary cleft (equivalent to a cluster density of about $150 \mu\text{m}^{-2}$) and twice that in the secondary cleft is used. The length of the collagen stalk that connects AChE from the synaptic basal lamina is on the scale of $0.05 \mu\text{m}$, depending on the species [92]. As done previously, we place AChE midway between the presynaptic and postsynaptic membranes in our rectilinear models. We have chosen to use cubic boxes with $0.02 \mu\text{m}$ sides spaced $0.1 \mu\text{m}$ apart in a square array spanning the primary and secondary clefts to afford a cluster density of $100 \mu\text{m}^{-2}$.

Reactivity of AChE

The reactivity of an AChE cluster in our model is relative to the surface area used to represent it. Following [71] we determine k'_{act} by conducting several separate but simple simulations. We represent an AChE cluster as a single cube with $0.02 \mu\text{m}$ edges, and place it at the center of a cube with $0.30 \mu\text{m}$ edges. The boundary condition for $\partial\Omega_{\text{act}}$ in Equation IV.2 is used on the surface of the interior cube, the AChE cluster. On the

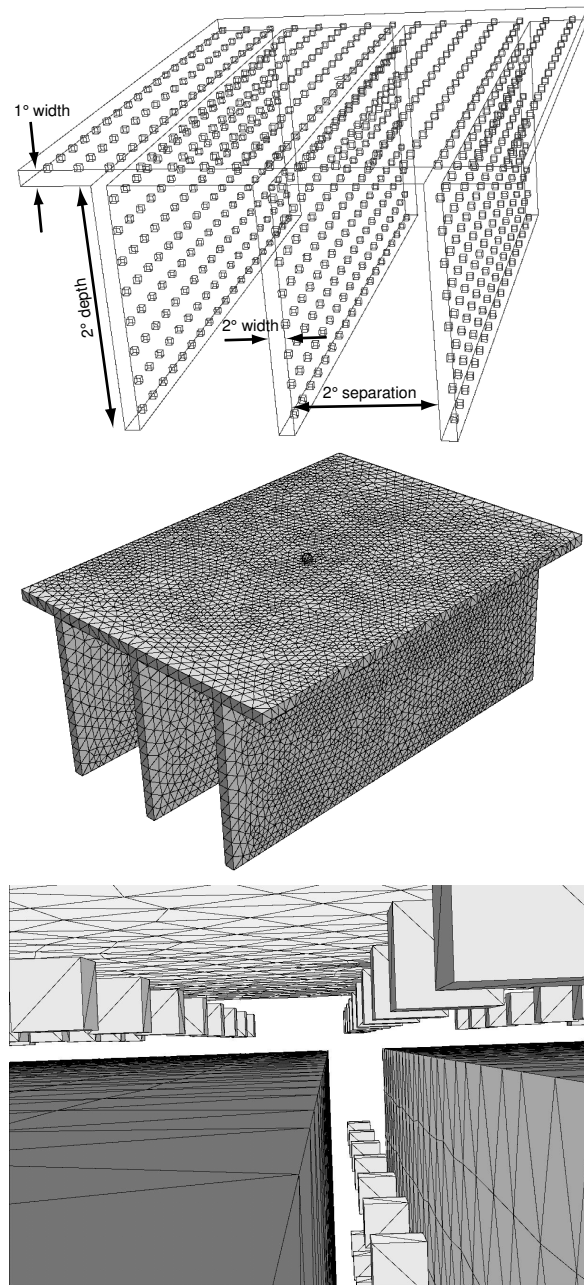


Figure IV.1: Three views (edges, outside, inside) of the finite element mesh for the rectangular model of the neuromuscular junction, with three secondary clefts and a spherical vesicle fused to the presynaptic membrane. The cubes represent acetylcholinesterase. 1°, primary cleft; 2°, secondary cleft.

exterior cube boundary $\partial\Omega - \partial\Omega_{\text{act}}$, the concentration of ACh is held at a different constant value for each “trial” simulation. The “current” of ACh consumed by AChE is defined to be

$$J := \int_{\partial\Omega_{\text{act}}} \hat{\mathbf{n}} \cdot D\nabla u \, dS. \quad (\text{IV.16})$$

Naturally, J must also equal the flux of ACh into the domain due to imposing constant ACh concentration on the outer boundary. Assuming a nonsaturated steady state and the catalytic scheme $E + S \rightarrow E + P$, the flux into the domain is estimated in linear proportion to the concentraion of ACh maintained on the boundary [71, 93]. Writing this proportionality constant as k , we set

$$ku|_{\partial\Omega - \partial\Omega_{\text{act}}} = k'_{\text{act}} \int_{\partial\Omega_{\text{act}}} u \, dS \quad (\text{IV.17})$$

and consider simulations with different sustained steady state levels of ACh on the outer boundary. Since $k = k_{\text{cat}}/K_{\text{M}} \approx 3 \times 10^9 \text{ M}^{-1} \cdot \text{min}^{-1} = 5 \times 10^{-6} \mu\text{m}^3 \cdot \mu\text{s}^{-1}$ has been determined by experiment [52], enforcing Equation IV.17 for each steady-state leads to an estimation of k'_{act} . FETk with the backward Euler timestepper is used to compute steady state ACh diffusion between the concentric cubes, with validation from an explicit steady-state solver. Sampling the range $1.00 \times 10^5 \mu\text{m}^{-3}$ to $1.00 \times 10^7 \mu\text{m}^{-3}$ (that is, 0.166 mM to 16.6 mM) as the imposed ACh concentration on the outer boundary, we find $k'_{\text{act}} = 2.0 \times 10^{-3} \mu\text{m} \cdot \mu\text{s}^{-1}$. This is slightly larger than the value used previously [71], due to the fact that we are using here a different area for the active site of AChE. With the enzymatic activity of AChE approximated, Equations IV.1 and IV.2 can now be solved for the rectilinear NMJ.

Solution and postsynaptic detection

The time course of ACh diffusion in the rectilinear NMJ model has been solved using the backward Euler and FETk (as outlined above) with timesteps of $1 \mu\text{s}$. Figure IV.2 shows the total number of ACh molecules over $400 \mu\text{s}$; the same decay has been shown in the solid curve in Figure 3 of [71].

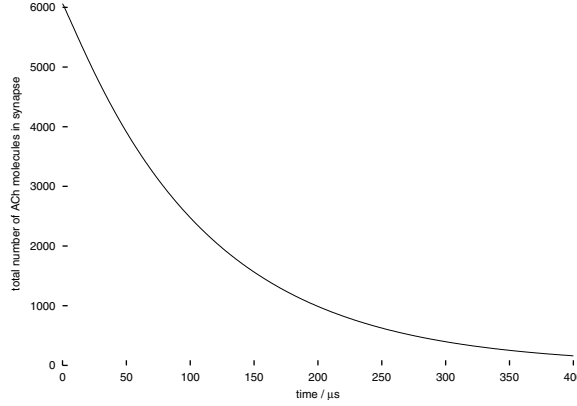


Figure IV.2: Total number of ACh molecules in the rectilinear NMJ model decreases over time.

Determining the postsynaptic detection level entails defining AChR density. MCell models typically use a graduated receptor density function γ_R [73, 74]. From the crest to $0.2 \mu\text{m}$ to $0.3 \mu\text{m}$ into the fold, γ_R ranges from $7\,000 \mu\text{m}^{-2}$ to $10\,000 \mu\text{m}^{-2}$. It is $2\,000 \mu\text{m}^{-2}$ to $3\,000 \mu\text{m}^{-2}$ another $0.2 \mu\text{m}$ to $0.3 \mu\text{m}$ from the crests, below which density falls off dramatically. Here we use a piecewise constant density of $\gamma_R(\mathbf{x}) = 8\,500 \mu\text{m}^{-2}$ from the crests down $0.25 \mu\text{m}$ into the secondary clefts, $\gamma_R(\mathbf{x}) = 2\,500 \mu\text{m}^{-2}$ an additional $0.25 \mu\text{m}$ into the secondary clefts, and then zero down to the troughs. The resulting postsynaptic detection level $L(t)$ is shown in Figure IV.3. The “rise time” (duration from the release of the vesicle to the peak) is about $20 \mu\text{s}$, much shorter than that of mEPC. However, since we do not yet consider ACh binding of AChR, this is reasonable. Moreover, it is comparable to the previous observation [71].

IV.E.2 Variations in muscle type

Fast-twitch and slow-twitch neuromuscular junctions

Simple rectilinear NMJ models for fast-twitch and slow-twitch muscle have been built according to the primitive dimensions listed in Table IV.1. Each model contains one vesicle, three identical secondary clefts, and the AChR distribution stated above. Also,

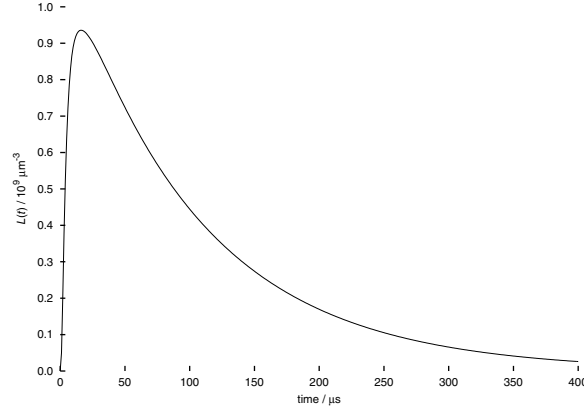


Figure IV.3: The postsynaptic detection level $L(t)$ in the rectilinear NMJ model.

	normal		dystrophic
	fast	slow	fast
primary cleft width / μm	0.10	0.10	0.10
secondary cleft depth / μm	1.00	0.75	0.50
secondary cleft separation / μm	0.25	0.50	0.75
secondary cleft width / μm	0.10	0.20	0.10

Table IV.1: Geometric dimensions for the rectilinear models of different muscle types [10, 83, 86].

as before, AChE clusters are $0.02 \mu\text{m}$ edged cubes raised $0.025 \mu\text{m}$ above the postsynaptic membrane with density $100 \mu\text{m}^{-2}$.

In Figure IV.4, the rise time of $L(t)$ for the fast-twitch NMJ model is $45 \mu\text{s}$, and a peak value of $4.25 \times 10^8 \mu\text{m}^3$ is obtained. In contrast, the slow-twitch geometry leads to a more gradual response, reaching the peak value $3.12 \times 10^8 \mu\text{m}^3$ in $43 \mu\text{s}$. The “decay time” (duration from vesicle release until the decay reaches half of the peak $L(t)$) for the fast-twitch muscle is $213 \mu\text{s}$, significantly shorter than that displayed in the slow-twitch geometry, $270 \mu\text{s}$.

In Figure IV.5, $\Lambda(t)$ is shown for the slow- and fast-twitch NMJ models. The peak-amplitudes are delayed and decay is accelerated in comparison to $L(t)$. As expected, the more rapid decay of fast-twitch muscle signal is preserved. There are miniature

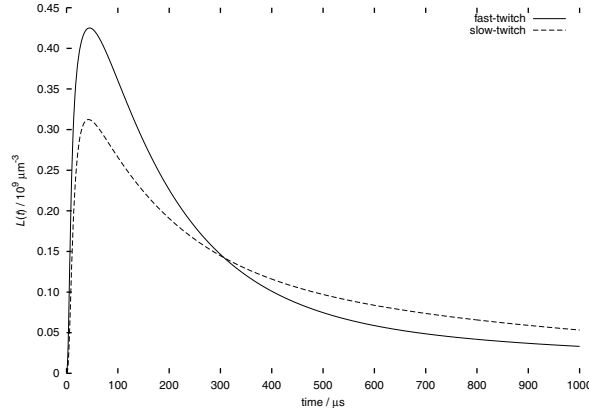


Figure IV.4: $L(t)$ for NMJ models of fast-twitch and slow-twitch muscles.

endplate potential (mEPP as opposed to mEPC) data on fast- and slow-twitch muscle in mouse [83]. Signal decay according to this data is several times longer, but the parallels between that geometry and our simulation are incomplete, essentially because the respective efforts, in being twenty years apart, are uncoordinated.

Dystrophic neuromuscular junctions

Some dystrophic muscle displays improperly developed NMJs in terms of ultrastructure [94], but again specific data are limited. For the rectilinear dystrophic NMJ model described in Table IV.1, the rise time, decay time, and amplitude of $L(t)$ are all slightly lower than normal (Figure IV.6). Of course, this simply states the obvious: such muscle does not function as efficiently! Models may not contribute in fundamental ways to muscular dystrophy until they can encompass the actual development of NMJ architecture during generation.

Reduced AChE density

As could be said for the distribution of AChR, aberrations in the presence of AChE can have functional implications. For the slow-twitch muscle NMJ, lowering AChE density to $50 \mu\text{m}^{-2}$ leads to a slightly longer rise time, $46 \mu\text{s}$, with a lower peak level

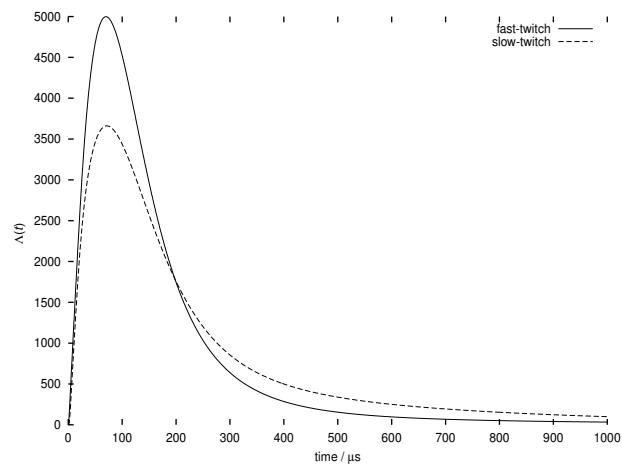


Figure IV.5: $\Lambda(t)$ for NMJ models of fast-twitch and slow-twitch muscles.

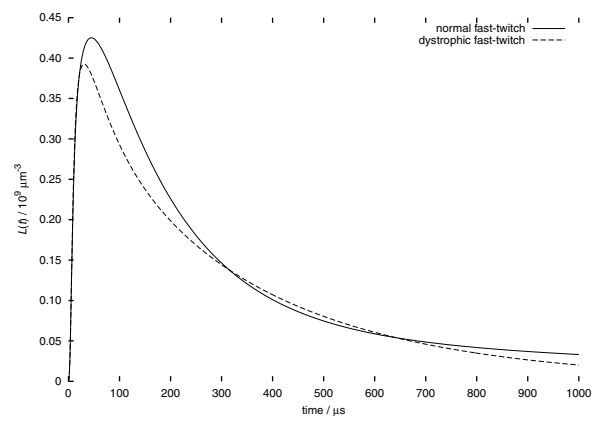


Figure IV.6: Normal versus dystrophic fast-twitch muscle.

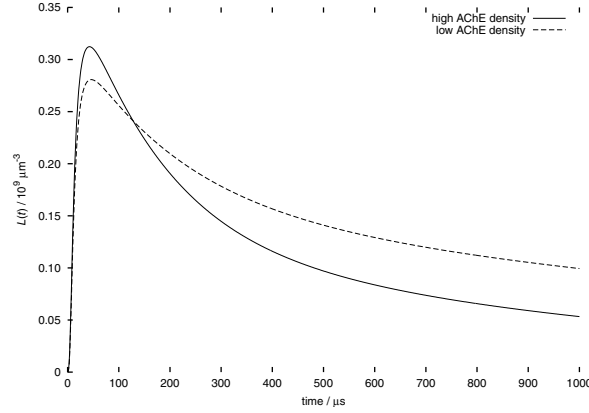


Figure IV.7: Comparing $L(t)$ for different AChE densities. High density: $100 \mu\text{m}^{-2}$; low density: $50 \mu\text{m}^{-2}$.

of $2.81 \mu\text{m}^3$ (Figure IV.7). The decay time is about twice as long, at $505 \mu\text{s}$. Specific experimental information on variations in AChE density among different muscle types is limited. As such, this example merely serves to illustrate that an abnormal density can have an appreciable effect on the efficiency of synaptic transmission across an NMJ.

IV.E.3 Realistic neuromuscular junction model

Finally, we demonstrate the capacity of FETk to model ACh transmission within a realistic NMJ geometry drawn from electron microscopy. Given this realism, our infrastructure is poised to accompany experiments.

Mesh geometry and initial condition

We are grateful to have received a realistic 3-dimensional surface-mesh model of an NMJ from Stiles and coworkers, formed from morphing a 2-dimensional electron micrograph [73, 74]. The resulting NETGEN volume mesh (Figure IV.8) includes the vesicle, while realizing AChE clusters requires the special attention described below. In total, there are 175 609 vertices and 771 408 simplices in the volume mesh. Edges range from $2.45 \times 10^{-3} \mu\text{m}$ to $1.05 \times 10^{-1} \mu\text{m}$ in length, simplex volume ranges from $1.87 \times 10^{-7} \mu\text{m}^3$

to $2.70 \times 10^{-4} \mu\text{m}^3$, and the worst (largest) edge ratio in any simplex is 14.4.

The vesicle is a triangulated sphere of radius $0.024 \mu\text{m}$ placed roughly in the center of the presynaptic membrane. The pore opening is a single triangle, with area $0.00054 \mu\text{m}^2$, at the locus of vesicle attachment. Initially, the ACh concentration is zero everywhere but inside the vesicle, where it is $300 \text{ mM} = 1.8 \times 10^8 \mu\text{m}^{-3}$. This translates to approximately 6.9×10^3 ACh molecules present at the beginning of simulation.

AChE clusters and reactivity

Placing AChE holes into the tetrahedral mesh is a nontrivial process that needs streamlining before “high-throughput” studies can be conducted. Currently, using the APBS [95] and FETk infrastructure, we repeatedly refine, down to a surface area threshold of $0.0024 \mu\text{m}^2$, the simplices that contain the positions of AChE monomers specified by Stiles and coworkers. The tetrahedral simplices containing the AChE positions are “removed” by marking adjacent faces of neighboring simplices as boundary. The resultant mesh has 55 589 tetrahedral AChE clusters, distributed as shown in Figure IV.9. The average surface area is $0.0017 \mu\text{m}^2$, representative of 59 072 AChE molecules. This average cluster surface area must be accounted for when estimating the specific reactivity k'_{act} . Since Equation IV.17 scales linearly with surface area of the cluster, the k'_{act} estimated in the previous section can be adjusted according to the smaller average surface area in the realistic model (by a factor of about 1.4). This simplification leads to $k'_{\text{act}} = 2.753 \times 10^{-3} \mu\text{m} \cdot \mu\text{s}^{-1}$.

AChR density and postsynaptic detection level

We use approximately the same AChR density criterion as the above rectilinear models. Figure IV.10 shows the postsynaptic detection level $L(t)$ for the more realistic NMJ model. The rise time is $10 \mu\text{s}$, about half as long as that in the previous rectilinear NMJ model, but comparison at this stage is somewhat unfounded.

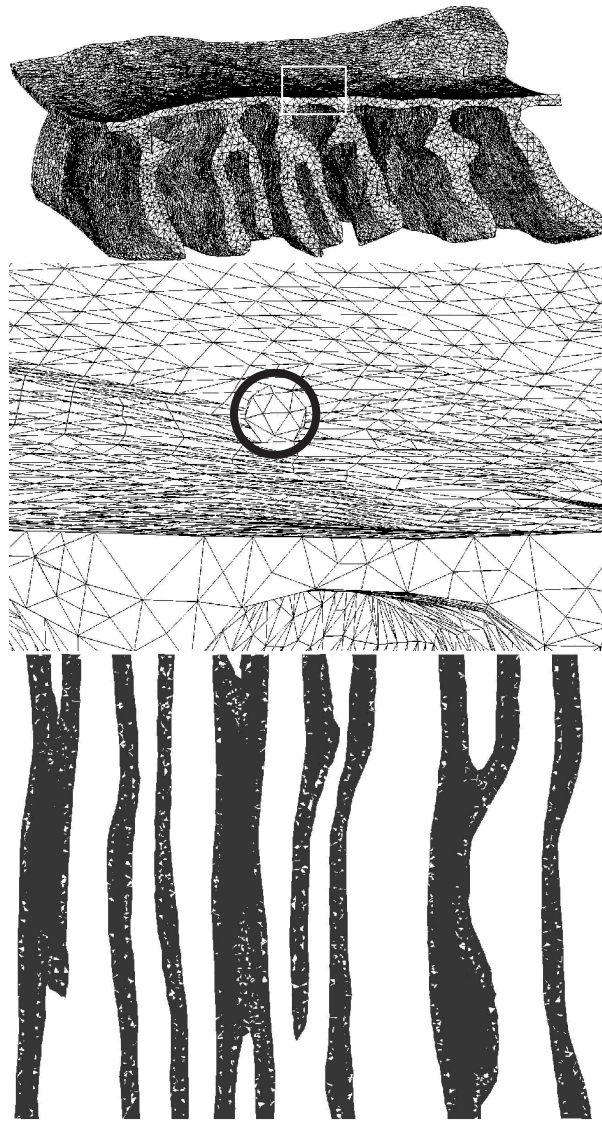


Figure IV.8: Three views of the realistic mesh: overview, enlarged box containing the vesicle on the presynaptic membrane, a cross-section of the secondary cleft (shaded). The AChE “holes” are unshaded. The height of the clefts from crest to trough is approximately $1\ \mu\text{m}$.

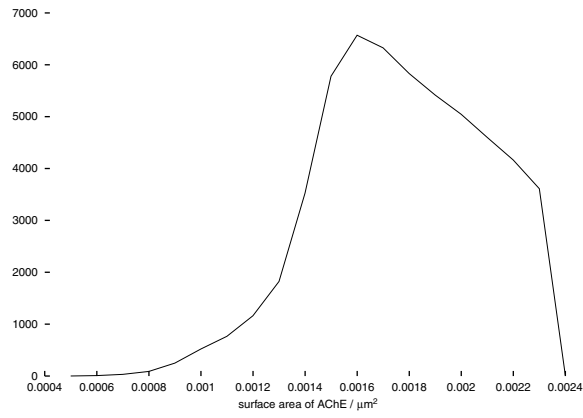


Figure IV.9: Surface area distribution of the AChE holes in the realistic mesh.

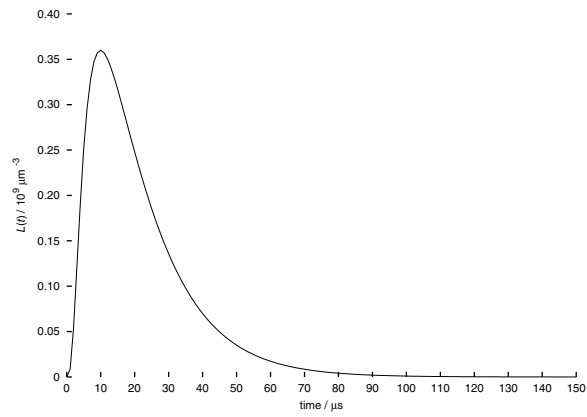


Figure IV.10: The postsynaptic detection level $L(t)$ over 150 μs in the realistic NMJ model.

IV.F Discussion and conclusions

We have shown that simple rectilinear models are capable of capturing electrophysiological trends observed in NMJs from different muscle types. Comparing decay time in the slow- and fast-twitch muscles reveals a discrepancy in behavior. Also, a model suggests that dystrophic muscle has a muted postsynaptic response. However, it is likely that NMJ malformation is less a cause than an effect in the pathology of dystrophy. As our primary contribution, we have created a finite element infrastructure capable of dealing with a realistic mesh based on electron microscopy data. This motivates future partnerships with coordinated experimental investigations on the relationship between muscle function and NMJ architecture. Currently, data that correlate geometry and kinetics with muscle function are, when available, scattered and incomplete for our intent and purpose.

Our effort to make physiologically relevant connections is an advancement from previous continuum models [71]. The finite element infrastructure we have unveiled will evolve on two fronts. First, with improved understanding of reaction kinetics, simulations will be more directly related to observable mEPC and mEPP. Second, increasing availability of ultrastructural data from electron tomography will offer the capacity for extensive comparative studies [96, 97]. Only then can parameter space, including NMJ geometry, vesicle placement, receptor binding, and reactivity, be comprehensively explored to better understand neuromuscular diseases that affect NMJ processes.

IV.G Acknowledgments

Our thanks go to Dr Burak Aksoylu, Prof. Mark H. Ellisman, Dr Jason Smart, Dr Jason Ka-Chun Suen, and Prof. Palmer W. Taylor for useful discussions. We are grateful to Prof. Tom Bartol and Prof. Joel Stiles for providing the realistic NMJ surface mesh. K. T. is a La Jolla Interfaces in Science fellow, supported partly by the Burroughs Wellcome Fund. This project is supported in part by the Howard Hughes Medical Institute, W. M. Keck Foundation, San Diego Supercomputer Center, National Biomedical Computation

Resource, National Science Foundation, and National Institutes of Health.

This chapter contains the same material as a manuscript submitted to the *Biophysical Journal*, of which I am the primary author.

Bibliography

- [1] Shen, T.; Tai, K.; Henchman, R.; McCammon, J. A. *Acc. Chem. Res.* **2002**, *35*, 332–340.
- [2] Tai, K.; Shen, T.; Börjesson, U.; Philippopoulos, M.; McCammon, J. A. *Biophys. J.* **2001**, *81*, 715–724.
- [3] Tai, K.; Shen, T.; Henchman, R. H.; Bourne, Y.; Marchot, P.; McCammon, J. A. *J. Am. Chem. Soc.* **2002**, *124*, 6153–6161.
- [4] Kandel, E. R.; Schwartz, J. H.; Jessell, T. M. *Principles of Neural Science*; Appleton and Lange: Norwalk, Connecticut, 1991.
- [5] Zimmermann, H. *Synaptic Transmission: Cellular and Molecular Basis*; Thieme: Stuttgart, 1993.
- [6] Shepherd, G. M. *Neurobiology*; Oxford University Press: Oxford, 1994.
- [7] Grutzendler, J.; Morris, J. C. *Drugs* **2001**, *61*, 41–52.
- [8] Wittbrodt, E. T. *Arch. Intern. Med.* **1997**, *157*, 399–408.
- [9] Taylor, P. Anticholinesterase agents. In *The Pharmacological Basis of Therapeutics*; Hardman, J. G.; Limbird, L. E.; Molinoff, P. B.; Ruddon, R. W.; Gilman, A. G., Eds.; McGraw-Hill: New York, 1996.
- [10] Ellisman, M. H.; Rash, J. E.; Staehelin, L. A.; Porter, K. R. *J. Cell. Biol.* **1976**, *68*, 752–774.
- [11] Ellisman, M. H. *Brain Res.* **1981**, *214*, 261–273.
- [12] Cornell, W. D.; Cieplak, P.; Bayly, C. I.; Gould, I. R.; Merz, Jr., K. M.; Ferguson, D. M.; Spellmeyer, D. C.; Fox, T.; Caldwell, J. W.; Kollman, P. A. *J. Am. Chem. Soc.* **1995**, *117*, 5179–5197.
- [13] Berendsen, H. J. C.; Grigera, J. R.; Straatsma, T. P. *J. Phys. Chem.* **1987**, *91*, 6269–6271.

- [14] McCammon, J. A.; Harvey, S. C. *Dynamics of Proteins and Nucleic Acids*; Cambridge University Press: Cambridge, 1987.
- [15] Allen, M. P.; Tildesley, D. J. *Computer Simulation of Liquids*; Oxford University Press: Oxford, 1987.
- [16] Becker, O. M.; MacKerell, Jr., A. D.; Roux, B.; Watanabe, M. *Computational Biochemistry and Biophysics*; Marcel Dekker: New York, 2001.
- [17] Ryckaert, J.-P.; Ciccotti, G.; Berendsen, H. J. C. *J. Comput. Phys.* **1977**, *23*, 327–341.
- [18] van Gunsteren, W. F.; Berendsen, H. J. C. *Mol. Phys.* **1977**, *34*, 1311.
- [19] Darden, T.; York, D.; Pedersen, L. *J. Chem. Phys.* **1993**, *98*, 10089–10092.
- [20] Straatsma, T. P.; Philippopoulos, M.; McCammon, J. A. *Comp. Phys. Commun.* **2000**, *128*, 377–385.
- [21] Braess, D. *Finite Elements*; Cambridge University Press: Cambridge, 1997.
- [22] Calvino, I. *Se una notte d'inverno un viaggiatore*; Einaudi: Torino, 1979.
- [23] Brooks, III, C. L.; Karplus, M.; Pettitt, B. M. *Proteins: A Theoretical Perspective of Dynamics, Structure, and Thermodynamics*; Wiley-Interscience: New York, 1988.
- [24] Gilson, M. K.; Straatsma, T. P.; McCammon, J. A.; Ripoll, D. R.; Faerman, C. H.; Axelsen, P. H.; Silman, I.; Sussman, J. L. *Science* **1994**, *263*, 1276–1278.
- [25] Wlodek, S. T.; Clark, T. W.; Scott, L. R.; McCammon, J. A. *J. Am. Chem. Soc.* **1997**, *119*, 9513–9522.
- [26] Zhou, H.-X.; Wlodek, S. T.; McCammon, J. A. *Proc. Natl. Acad. Sci. USA* **1998**, *95*, 9280–9283.
- [27] Tara, S.; Straatsma, T. P.; McCammon, J. A. *Biopolymers* **1999**, *50*, 35–43.
- [28] Bourne, Y.; Taylor, P.; Marchot, P. *Cell* **1995**, *83*, 503–512.
- [29] García, A. E. *Phys. Rev. Lett.* **1992**, *68*, 2696–2699.
- [30] Amadei, A.; Linssen, A. B. M.; Berendsen, H. J. C. *Proteins* **1993**, *17*, 412–425.
- [31] Balsera, M. A.; Wriggers, W.; Oono, Y.; Schulten, K. *J. Phys. Chem.* **1996**, *100*, 2567–2572.
- [32] Shen, T. Y.; Tai, K.; McCammon, J. A. *Phys. Rev. E* **2001**, *63*, 041902.
- [33] Karplus, M.; McCammon, J. A. *CRC Crit. Rev. Biochem.* **1981**, *9*, 293–349.

- [34] Ripoll, D. R.; Faerman, C. H.; Axelsen, P. H.; Silman, I.; Sussman, J. L. *Proc. Natl. Acad. Sci. USA* **1993**, *90*, 5128–5132.
- [35] Faerman, C.; Ripoll, D.; Bon, S.; Le Feuvre, Y.; Morel, N.; Massoulié, J.; Sussman, J. L.; Silman, I. *FEBS Letters* **1996**, *386*, 65–71.
- [36] Kronman, C.; Ordentlich, A.; Barak, D.; Velan, B.; Shafferman, A. *J. Biol. Chem.* **1994**, *269*, 27819–27822.
- [37] Bartolucci, C.; Perola, E.; Cellai, L.; Brufani, M.; Lamba, D. *Biochemistry* **1999**, *38*, 5714–5719.
- [38] Simon, S.; Le Goff, A.; Frobert, Y.; Grassi, J.; Massoulié, J. *J. Biol. Chem.* **1999**, *274*, 27740–27746.
- [39] Becker, O. M. *J. Mol. Struct. (Theochem)* **1997**, *398–399*, 507–516.
- [40] Becker, O. M. *Proteins* **1997**, *27*, 213–226.
- [41] Becker, O. M. *J. Comput. Chem.* **1998**, *19*, 1255–1267.
- [42] Rosenberry, T. L.; Rabl, C.-R.; Neumann, E. *Biochemistry* **1996**, *35*, 685–690.
- [43] Harel, M.; Kleywegt, G. J.; Ravelli, R. B. G.; Silman, I.; Sussman, J. L. *Structure* **1995**, *3*, 1355–1366.
- [44] Kryger, G.; Harel, M.; Giles, K.; Toker, L.; Velan, B.; Lazar, A.; Kronman, C.; Barak, D.; Ariel, N.; Shafferman, A.; Silman, I.; Sussman, J. L. *Acta Cryst.* **2000**, *D56*, 1385–1394.
- [45] Radić, Z.; Duran, R.; Vellom, D. C.; Li, Y.; Cerveñansky, C.; Taylor, P. *J. Biol. Chem.* **1994**, *269*, 11233–11239.
- [46] Marchot, P.; Prowse, C. N.; Kanter, J.; Camp, S.; Ackermann, E. J.; Radić, Z.; Bougis, P. E.; Taylor, P. *J. Biol. Chem.* **1997**, *272*, 3502–3510.
- [47] Marchot, P.; Bourne, Y.; Prowse, C. N.; Bougis, P. E.; Taylor, P. *Toxicon* **1998**, *36*, 1613–1622.
- [48] Marchot, P.; Khélif, A.; Ji, Y. H.; Mansuelle, P.; Bougis, P. E. *J. Biol. Chem.* **1993**, *268*, 12458–12467.
- [49] Eastman, J.; Wilson, E. J.; Cerveñansky, C.; Rosenberry, T. L. *J. Biol. Chem.* **1995**, *270*, 19694–19701.
- [50] Šentjurs, M.; Pečar, S.; Stojan, J.; Marchot, P.; Radić, Z.; Grubič, Z. *Biochim. Biophys. Acta* **1999**, *1430*, 349–358.
- [51] Radić, Z.; Taylor, P. *J. Biol. Chem.* **2001**, *276*, 4622–4633.

- [52] Radić, Z.; Quinn, D. M.; Vellom, D. C.; Camp, S.; Taylor, P. *J. Biol. Chem.* **1995**, 270, 20391–20399.
- [53] Szegletes, T.; Mallender, W. D.; Thomas, P. J.; Rosenberry, T. L. *Biochemistry* **1999**, 38, 122–133.
- [54] Mallender, W. D.; Szegletes, T.; Rosenberry, T. L. *Biochemistry* **2000**, 39, 7753–7763.
- [55] Shi, J.; Boyd, A. E.; Radić, Z.; Taylor, P. *J. Biol. Chem.* **2001**, 276, 42196–42204.
- [56] Kraulis, P. J. *J. Appl. Crystallogr.* **1991**, 24, 946–950.
- [57] Bourne, Y.; Taylor, P.; Bougis, P. E.; Marchot, P. *J. Biol. Chem.* **1999**, 274, 2963–2970.
- [58] le Du, M.-H.; Housset, D.; Marchot, P.; Bougis, P. E.; Navaza, J.; Fontecilla-Camps, J. C. *Acta Cryst.* **1996**, D52, 87–92.
- [59] Berendsen, H. J. C.; Postma, J. P. M.; van Gunsteren, W. F.; Di Nola, A.; Haak, J. R. *J. Chem. Phys.* **1984**, 81, 3684–3690.
- [60] Gillilan, R. E.; Wood, F. *Comput. Graph.* **1995**, 29, 55–58.
- [61] Baker, N. A.; Helms, V.; McCammon, J. A. *Proteins* **1999**, 36, 447–453.
- [62] Humphrey, W.; Dalke, A.; Schulten, K. *J. Mol. Graph.* **1996**, 14, 33–38.
- [63] Boyd, A. E.; Marnett, A. B.; Wong, L.; Taylor, P. *J. Biol. Chem.* **2000**, 275, 22401–22408.
- [64] Grochulski, P.; Li, Y.; Schrag, J. D.; Cygler, M. *Prot. Sci.* **1994**, 3, 82–91.
- [65] Baker, N.; Tai, K.; Henchman, R.; Sept, D.; Elcock, A.; Holst, M.; McCammon, J. A. Mathematics and Molecular Neurobiology. In *Advances in Computational Methods for Macromolecular Modeling: Theory and Application in Biomolecular Systems*; Schlick, T.; Gan, H. H., Eds.; Springer-Verlag: Berlin, 2002.
- [66] Tara, S.; Helms, V.; Straatsma, T. P.; McCammon, J. A. *Biopolymers* **1999**, 50, 347–359.
- [67] Millard, C. B.; Koellner, G.; Ordentlich, A.; Shafferman, A.; Silman, I.; Sussman, J. L. *J. Am. Chem. Soc.* **1999**, 121, 9883–9884.
- [68] Saxena, A.; Hur, R.; Doctor, B. P. *Biochemistry* **1998**, 37, 145–154.
- [69] Axelsen, P. H.; Harel, M.; Silman, I.; Sussman, J. L. *Prot. Sci.* **1994**, 3, 188–197.

- [70] Feynman, R. P. *No Ordinary Genius: the Illustrated Richard Feynman*; Norton: New York, 1994.
- [71] Smart, J. L.; McCammon, J. A. *Biophys. J.* **1998**, 75, 1679–1688.
- [72] Ghaffari-Farazi, T.; Liaw, J.-S.; Berger, T. W. *Neurocomputing* **1999**, 26–27, 17–27.
- [73] Stiles, J. R.; Bartol, T. M. Monte Carlo methods for simulating realistic synaptic microphysiology using MCell. In *Computational Neuroscience: Realistic Modeling for Experimentalists*; De Schutter, E., Ed.; CRC Press: New York, 2000.
- [74] Stiles, J. R.; Bartol, T. M.; Salpeter, M. M.; Salpeter, E. E.; Sejnowski, T. J. Synaptic variability: new insights from reconstructions and Monte Carlo simulations with MCell. In *Synapses*; Cowan, W. M.; Südhof, T. C.; Stevens, C. F., Eds.; Johns Hopkins University Press: Baltimore, 2001.
- [75] Holst, M. *Adv. Comput. Math.* **2001**, 15, 139–191.
- [76] Land, B. R.; Salpeter, E. E.; Salpeter, M. M. *Proc. Natl. Acad. Sci. USA* **1981**, 78, 7200–7204.
- [77] Land, B. R.; Harris, W. V.; Salpeter, E. E.; Salpeter, M. M. *Proc. Natl. Acad. Sci. USA* **1984**, 81, 1594–1598.
- [78] Kandel, E. R.; Siegelbaum, S. A. Directly gated transmission at the nerve-muscle synapse. In *Principles of Neural Science*; Kandel, E. R.; Schwartz, J. H.; Jessell, T. M., Eds.; Appleton and Lange: Norwalk, Connecticut, 1991.
- [79] Anglister, L.; Stiles, J. R.; Haesaert, B.; Eichler, J.; Salpeter, M. M. Acetylcholinesterase at neuromuscular junctions. In *Enzymes of the Cholinesterase Family*; Quinn, D. M.; Balasubramanian, A. S.; Doctor, B. P.; Taylor, P., Eds.; Plenum Press: New York, 1995.
- [80] Miyazawa, A.; Fujiyoshi, Y.; Stowell, M.; Unwin, N. *J. Mol. Biol.* **1999**, 288, 765–786.
- [81] Brejc, K.; van Dijk, W. J.; Klaassen, R. V.; Schuurmans, M.; van der Oost, J.; Smit, A. B.; Sixma, T. K. *Nature* **2001**, 411, 269–276.
- [82] Gisiger, V.; Stephens, H. *J. Physiol. Paris* **1982–1983**, 78, 720–728.
- [83] Florendo, J. A.; Reger, J. F.; Law, P. K. *Exp. Neurol.* **1983**, 82, 404–412.
- [84] Fahim, M. A.; Holley, J. A.; Robbins, N. *Neuroscience* **1984**, 13, 227–235.
- [85] Shalton, P. M.; Wareham, A. C. *Muscle Nerve* **1980**, 3, 120–127.

- [86] Tremblay, J. P.; Grégoire, L.; Sasseville, R.; Guay, G.; Belhumeur, C. *Synapse* **1988**, 2, 148–156.
- [87] Gisiger, V.; Stephens, H. R. *J. Neurosci. Res.* **1988**, 19, 62–78.
- [88] Schöberl, J. *Comput. Visual Sci.* **1997**, 1, 41–52.
- [89] Naka, T.; Sakamoto, N. *Math. Comput. Simul.* **2002**, 59, 87–94.
- [90] Schwartz, J. H. Synaptic vesicles. In *Principles of Neural Science*; Kandel, E. R.; Schwartz, J. H.; Jessell, T. M., Eds.; Appleton and Lange: Norwalk, Connecticut, 1991.
- [91] Südhof, T. C.; Scheller, R. H. Mechanism and regulation of neurotransmitter release. In *Synapses*; Cowan, W. M.; Südhof, T. C.; Stevens, C. F., Eds.; Johns Hopkins University Press: Baltimore, 2000.
- [92] Rotundo, R. L.; Rossi, S. G.; Anglistter, L. *J. Cell Biol.* **1997**, 136, 367–374.
- [93] Rice, S. A. *Diffusion-Limited Reactions*; Elsevier: Amsterdam, 1985.
- [94] Hosaka, Y.; Yokota, T.; Miyagoe-Suzuki, Y.; Yuasa, K.; Imamura, M.; Matsuda, R.; Ikemoto, T.; Kameya, S.; Takeda, S. *J. Cell Biol.* **2002**, 158, 1097–1107.
- [95] Baker, N. A.; Sept, D.; Joseph, S.; Holst, M. J.; McCammon, J. A. *Proc. Natl. Acad. Sci. USA* **2001**, 98, 10037–10041.
- [96] Harlow, M. L.; Ress, D.; Stoschek, A.; Marshall, R. M.; McMahan, U. J. *Nature* **2001**, 409, 479–484.
- [97] Gustafsson, J. S.; Birinyi, A.; Crum, J.; Ellisman, M.; Brodin, L.; Shupliakov, O. *J. Comp. Neurol.* **2002**, 450, 167–182.
- [98] MacKay, G. L. *From Far Formosa*; Oliphant Anderson and Ferrier: Edinburgh and London, 1896.

When a young man succeeds in passing the examinations for even the lowest degree, preparations on a most elaborate scale are made at his home for honoring him on his return. No one but an eye-witness can imagine the scene. A feast is prepared, theatrical performers are often engaged, a procession goes out to meet the graduate, who affects all the airs imaginable, and his conceit is swollen beyond endurance. His swagger is supercilious to the point of silliness. To recognize his old companions is a condescension for which they feel extremely grateful. The whole performance tends to make these graduates the most obnoxious of all the people one meets. [98]

Text face: Times, 12 points. Typeset using PDF \LaTeX by the author.

